8-2012

Study of Local Structure, Stress and Dynamics in Disordered Materials Using Ab-Initio and Molecular Dynamics Simulation

Madhusudan Ojha
mojha@utk.edu

To the Graduate Council:

I am submitting herewith a dissertation written by Madhusudan Ojha entitled "Study of Local Structure, Stress and Dynamics in Disordered Materials Using Ab-Initio and Molecular Dynamics Simulation." I have examined the final electronic copy of this dissertation for form and content and recommend that it be accepted in partial fulfillment of the requirements for the degree of Doctor of Philosophy, with a major in Physics.

Takeshi Egami, Major Professor

We have read this dissertation and recommend its acceptance:

Elbio Dagotto, David Keffer, Alexei P. Sokolov

Accepted for the Council:
Dixie L. Thompson

Vice Provost and Dean of the Graduate School

(Original signatures are on file with official student records.)

Study of Local Structure, Stress and Dynamics in Disordered Materials Using Ab-Initio and Molecular Dynamics Simulation

A Dissertation

Presented for the

Doctor of Philosophy

Degree

The University of Tennessee, Knoxville

Madhusudan Ojha

August 2012

This dissertation is dedicated to my parents for their love, endless support and encouragement.

Acknowledgements

First of all I would like to thank my dissertation advisor Professor Dr. Takeshi Egami for his kindness, patience, guidance, financial help in the form of graduate research assistantship and generosity and overall helping me to grow as a researcher. He was always available whenever I needed his guidance in spite of his very busy schedule. He always encouraged me to attend and participate in conferences, scientific talks, and summer schools. Event though I was working on theoretical calculation for my dissertation work, he always encouraged me to participate in neutron scattering and x-ray scattering experiments. I participated in a number of them. These opportunities helped me understand physics not only from the theoretical side but also from the experimental side.

I would also like to offer my sincere thanks to Dr. Don M. Nicholson, a senior research scientist at Oak Ridge National Laboratory (ORNL), for his tremendous help extended to me from the very beginning of my research work and in the whole dissertation writing process. He mentored me on a daily basis to help me to learn first principle calculations, including ab-initio molecular dynamics, to understand and interpret the results and to write the findings in the form of papers.

Also, I would like to thank Dr. David Keffer who is also one of my dissertation committee members for his guidance, which helped me to learn classical molecular dynamics simulations and to write analysis code.

Also, I thank my dissertation committee members Dr. Elbio Dagotto and Dr. Alexei P. Sokolov for their time and guidance.

I would like to thank my parents, both brothers and sister for their encouragement and support. Finally, I would like to extend my special thanks to my wife, Dr. Mamta Ojha, and my daughter, Manita Ojha, for their love, support and encouragement. Without their strong and unconditional support this work would not have been possible.

Abstract

Understanding the atomic structure and dynamics in structurally disordered systems has been a long-standing and most challenging problem in physics and material science. To begin with, it is difficult to describe disorder quantitatively and to differentiate the degree of disorder from one system to another. The majority of experimental and theoretical approaches to the study of disordered systems are either transferred directly from the study of crystals or address the problem in the macroscopic scale where the atomic origin of behavior is obscured. First principle atomic level stresses and dynamic pair distribution functions described in this dissertation represent attempts to overcome these limitations of current approaches. They relate system-specific atomic level properties to macroscopic properties such as viscosity and the glass transition temperature. The novel dynamic pair-density-function method effectively explores the dynamics in disordered systems as demonstrated by our discovery of super-localization in high-temperature liquid iron. The dynamic pair distribution function and local stresses are governed by the bonding within the cage of neighboring atoms; they reveal very localized dynamics. We have used atomic level stresses to characterize materials within the local approximation to density functional theory using the Locally Self-consistent Multiple Scattering method. The results of calculations on several crystals, liquids and glasses and radiation damaged bcc iron are presented. Atomic level stress calculations are also used to address the issue of metallic glass formability in the case of Au-Al system. We are advancing the field from qualitative results based

on models to system-specific, quantum-mechanics-based calculations of atomic level mechanisms.

Contents

List of Tables xii

List of Figures xiii

1 Introduction 1

2 Theoretical Background 10

2.1 Introduction 10

2.2 Structure Characterization 12

2.2.1 Pair-Density Function(PDF) 12

2.2.2 Static Structure Factor 14

2.3 Dynamics Characterization 15

2.3.1 General Dynamic Correlation Function 16

2.3.2 Intermediate Scattering Function 16

2.3.3 Mean Square Displacement (MSD) 19

2.3.4 The Van Hove Correlation Function 21

2.4 Features of the Glassy State 24

2.4.1 Fragility 25

2.4.2 The Kauzmann Paradox 27

2.4.3 Boson Peak 29

2.5 Radiation Damage 31

2.5.1 Primary Damage 31

2.5.2 Primary Damage Evolution 33

3 Methods **34**

3.1 Density Functional Theory 34

3.1.1 Kohn-Sham Theorems 35

3.1.2 Kohn-Sham Equation 37

3.1.3 Exchange-correlation Functional 38

3.2 Multiple Scattering Theory 40

3.2.1 Multiple-Scattering Theory Equations 40

3.2.2 Muffin-Tin and Atomic Sphere Approximation 44

3.3 The Locally Self-Consistent Multiple Scattering Theory(LSMS) Method 45

3.3.1 LSMS Algorithm 46

3.4 Dynamic Pair-Density Function 48

3.5 Theory of Atomic Level Stress 50

3.6 Molecular Dynamics Simulation 52

3.6.1 Background and History 52

3.6.2 Equations of Motion 53

3.6.3 Solution of Equation of Motion: Integration Algorithm 54

3.6.4 Periodic Boundary Condition 54

3.6.5 Temperature Control 55

3.7 MD Simulation of Displacement Cascade 56

3.8 First Principle Calculations of MD Simulated Data 57

4 Dynamic Pair-Density Function of Liquid Iron **58**

4.1 Introduction 58

4.2 Molecular Dynamics Simulation 59

4.3 Results 60

4.3.1 Pair-Density Function (PDF) 60

4.3.2 Static Structure Factor 61

4.3.3 Dynamic Pair-Density Function 63

4.4 Discussion 65

5 Crystalline and Amorphous Models of Highly Damaged Fe 66

5.1 Introduction 66

5.2 Computational Approach 67

5.3 Results and Discussion 69

5.4 Conclusion 75

6 First principle local stress 76

6.1 Introduction 76

6.2 Local Energy 78

6.3 Local Stress 82

6.4 Calculation Details 88

6.5 Results 94

6.6 Discussion and Conclusions 98

7 Glass Formability and Atomic level Stress in Al-Au system 99

7.1 Introduction 99

7.2 Au-Al System 102

7.2.1 Glass Formability 102

7.2.2 Au-Al Phase Diagram 103

7.3 Electronic States in Al-Au 105

7.3.1 First Principle Calculations 105

7.3.2 Electron Density, Fermi Level and Charge Transfer 108

7.3.3 Origin of the Deep Eutectic 110

7.3.4 Glass-Forming Ability 111

7.3.5 Conclusion 113

8 The Use of Atomic Level Stress to Characterize the Structure of Irradiated Iron 115

8.1 Introduction 115
8.2 Local Energy and Pressure 117
8.3 Procedure 119
8.4 Distribution of Volume and Pressure 120
8.5 Conclusion 125

9 Summary **126**

Bibliography **129**

Vita **140**

List of Tables

7.1 Deviation in local electron density (electron per atom) in Al_2Au, $AlAu_2$ and $AlAu_4$. 107

7.2 Deviation in local electron density (electron per atom) in Al_2Au, $AlAu_2$ and $AlAu_4$. 109

List of Figures

2.1 The radial distribution function: The radial distribution function $g(r)$ in liquid argon at relatively high temperature. The various peaks correspond to various shells around each particle (21). 13

2.2 The Static structure factor: The static structure factor $S(q)$ in a Lennard-Jones liquid at three different temperatures. The relaxation times increases by almost 4 orders of magnitude, and yet the structure factor shows no particular change (22; 23). 15

2.3 Left graph shows the exponential decay of the time correlation function $F(\vec{Q},t)$ as seen in normal liquids. The right figure shows the complex decay behavior shown by supercooled liquids viz., the early decay behavior I, the plateau II, the β -relaxation regimes IIa and IIb, and the α-relaxation regime III (25). 17

2.4 Two step relaxation in $F(\vec{Q},t)$ in a Lennard-Jones system (evaluated at the value of q where the static structure factor has the main peak). At high temperature the decay is exponential but as the temperature gets closer to the glass transition temperature, T_g, a plateau is formed and the relaxation shows two-step behavior (26). 18

2.5 The time dependence of the mean squared displacement for different temperatures: (a) The lennard Jones system, (b) Silica (27; 28). . . . 20

2.6 Self-part of Van Hove Correlation Function for a simple liquid (28). . 23

2.7 $G_d(r,t)/\rho$ for a simple liquid at different temperatures (28). 24

2.8 Angel plot of viscosity η for different glass-formers (29). 25
2.9 Kauzzmann Paradox. 28
2.10 Raman spectra of glassy $As_2S_3(1)$ and $SiO_3(2)$ normalized to boson peak intensity and energy, together with light-to-vibration coupling coefficients c(ω)(1' and 2') (43). 30
2.11 Heat Capacity Experiment on network and polymeric glass showing Boson peak (44). 31

3.1 Schematic of a parallel SCF algorithm. 47
3.2 Schematic picture showing PBC in 2D. 55

4.1 Modified Johnson's potential. 59
4.2 Pair density function of liquid and glassy phase iron. 61
4.3 Static Structure factor of liquid and glassy iron. 62
4.4 Dynamic pair-density function of liquid iron at 3000 K. 64

5.1 (a) The PDF shortly after cascade initiation (dashed) and at the peak of vacancy count (solid). (b) The PDF of super-cooled liquid Fe at several temperatures. 70
5.2 (a) The number of vacancies within spheres of various radii as a function of time. (b) The average temperature within spheres of various radii as a function of time. 71
5.3 (a) MSD over spheres of various radii over the cascade life as a function of time difference. (b) MSD of liquid Fe at various temperatures as a function of time difference. 73
5.4 (a) Distribution of atomic volumes within 1 nm radius shortly after cascade initiation. (b) Distribution of atomic volumes within 1 nm radius at peak of vacancy count. (c) Distribution of atomic volumes within 1 nm radius sphere of super-cooled liquid Fe at 1250K. 74

6.1 B2 structure; larger central(corner) atom represents Zr(Cu). 90

6.2 Atomic and total energy as a function of atomic volume for B2 CuZn. Curves are shifted to be zero at the equilibrium volume. 91
6.3 Atomic and average pressure as a function of atomic volume for B2 CuZn. The two dots indicate local pressure from virial expression at equilibrium volume. 92
6.4 Energy versus strain in the z direction (strain in x and y directions maintain volume). Curves are shifted to be zero at the equilibrium volume. 93
6.5 Stress versus strain in the z direction (strain in x and y directions maintain volume). 94
6.6 Average species pressure for CuZr in the B2, SQS, liquid and glass structures as a function of atomic volume. 95
6.7 Individual atomic pressures in CuZr liquid structure as a function of individual atomic volume. 96
6.8 The Cu-Cu and Zr-Zr pair distribution functions and their associated approximate potentials for liquid CuZr. The first and second neighbors distance are indicated by vertical dotted and solid lines respectively. . 97

7.1 Au-Si Phase Diagram (124). 100
7.2 Au-Al Phase Diagram (127). 101
7.3 XRD pattern of rapidly solidified $Au_{75}Al_{25}$ alloys (126). 102
7.4 Al_2Au crystal structure showing unit cell. 103
7.5 Al_2Au structure showing Au vacancies and (b) $AuAl_8$ cluster found in Al_2Au compound around Au. 104
7.6 (a) Unit cell of $AlAu_4$; (b) Unit cell of$AlAu_2$. 106
7.7 (a) Environment of Al in $AlAu_4$ (distorted icosahedra); (b) Environment of Au_1 in $AlAu_4$ (distorted icosahedra); (c) Environment of Au_2 in $AlAu_4$ (defective and distorted icosahedra). 111

7.8 (a) Local pentagonal atomic arrangement around Al in $AlAu_2$; (b) local heptagonal atomic arrangement around Au in $AlAu_2$. 112

8.1 The calculated (Modified Finnis and Sinclair (80) molecular dynamics (MD)) number of Frenkel pairs is shown as a function of time after cascade initiation for a series of PKA energies. 116

8.2 Deviation of VP-Volume from average (79.5 $a.u.$) 121

8.3 Deviation of local pressure from average value ($a.u.$). 121

8.4 Distribution of VP-Volumes as a function of local pressure. The straight-blue line indicates an upper or critical limit on volume as a function of pressure in the damaged-system. The curved-red line is the volume versus pressure curve for perfect crystal. 122

8.5 4 Distribution of local moments as a function of local pressure. The red line indicates the moment versus pressure curve for perfect crystalline alpha Fe. 124

8.6 Local moments as a function of VP-volume; red line is the moment per atom in perfect crystal. The data seems to show the Stoner criticality. 124

Chapter 1

Introduction

Disordered materials such as liquids and glasses are of scientific and technological importance as they play a crucial part in our daily life. For example, water covers two thirds of the surface of the earth and is the main component of our body. Likewise, the earth's core is a liquid at high temperature and pressure, although, some of the researchers think that the very central part of the core is crystalline (hexagonal Fe) (1)). Glasses are everywhere in our daily life ranging from windows of our houses and cars to the optical fiber for communications. Glass is used as a stable coating on medicines and also eaten as candy (although chocolates are crystalline). Modern functional materials are structurally complex and disordered. We often exploit their intrinsic disorder or extrinsically induced disorder to take advantage of their properties for scientific and technological purposes.

Material properties are closely related to their structure. Therefore the study of the relationship between atomic structure and material properties is fundamental in condensed matter physics as well as in material science. For example, graphite, diamond, carbon nanotubes and spherical fullerenes (bucky balls), all are made up of carbon atoms but their properties are quite different because they possess different atomic structures. It is the structure that is closely related to their practical function and hence the study of structure is important. In crystalline solids atomic correlations

extend to long range and to establish the relationship between the structure and property is relatively easy. For disordered materials as they lack long-range correlation understanding the structure-property relation is challenging.

The study of structure of disordered systems (2) such as liquids and glasses is an important and challenging problem. For example, they lack long-range periodicity found in crystalline substances and hence the traditional crystallographic tools for structural study cannot give complete information due to the absence of Bragg reflections. Furthermore, many theoretical and computational tools developed to study properties of crystalline substances cannot be applied to disordered system without making significant changes. Unlike gases liquids and glasses are condensed matter with strong short-range correlations in atomic positions, which change with temperature and time. Not only liquids and glasses but other materials of fundamental importance lack long-range periodicity; for example, amorphous semiconductors such as a-Si and a-Ge (3) amorphous bio-minerals (4) and, most soft matter, such as polymers, colloids and macromolecules including proteins, etc. Recently it is reported that amorphous silicon exhibits a glass transition and behaves like a glass (5). Furthermore, crystalline materials when exposed to radiation become amorphous and the study of radiation-damage in crystals and defects produced as a consequence is recently viewed as an important field of research.

Crystalline solids are characterized by long-range order that is described by repeating structural units. In crystalline solids, atoms vibrate around stable lattice positions. The lattice dynamics of crystalline solids can be well described in terms of phonons as elementary excitations and their thermal properties can be theoretically calculated by using phonons as a basis to evaluate the partition function. Today, with the advent of fast computers, we can calculate many properties of crystalline solids and molecules with amazing accuracy using first-principle calculations. Quantum mechanical calculations are helping us to design a whole new set of alloys, compounds and molecules. Whereas the science of crystalline solids is well advanced, our knowledge and understanding of science of disordered systems such as liquids and

glasses is still far behind those of crystalline materials. For instance when a liquid is cooled without crystallization its viscosity and relaxation time increase by 15 orders of magnitude over a relatively small (30 - 50%) range of temperature, and a liquid becomes a glass, behaving like a solid. But no satisfactory microscopic theory exits to describe this phenomenon, the glass transition. The nature of glass and glass transition is considered one of the most challenging theoretical problems in condensed matter physics (6; 7).

Metals and alloys, which generally exist as crystalline materials, can be converted to glass (metallic glass) by rapid cooling of their melt. Some of them do not even require rapid cooling, and thus can be made into a glass (bulk metallic glasses (BMG)) with regular cooling methods. These BMGs are technologically important due to their promising high compression strength, good corrosion resistance, and large elasticity compared to their crystalline counterparts (8). Due to their simpler atomic bonding (metallic bonding) compared to silica based glass they are a good candidate to study the general behavior of liquids and glasses.

The study of local structure in disordered systems is important and useful to understanding the underlying physics. However, as discussed above the lack of periodicity makes the study much more difficult than with crystalline materials. New methods should be proposed to deal with this difficult situation. Furthermore, in these disordered systems we still observe local chemical and topological order in the form of coordination number, nearest neighbor distances, nearest neighbor bond lengths and bond angles etc. But, these types of order are local and disappear or decay rapidly with distance from an atom.

It is a common practice to describe the structure of liquids, glasses and other disordered materials in terms of atomic pair-density function (PDF), which measures the probability of finding a particle (labeled j) from other particle (labeled i) of the system at a certain distance$r$ apart. Experimentally, the PDF is obtained by Fourier transforming the static structure factor, $S(Q)$, obtained from X-ray or neutron diffraction experiment (9). The PDFs of disordered (or amorphous) materials give

information about the short-to-medium range order by showing peaks at small value of distances (r). The PDF does not provide a complete picture of the structure of a material because it is a spherically averaged one-dimensional quantity. But, it gives structural information about the material in the form of the peak positions, peak widths, and relative intensities of the peaks etc. In the disordered systems the first peak of the PDF gives information about the nearest neighbor distance and thus shows some short-range order and the peaks beyond first peak giving the short-to-medium range order. As the peaks in PDFs in disordered material die off after a few peaks, no long-range order can be seen in PDF as expected. But, PDF cannot completely describe the structure present in liquids and glasses as it takes into account the two body correlations only, whereas local structure and properties may be dependent on many-body correlations.

It is a common practice in experimental studies using neutrons and X-rays to describe collective excitations (dynamics) by assuming that the sample under study is crystalline and it possesses translational symmetry. Therefore, conventionally liquid dynamics is also measured by neutron scattering experiments using the dynamic structure factor, $S(Q, \omega)$ which provides information about the inter-particle correlation in reciprocal space and its time evolution. But, many materials studied today are not perfectly crystalline and collective dynamics in such materials are damped (or scattered) and the dynamic structure factor, $S(Q, \omega)$, may not capture the dispersion correctly. If we take the Fourier transform of $S(Q, \omega)$ we can get a dynamic quantity $\rho(r, \omega)$ called the dynamic pair-density function (DPDF) which gives the density of pairs of atoms separated by distance r and vibrating at an angular frequency of ω (9; 10). The power of this method is that it provides information about local dynamics in strongly disordered systems (such as liquids and glasses) in real space. The DPDF can also be determined by MD simulations and the results obtained can be compared to the results of neutron scattering experiments (11). This method is useful when the excitations are localized in space and hence powerful to study local dynamics rather than collective dynamics (11; 9).

In order to describe the atomic environment reasonably, the concept of atomic-level stress, which results from the incompatibility between a given atom and its surroundings, was introduced by Egami et al. (12). Atomic level stress is defined as the first order local response in energy to homogeneous (affine) strain (13). In a perfect crystal at absolute zero with one atom per unit cell, at equilibrium, we will not observe any atomic-level stress. But, even in perfect crystals atomic-level stresses appear due to the lattice vibrations and lattice defects and also from any deviation from the equilibrium. The theory of atomic level stress assumes that in the case of liquids, disordered solids and glasses, the atoms are not ideally packed as in the case of closed packed structures. Because of this situation in liquids, disordered solids and glasses, the atomic environment of each atom is different from other atoms around it and each atom is under different amounts of stress. Hence, the theory of atomic level stress finds its usefulness in the study of these systems. The atomic level stress is very sensitive to atomic environment (the chemical nature of atoms, nature of the cage or bonding, size of atoms, effective inter-atomic potentials etc.) around it, and hence related to the local structures of the system. Thus, atomic level stresses can be used to describe the local structures in liquids and glasses and the local structures can be related to their properties (13).

Computational physics is now an established mainstream field of research. Recent advances in computers and the computational techniques have greatly improved the power of theoretical tools such as molecular dynamics (MD) simulations and the first-principle calculations based on the Density functional theory (DFT) (14; 15). These days MD simulations with million atoms and DFT calculations with thousands of atoms are routinely performed. This advancement has provided a powerful computational platform to understand the dynamics in liquids and glasses. Therefore, the results obtained from MD simulations and DFT calculations can be used to develop physically intuitive analytical theories that will be able to provide a more complete picture of complex dynamics associated with liquids and other disordered materials.

Quantum mechanical calculation of macroscopic stress exploits the Hellmann-Feynman theorem (16). Errors in approximating the change in the electron density under deformation do not affect the stresses, which are first derivatives with respect to deformation while errors in the electron density only contribute to changes in the total energy at the second order. While the total energy is stationary with respect to the electron density any decomposition of the energy into components results in each component having a non zero variation such that the average variation vanishes. In particular changes in atomic charge under deformation result in non-vanishing contributions to the component stress. Here, we are proposing a method where the total energy is expressed as a sum of the local atomic level energies, $E = \sum_i E_i$. The atomic level stresses are obtained by the local response to affine deformations of the atomic positions. The non-affine behavior of the electron density contributes to the local stress and is particularly large when there is large electron transfer. The non-affine behavior of the electron density is made particularly clear by consideration of the density of the 1s core levels which are largely unaffected by deformation. The locally Self-consistent Multiple Scattering theory (LSMS) method (17; 18; 19) is used to evaluate the local energies within the local density approximation to DFT .The LSMS method is an order-N approach to the calculation of the electronic structure of large systems in the local density approximation (LDA). It is based on the observation that a good approximation to the electron density and the density of states (DOS) on a particular atom within a large system, and hence the total energy of that system, can be calculated by considering only the electronic multiple scattering processes in a finite spatial region. This finite spatial region is called local interaction zone (LIZ) centered at that atom. In all calculations the local Kohn-Sham potential is treated in the Atomic Sphere Approximation (19).

Radiation damage occurs when radiation from nuclear reactors such as high energy neutrons pass through reactor materials and collide with atoms of these materials transferring part of their original energy to these atoms. When a crystalline sample is subjected to radiation its structure does not remain perfectly crystalline afterwards.

Radiation damage can change the structure of crystalline solids in irreversible ways making them disordered. Radiation damage often brings significant changes in the physical properties of irradiated materials. The microscopic processes that bring about these changes are not fully understood, thereby limiting our ability to predict the consequences of irradiation. Therefore, the study of radiation damage in solids is very important for nuclear technology to understand the service-life of any material to be used in nuclear reactors. Therefore, to study radiation damaged sample of bulk crystalline materials new approaches should be used.

In this dissertation, Chapter two presents some of the relevant and important theoretical background of liquid and glass structure and dynamics, and a brief introduction about the radiation damage in matter.

Chapter three of the dissertation discusses the basics of the Density Functional Theory (DFT) methods. This chapter also discusses the Locally Self Consistent Multiple Scattering (LSMS) method, the theory of atomic level stress and the dynamic pair-density function used in this dissertation.

The dynamic pair-density function of liquid iron at high temperature is calculated using MD simulation to understand the local dynamics in a high temperature liquid. The results are given in Chapter four.

The structure of irradiated material near a primary knock on atom shortly after the impact is largely unknown. MD simulations with classical force fields provide the foundation for our current understanding of the resulting cascade. Atomic level structural characterization is often done in terms of the defects within the context of a perfect bulk, however, the choice of the best representation is complicated because the density of the defects is high, the material is inhomogeneous and it is not in equilibrium. Here we explore the adaptation of tools typically employed to characterize homogeneous equilibrium liquids to the highly defected region of the cascade. A structure corresponding to a radiation-damaged sample of bcc iron immediately after the impact was analyzed using the pair-density function (PDF)

and the dynamics was studied using mean square displacement (MSD). The results are discussed in Chapter five.

To understand the atomic level stresses in liquids and glasses it is equally important to understand the value and nature of atomic level stress in their crystalline solid phases for comparison and for interpretation of the results. Therefore, we have calculated atomic level stresses in some simple crystalline intermetallic compounds as well as liquids and glasses so that the knowledge acquired from this can be utilized to understand liquid and glass phases. It is generally believed that in crystalline solids stress is absent, but our first principle calculation shows that this is not the case. In Chapter six the atomic level stresses in intermetallic B2 structures are calculated using first principle method and compared to liquids and glasses.

Glass formability is a fundamental question in the field of bulk metallic glass (BMG). Compared to glasses made from silicates the formation of metallic glass is difficult because metals tend to crystallize easily upon cooling. Because of this reason the first sample of metallic glass ($Au_{75}Si_{25}$) about approximately 10 micrometer in thickness was obtained when cooling the melt at a rate of $10^5 - 10^6$ K/s (20). These days metallic glass are formed with much smaller cooling rates but one needs to select constituent elements and the composition very carefully to avoid crystallization, and it's a matter of art rather than science to get a good glass former. The gold-aluminum system exhibits various features (negative heat of mixing, deep eutectic etc.), which suggest a possibility of glass formability, but it does not form a glass. Atomic level stresses are calculated using first principles for three different phases of Al-Au system (Al_2Au, $AlAu_2$ and $AlAu_4$) to understand the complex dynamics present in this system and details are presented in Chapter seven.

Even though the MD simulations with classical force fields provide the foundation for understanding of cascades found in radiation damaged samples, with the improvements of computational power, modern density functional calculations can now treat large numbers of atoms to realistically represent irradiated samples. They can provide additional details of the magnetic and electronic nature of irradiated

samples. The atomic level stresses for an instantaneous configuration following the formation of a low energy cascade in bcc iron were calculated from the first principles. Here, for the first time atomic level stress is used as a characterization tool to study a radiation damaged sample. The results are presented in Chapter eight.

Finally, Chapter nine gives the summary and future direction

Chapter 2

Theoretical Background

2.1 Introduction

Liquids and glasses are two prominent examples of structurally disordered systems that are challenging and interesting to study. If a liquid is cooled it becomes a crystal through a first order phase transition, but the first order transition involves an interface, and thus its kinetics depends on composition. In some cases crystallization is slow enough that a liquid can be cooled below the melting temperature (supercooling) without crystallization and a glass can be obtained. Glass behaves as a mechanically stable off-equilibrium system. In other words, glasses show some properties of crystalline state viz. mechanical rigidity but they have disordered structures at the molecular level like liquids. In a glassy phase the system remains trapped in one part of the phase space. This condition is called non-ergodicity. A supercooled liquid becomes a glass at the glass transition temperature, T_g, when the viscosity, η, becomes equal to 10^{13} poise. In the glassy state the liquid is essentially frozen in the laboratory time scale. In general the time scale of liquid dynamic is expressed by the Maxwell relaxation time, $\tau_M = \eta/G_\infty$, where G_∞ is the instantaneous shear modulus. For higher temperature liquids the relaxation time is much smaller than the experimental time scale and in supercooled liquids the

relaxation time is of the order of observation time but when the system enters the glassy phase the relaxation time becomes much longer than the observation time. At the glass transition temperature the Maxwell relaxation time is of the order of 100 to 1000 sec. Thus, while going from liquid to glass the viscosity and relaxation time change by a huge 15 orders of magnitude.

The glassy state is found for all classes of materials viz. oxide (e. g. SiO_2), ionic (e. g. ZnF_2), polymeric, metallic, carbohydrates etc. Also crystalline materials when irradiated with ionizing particles such as neutrons can become amorphous. Recently radiation damage in structural materials such as iron has received much attention, as indicated by the recent establishment of one of the Energy Frontier Research Centers, Center for Defect Physics (CDP) at Oak Ridge National Laboratory (ORNL) which focuses on studying Radiation damage in materials using theory, modeling and experiment.

Remarkable progresses have been made in the field of glass physics in the last few decades but our understanding of physics of the glass is not yet complete. No single microscopic theory is present that can describe glass dynamics.

Generally, metals and alloys are crystalline in nature. Pure metals cannot form glass because their structures prefer crystalline phases compared to glassy phases on cooling the liquid phase. But metallic alloys can stabilize the liquid and help glass formation according to the confusion principle. For example, the binary alloy $Fe_{80}Be_{20}$ can be made glass with a critical cooling rate of 10^5 to 10^6 K/s. It is observed that multicomponent composition favors glass formability; glass formation can be achieved with much lower cooling rates as low as 1 K/s and glasses can be made in bulk (dimensions more than 1 cm). Metallic glasses, newcomers in the field of glass physics, are simpler in structure and they offer a new opportunity of studying basic fundamental processes in the liquid and glass.

Characterizing the structure of liquids and glasses has been a difficult subject. Also, understanding the dynamics in the liquids and glasses is a challenging field. This chapter describes some of the tools used to characterize the structure and dynamics

of liquids and glasses and some of the salient features of glassy and supercooled liquids. Furthermore, a discussion of radiation damage in crystalline material will be presented.

2.2 Structure Characterization

Generally the pair-density function and the static structure factor are used to characterize the structures of liquids and glasses.

2.2.1 Pair-Density Function(PDF)

In ordinary sense as we are introduced in introductory physics class that there are three states of matter viz. solids, liquids and gases and first major difference among them are the manner in which they occupy space. There are clear structural differences among gas, liquid and solid (crystal) which is apparent in the pair-density function , which is defined as (9)

$$g(\vec{r}) = \frac{1}{N\rho} \left\langle \sum_{i=1}^{N} \sum_{j \neq i}^{N} \delta(\vec{r} + \vec{r}_j - \vec{r}_i) \right\rangle \tag{2.1}$$

Here, ρ is the number density. For isotropic systems such as liquids the angular dependence can be integrated over to define the radial distribution function $g(r)$. The radial distribution function (RDF) or pair-density function (PDF) measures the probability of finding particles (labeled j) at a distance r from a tagged particle (labeled i). It can be expressed as:

$$g(r) = \frac{1}{4\pi r^2} \frac{1}{N\rho} \left\langle \sum_{i=1}^{N} \sum_{j \neq i}^{N} \delta(r - |\vec{r}_j - \vec{r}_i|) \right\rangle = \frac{1}{4\pi r^2} \frac{1}{N\rho} \left\langle \sum_{i=1}^{N} \sum_{j \neq i}^{N} \delta(r - r_{ij}) \right\rangle \tag{2.2}$$

Here, N is the total number of particles and ρ is the density and,

$$r_{ij} = |\vec{r}_j - \vec{r}_i| \tag{2.3}$$

It is straightforward to show that $g(r)$ satisfies the integral rule:

$$\int_0^\infty 4\pi r^2 \rho g(r) dr = N - 1 \sim N \tag{2.4}$$

It is clearly seen that $g(r)$ must go to unity for large values of r. Furthermore; the product $\rho\, g(r)$ gives the mean local density at distance r from a central particle. The different phases of particle systems are clearly distinguishable in their radial distribution functions. In liquid, the typical shape of the function is as shown in Figure 2.1

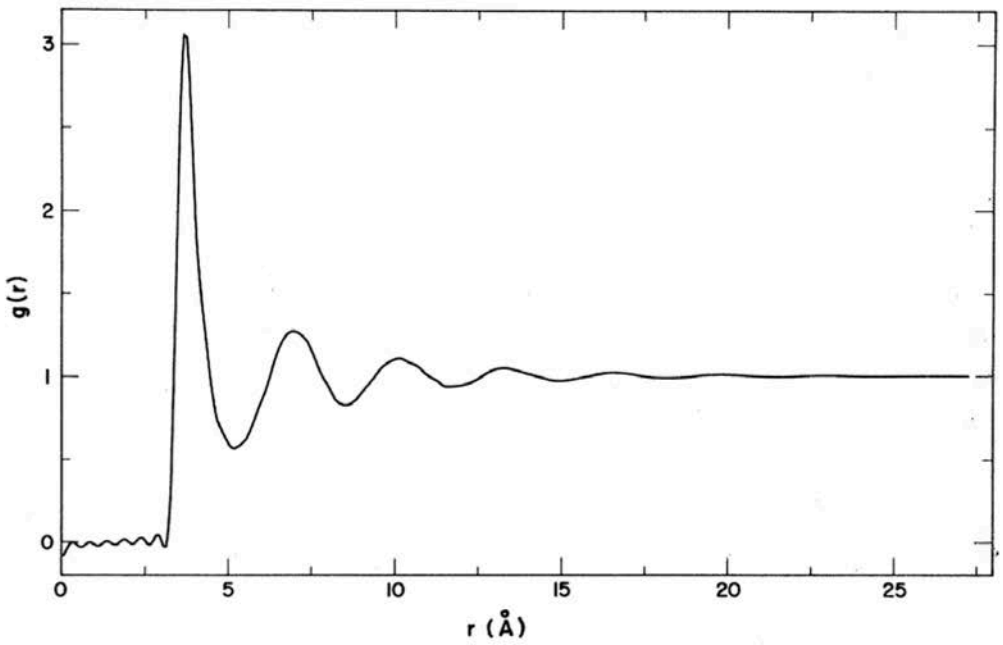

Figure 2.1: The radial distribution function: The radial distribution function $g(r)$ in liquid argon at relatively high temperature. The various peaks correspond to various shells around each particle (21).

At smaller values of r, $g(r)$ is zero because short-range repulsion prevents atoms from getting too close to each other; at larger r, $g(r)$ rises steeply corresponding to the first shell of particles around the focal one; at even larger r it shows weaker but well defined peaks corresponding to the various shells around the focal one. The peaks become weaker as r increases indicating the absence of long-range order in liquids.

A crystal is dense and ordered. Therefore, in crystals at low temperature, $g(r)$ shows sharp peaks, which do not decay to zero because of the existence of long-range order. The peaks would be delta- functions except they become Gaussian due to thermal or quantum mechanical vibrational motion. Spatial correlation extends throughout the entire crystal. On the other hand, in a gas we only see the drop of probability at very low r due to the hard core of the particles, and peaks are usually limited to the first nearest neighbors.

The radial distribution function for the glass is similar to that of liquid. So glass is similar to liquid as far as structure is concerned. They also belong to the same thermodynamic phase.

2.2.2 Static Structure Factor

Inelastic neutron scattering allows us to measure experimentally the static structure factor $S(q)$. It is related to the radial distribution function $g(r)$ by a simple Fourier integral.

$$S(q) = 1 + 4\pi\rho \int_0^\infty r^2 \frac{\sin qr}{qr}(g(r) - 1)dr \tag{2.5}$$

The static structure factor gives the same kind of information in momentum space as is given by the pair-density function in real space. It is seen that the static structure factor of a deeply supercooled liquid, of an off-equilibrium glass, and of high temperature liquids are almost indistinguishable as shown in Figure 2.2. This shows that the average structure of glass-formers changes only slightly upon supercooling.

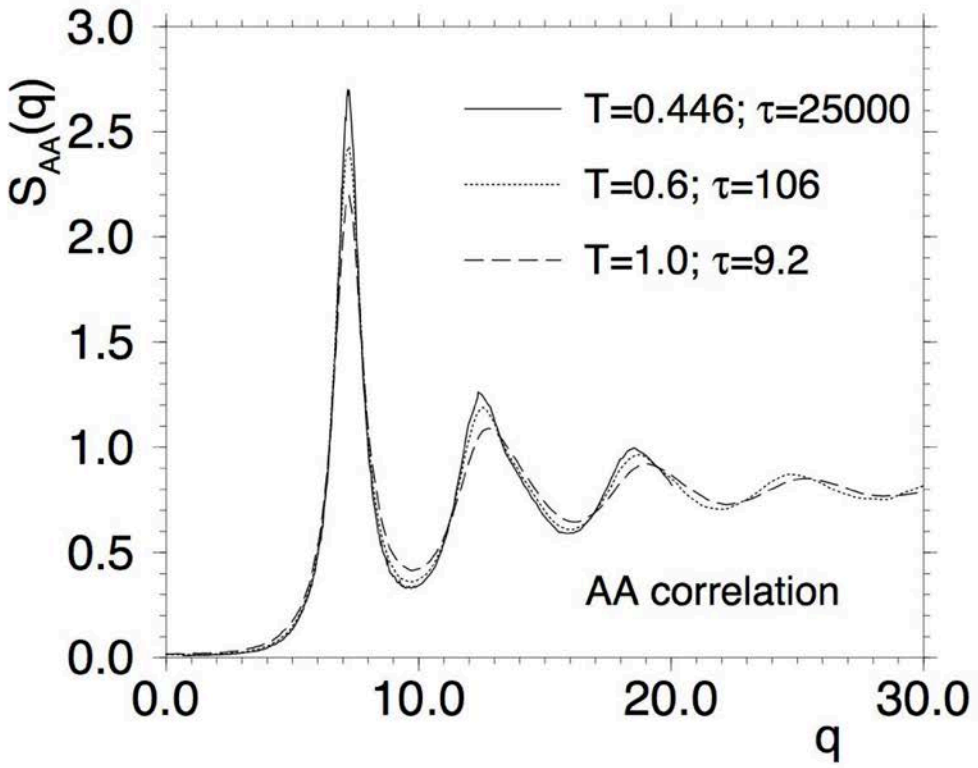

Figure 2.2: The Static structure factor: The static structure factor $S(q)$ in a Lennard-Jones liquid at three different temperatures. The relaxation times increases by almost 4 orders of magnitude, and yet the structure factor shows no particular change (22; 23).

Even though at present it appears that it is difficult to find the relation between the nature of atomic arrangements and the spectacular variation of dynamic quantities, in supercooled liquids, structure remains a natural key concept for understanding dynamics.

2.3 Dynamics Characterization

Below are listed some of the functions that are used to characterize the dynamics of liquids and glasses.

2.3.1 General Dynamic Correlation Function

A general dynamic correlation function can be expressed as (24):

$$C(t_1, t_2) = \frac{1}{N} \sum_{i=1}^{N} \langle \phi_i(t_1) \phi_i(t_2) \rangle \tag{2.6}$$

where $\phi_i(t)$ is a general quantity related to particle i of the system at time t. For a system in equilibrium, the above equation reduces to:

$$C(t) = \frac{1}{N} \sum_{i=1}^{N} \langle \phi_i(t) \phi_i(0) \rangle \tag{2.7}$$

The density of particles in a liquid can be expressed as:

$$\rho(\vec{r}, t) = \sum_i \delta(\vec{r} - \vec{r}_i) \tag{2.8}$$

In liquids, the typical choices of $\phi_i(t)$ is the Fourier transformed density, $\rho_{\vec{Q}}(t)$, which is given by,

$$\rho_{\vec{Q}}(t) = \int e^{i\vec{Q}.\vec{r}} \left(\sum_i \delta(\vec{r} - \vec{r}_i(t)) \right) d\vec{r} = \sum_i e^{i\vec{Q}.\vec{r}(t)} \tag{2.9}$$

2.3.2 Intermediate Scattering Function

The intermediate scattering function is given by

$$F(\vec{Q}, t) = \frac{1}{N} \left\langle \rho_{-\vec{Q}}(0) \rho_{\vec{Q}}(t) \right\rangle = \frac{1}{N} \sum_{ij} e^{i\vec{Q}.(\vec{r}_j(t) - \vec{r}_i(0))} \tag{2.10}$$

Here, N denotes the number of particles in the liquid system, $\vec{r}_i(t)$ denotes the vector coordinates of the particle i at time t and $\langle .. \rangle$ indicates an average over time origins. This time correlation function describes the time decay of density fluctuations in a system and therefore is of particular interest in the case of supercooled liquids. Perturbation in the liquid system is reflected in the change in $F(\vec{Q}, t)$.

The intermediate scattering function, $F(\vec{Q},t)$, may be separated into two parts, the self part (s) and the distinct part (d) as given below

$$F(\vec{Q},t) = F_s(\vec{Q},t) + F_d(\vec{Q},t) \tag{2.11}$$

Here,

$$F_s(\vec{Q},t) = \frac{1}{N}\left\langle \sum_{i=1}^{N} \mathrm{e}^{-i\vec{Q}.[\vec{r}_i(t)-\vec{r}_i(0)]} \right\rangle \tag{2.12}$$

$$F_d(\vec{Q},t) = \frac{1}{N}\left\langle \sum_{j=1}^{N}\sum_{k\neq j}^{N} \mathrm{e}^{-i\vec{Q}.[\vec{r}_j(t)-\vec{r}_k(0)]} \right\rangle \tag{2.13}$$

In normal liquids, $F(\vec{Q},t)$ decays exponentially with relaxation time as shown schematically in the left graph of Figure 2.3. Supercooled liquids show a different behavior. As shown on the right side of Figure 2.3, the short-time behavior is stepped shaped and the correlation function reaches a plateau at intermediate times (β-relaxation) and the long-time behavior in region III and beyond is called α-relaxation regime.

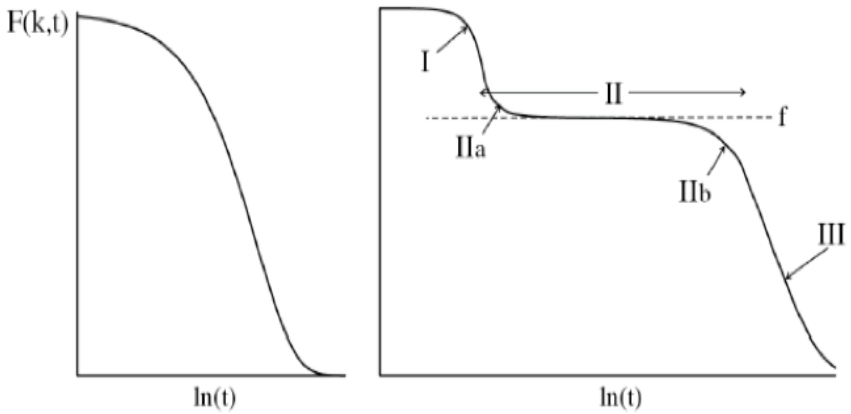

Figure 2.3: Left graph shows the exponential decay of the time correlation function $F(\vec{Q},t)$ as seen in normal liquids. The right figure shows the complex decay behavior shown by supercooled liquids viz., the early decay behavior I, the plateau II, the β -relaxation regimes IIa and IIb, and the α-relaxation regime III (25).

The Stretched exponential law generally fits this behavior:

$$F(\vec{Q},t) \sim e^{-(t/\tau)^{\beta}} \tag{2.14}$$

Here, τ is called relaxation time and gives information about the time scale of the decay. In general, τ and β both depend on the temperature and on the wave number of the perturbation being examined as shown in Figure 2.4. It is argued that the β-relaxation regime is governed by the so-called cage-effect; i. e., the rattling of the particles within a cage formed by nearest neighbors.

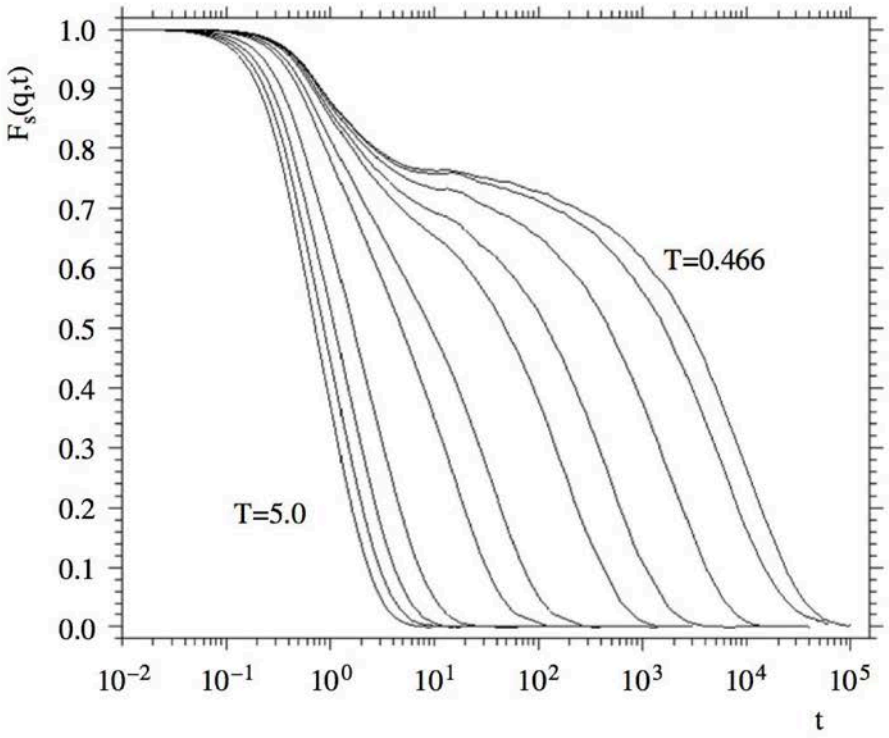

Figure 2.4: Two step relaxation in $F(\vec{Q},t)$ in a Lennard-Jones system (evaluated at the value of q where the static structure factor has the main peak). At high temperature the decay is exponential but as the temperature gets closer to the glass transition temperature, T_g, a plateau is formed and the relaxation shows two-step behavior (26).

The α-relaxation corresponds to the structural relaxation and is argued to involve a coordinated and cooperative motion of particles leading to the breaking of the cage. In conclusion we can say that $F(\vec{Q},t)$ characterizes the collective dynamics of the liquid. Furthermore, the self-part of the intermediate scattering function can be measured by neutron spin echo experiment. The spectrum of the intermediate scattering function is called the dynamic structure factor, $S(\vec{Q},\omega)$; it can be measured by inelastic neutron scattering.

$$S(\vec{Q},\omega) = \int_{-\infty}^{\infty} F(\vec{Q},t)e^{-i\omega t}dt \tag{2.15}$$

2.3.3 Mean Square Displacement (MSD)

The mean square displacement is one of the simplest quantities that can be easily measured in molecular dynamics simulation and at the same time is very useful physical quantity giving information about the dynamics of liquids and supercooled liquids. The mean squared displacement (MSD) of a tagged particle α, $\langle {r^2}_\alpha(t)\rangle$,is defined as:

$$\left\langle r_\alpha^2(t)\right\rangle = \frac{1}{N_\alpha}\sum_{i=1}^{N_\alpha}\left\langle |\vec{r}_i^{\alpha}(t) - \vec{r}_i^{\alpha}(0)|^2\right\rangle \tag{2.16}$$

Here, $\langle..\rangle$ denotes the time average. Figure 2.5 shows the time dependence of MSD for different temperatures (27; 28). It is clear from the Figure 2.5 that, at short times MSD shows a quadratic dependence on time, $\langle r_\alpha^2(t)\rangle \propto t^2$ because for short times the particles will move ballistically, i. e. $\vec{r}_i^{\alpha} \approx \vec{r}_i^{\alpha}(0) + \dot{\vec{r}}_i^{\alpha}t$ and thus giving t^2 time dependence to MSD. For longer times particle motion becomes diffusive and hence MSD shows linear time dependence. Furthermore, at high temperatures both short and very long times have power law behavior; at low temperatures there is a plateau at intermediate times, which is not present at high temperature.

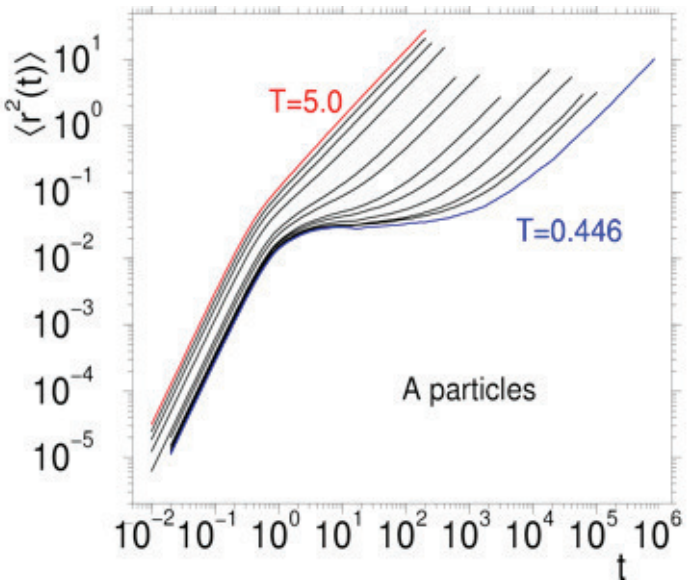

(a) The lennard Jones system

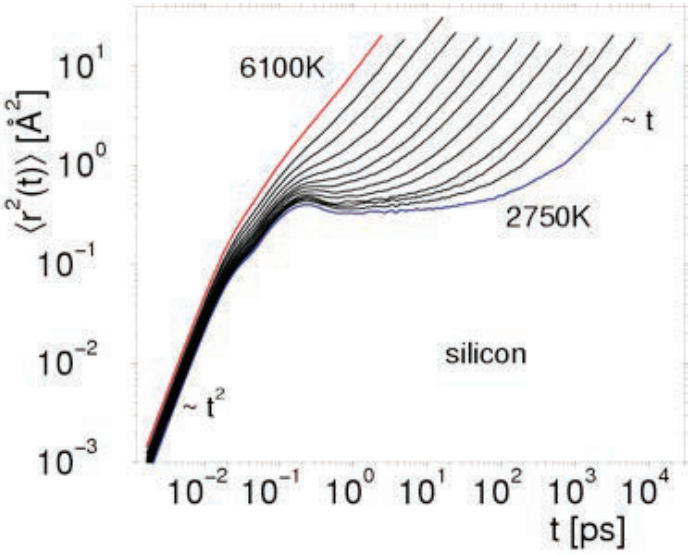

(b) Silica

Figure 2.5: The time dependence of the mean squared displacement for different temperatures: (a) The lennard Jones system, (b) Silica (27; 28).

This is called cage effect i.e., the tagged particle is confined in a cage formed by its neighbors and the particle takes long time to come out of this cage. The cage effect is enhanced as the temperature is lowered.

One can easily calculate the self-diffusion constant $D(T)$ from MSD using the Einstein relation:

$$D = \lim_{t\to\infty} \frac{\langle r_\alpha^2(t)\rangle}{6t} \tag{2.17}$$

2.3.4 The Van Hove Correlation Function

A density-density time correlation function or van Hove correlation function $G(\vec{r},t)$ is defined as (24):

$$\begin{aligned} G(\vec{r},t) &= \tfrac{1}{\rho}\left\langle \rho(\vec{r},t)\rho(0,0)\right\rangle \\ &= \tfrac{1}{N}\left\langle \sum_i \sum_j \delta[\vec{r} - (\vec{r}_j(t) - \vec{r}_i(0))] \right\rangle \end{aligned} \tag{2.18}$$

Here the angular brackets represent the usual time average over a system at equilibrium and δ is the Dirac delta symbol. The space-time correlation function $G(\vec{r},t)$ is proportional to the probability that an atom is at position $\vec{r}$ at time t given that an atom was at the origin $\vec{r}=0$ at initial time $t=0$. The space-time correlation function $G(\vec{r},t)$ can be separated into two parts:

$$G(\vec{r},t) = G_s(\vec{r},t) + G_d(\vec{r},t) \tag{2.19}$$

Here $G_s(\vec{r},t)$ and $G_d(\vec{r},t)$ are respectively called the self-part and distinct-part of $G(\vec{r},t)$ and can be expressed as:

$$G(\vec{r},t) = G_s(\vec{r},t) + G_d(\vec{r},t) \tag{2.20}$$

$$G_s(\vec{r},t) = \frac{1}{N}\left\langle \sum_i \delta[\vec{r} - |\vec{r}_i(t) - \vec{r}_i(0)|] \right\rangle \tag{2.21}$$

$$G_d(\vec{r},t) = \frac{1}{N}\left\langle \sum_i \sum_{j\neq i} \delta[\vec{r} - |\vec{r}_j(t) - \vec{r}_i(0)|] \right\rangle \tag{2.22}$$

For homogeneous uniform substance $G_s(\vec{r},t)$and $G_d(\vec{r},t)$ depend only on scalar distance and hence equations 2.21 and 2.22 reduce to (24):

$$G_s(r,t) = \frac{1}{N}\left\langle \sum_i \delta[r - |\vec{r}_i(t) - \vec{r}_i(0)|] \right\rangle \xrightarrow{t,\, r\to\infty} \frac{1}{(4\pi Dt)^{3/2}} \exp(r^2/4Dt) \tag{2.23}$$

$$G_d(r,t) = \frac{1}{N}\left\langle \sum_i \sum_{j\neq i} \delta[r - |\vec{r}_j(t) - \vec{r}_i(0)|] \right\rangle \xrightarrow{t,\, r\to\infty} \rho \tag{2.24}$$

Furthermore, $G_s(r,0) = \delta$ and $G_d(r,0) = \rho g(r)$. Figure 2.6 shows $4r^2 G_s(r,t)$ for simple (Lennard- Jones) liquid (28) at three different temperatures.

It is clear from the figure that at high temperatures, the self part of van Hove correlation function decays in a regular manner and there is a slight change in decay pattern for intermediate temperatures where we can see a weak tendency of clustering but this effect is much more enhanced at the lowest temperatures. This clustering suggests dramatic slowing down of the particle motion as the temperature goes down and this is called cage effect. Experimentally we cannot measure $G_s(r,t)$ but using neutrons spin echo measurements it is possible to measure its space Fourier transform, the incoherent intermediate scattering function $F_s(Q,t)$. Thus it is very interesting and informative to calculate these quantities using computer simulations.

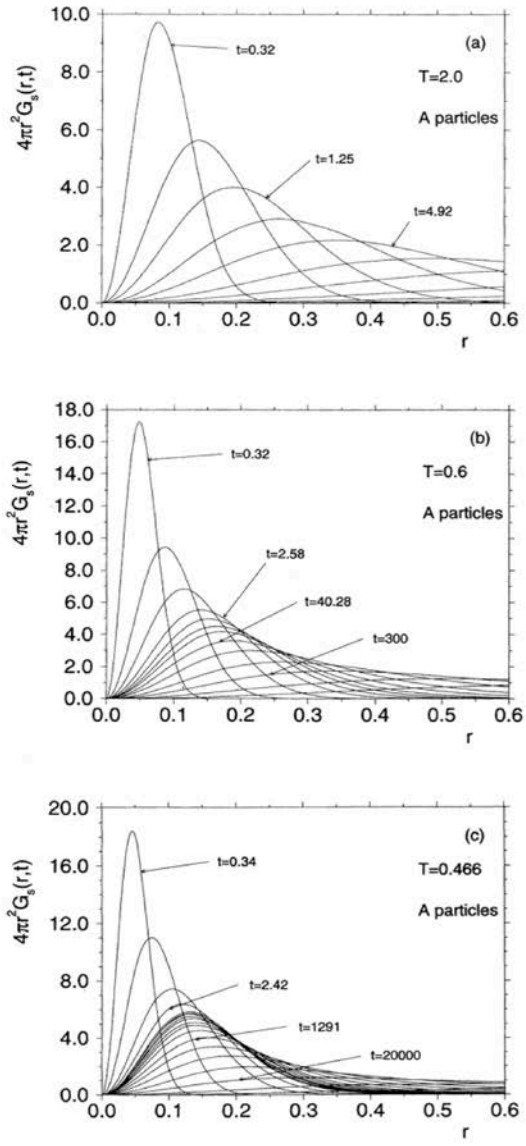

Figure 2.6: Self-part of Van Hove Correlation Function for a simple liquid (28).

Figure 2.7 shows the dependence of $G_d(r,t)/\rho$ on temperature for a simple liquid. We can see here that for high temperatures $G_d(r,t)/\rho$ decays without displaying any particular feature. This happy situation changes when the temperature is lowered and we observe at intermediate times the correlation function start to cluster and this effect get enhanced as the temperature is lowered further. This feature at low temperature can be related to the β-relaxation.

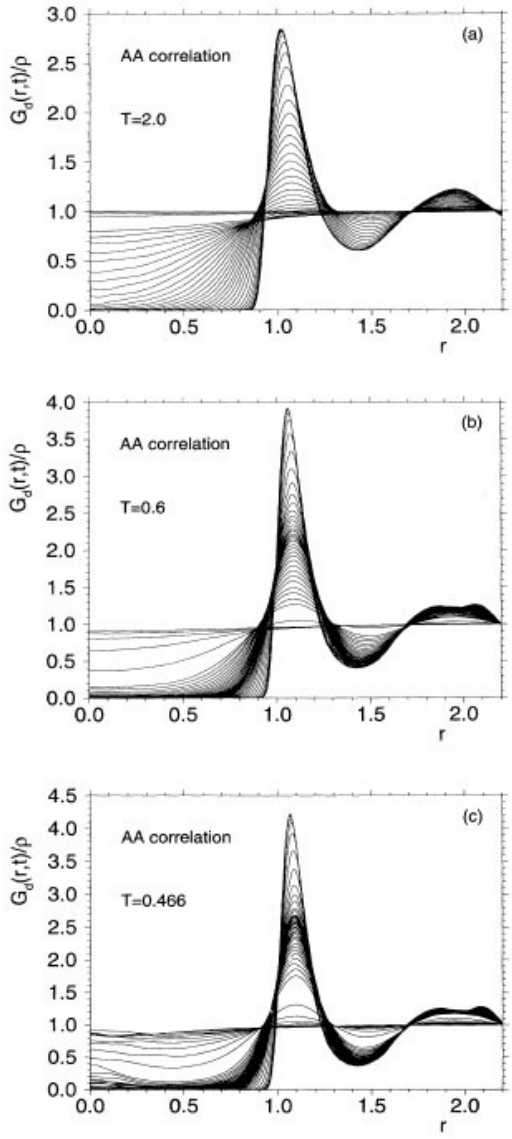

Figure 2.7: $G_d(r,t)/\rho$ for a simple liquid at different temperatures (28).

2.4 Features of the Glassy State

Some of the features of supercooled liquids and glasses viz. fragility, The Kauzmann Paradox and Boson peak are discussed below.

2.4.1 Fragility

C. A. Angell (29) proposed a very elegant way to compare and contrast the way viscosities of various glass formers depend on temperature above T_g such that viscosity data for all glass formers would intersect at their glass transition temperatures as shown in Figure 2.8.

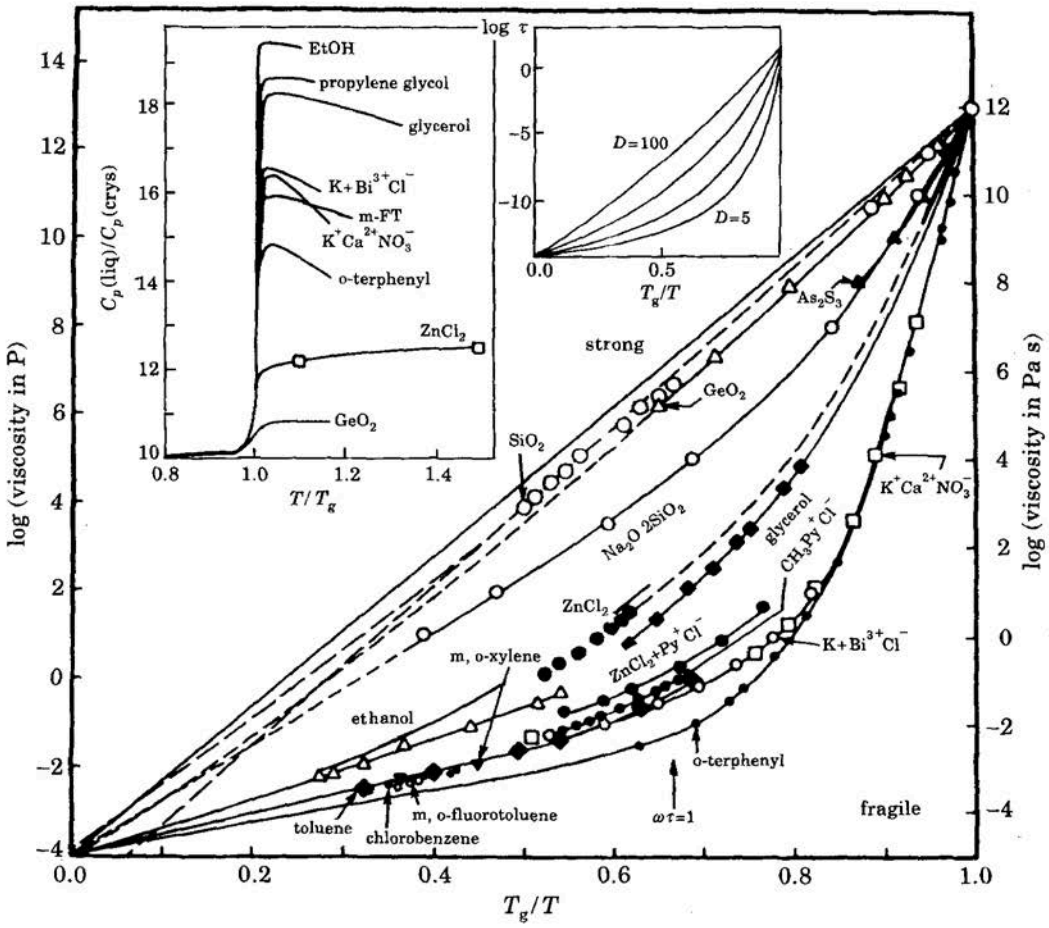

Figure 2.8: Angel plot of viscosity η for different glass-formers (29).

In the Angell representation $log(\eta)$ is plotted against T_g/T. Network-forming glasses such as SiO_2 (silica) and GeO_2 (Germania), show a mild dependence of η on

T_g/T, which can be approximately described by the Arrhenius law:

$$\eta(T) = \eta_\infty e^{E/T} \tag{2.25}$$

where η_∞ is the high temperature limit of the viscosity. Glasses, which show such behavior, are called strong in the Angell classification scheme. But, other glass formers such as o-terphenyl and tolune show an increase of η faster than Arrhenius (super-Arrhenius) upon super cooling. They are called fragile. The Vogel-Fulcher-Tammann (VTF) form (30) as given below in Eq.2.26 can be used to fit both extremes of temperature dependence of η.

$$\eta(T) = Ae^{[B/(T-T_0)]} \tag{2.26}$$

Here, A, B, and T_0 are fitting parameters. However, the VTF form when fitted to data often give unphysical values of the pre-factor A (31). Furthermore, there is evidence that shows that certain material undergo crossover from fragile to strong as the temperature is lowered (32; 33). The degree of super-Arrhenius behavior of a glass-forming material can be quantified by a physical quantity called fragility index, which is defined as (34):

$$m = \left.\frac{d(\log \eta)}{d(T_g/T)}\right|_{T=T_g} \tag{2.27}$$

It gives the steepness of the slope of $\log(\eta)$ dependence on T_g/T near T_g as shown in Figure 2.8. Typical values of fragility index, m, are 20(GeO_2), 53(glycerol), and 81(o-terphynyl) (35). One can also get fragility index by assuming the validity of specific functional form for $\eta(T)$ (36). Writing the VTF law given in Eq. 2.26 in another form as given in equation below (37) offers a way to get the material specific fragility index, K.

$$\eta(T) = \eta_\infty e^{[1/K(T/T_0-1)]} \tag{2.28}$$

Here, one has to understand that fragility is a qualitative concept and is not quantitative. Furthermore, we can understand from above discussion that something very subtle happens near the glass transition pointing that glass transition is more fundamental for fragile liquids rather than for strong liquids.

2.4.2 The Kauzmann Paradox

Walter Kauzmann pointed out the entropy crisis in the case of supercooled liquid which later came to known as Kauzmann paradox (38). The entropy, S, of a substance is given by:

$$S(N, V, E) = k_B \ln \Omega \tag{2.29}$$

Here, N, V, E and Ω are respectively number of particles, volume, energy and number of quantum states accessible to the system and k_B is the Boltzmann constant. This equation clearly shows that the entropy cannot be less than zero because Ω cannot be less than one. Crystal entropy becomes zero when the temperature, T, approaches 0 K. One of the odd characteristics of supercooled liquids arises when one compares the liquid entropy with the entropy of the crystalline substance at the same temperature. Near the melting point, the liquid entropy is much larger than the entropy of the crystal. It is seen that the entropy of the liquid decreases more

rapidly than the crystalline entropy; with decreasing temperature and we can expect a crossover at temperature T_K at which the liquid entropy would become less than the entropy of the crystal. This is a paradox, first pointed by Kauzmann in 1948, because a disordered liquid cannot have entropy less than an ordered crystalline state.

We only see this paradoxical situation when we extrapolate as shown in Figure 2.9, but before this can happen the glass transition intervenes and system entropy cannot decrease any more. As we know the glass transition temperature depends on the cooling rate and we can lower the glass transition temperature if the liquid is cooled slower. In other words, it is not necessary to have $T_g > T_K$ and also a liquid state can be maintained below T_K. A variety of solutions to this paradox have been proposed but without any success.

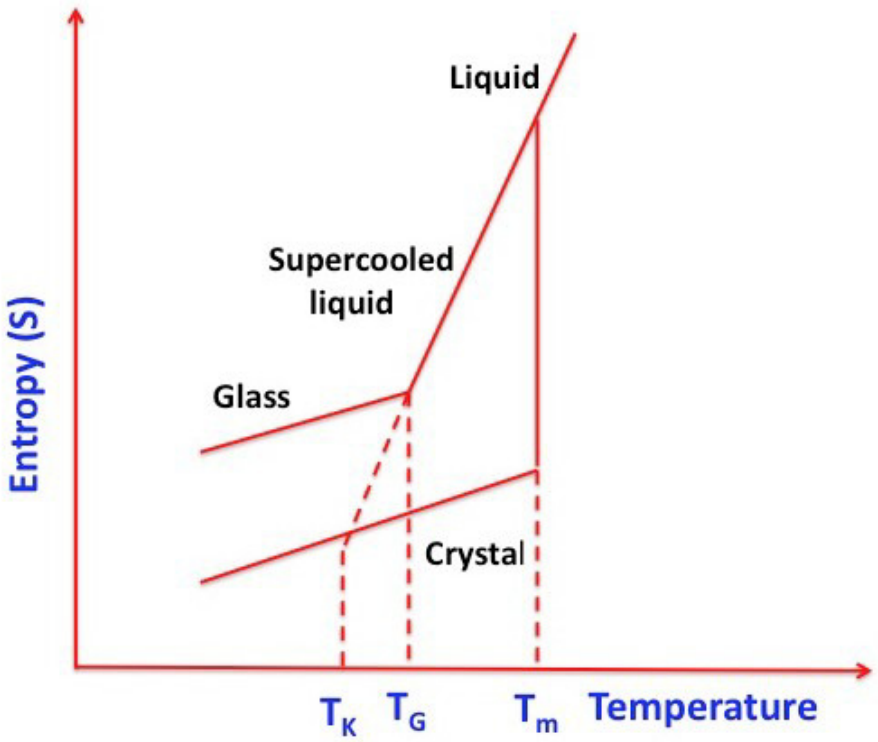

Figure 2.9: Kauzzmann Paradox.

One of the proposals suggests that there exists a genuine phase transition at T_K which may not be a true thermodynamic phase transition. This proposal assumes that the vibrational entropy of the liquid and crystal are roughly the same with the liquid having some additional configurational entropy. According to this proposal, at Kauzmann temperature the configurational entropy of the liquid becomes zero and it undergoes to a unique *ideal glass*. But this so called *ideal glass* has never been characterized.

2.4.3 Boson Peak

A universal feature that is observed in glasses and supercooled liquids is the presence of an excess of modes over Debye level in the density of vibrational states (DVOS). This universal feature is called Boson Peak (BP). The boson peak can be measured using inelastic Raman scattering or inelastic neutron scattering or heat capacity measurements. The difference between the neutron scattering and Raman scattering is that neutron scattering directly gives the vibrational density of states (VODS), $g(\omega)$ whereas in the Raman scattering the intensity is proportional to $g(\omega)$ multiplied by light-to-vibration coupling constant $c(\omega)$ as given below:

$$c(\omega) = \frac{g(\omega)c(\omega)[n(\omega)+1]}{\omega} \tag{2.30}$$

Here, $[n(\omega)+1]$ is called the Bose temperature factor. Here, $c(\omega)$ depends on the frequency in an unknown fashion (39). The comparison between neutron scattering and Raman scattering results show that $c(\omega)$ has universal linear frequency behavior near the boson peak maximum (39; 40; 41). In the one-phonon approximation, the incoherent dynamics structure factor, $S_{inc}(Q,\omega)$ is related to $g(\omega)$by a simple relation as shown below:

$$S_{inc}(Q,\omega) = \frac{3N\hbar}{2M} e^{-2W} Q^2 \frac{n(\omega)+1}{\omega} g(\omega) \tag{2.31}$$

where e^{-2W} is the Debye-Waller factor, $W = \frac{1}{6}Q^2 \langle u^2 \rangle$, $\langle u^2 \rangle$, is the mean square displacement, $n(\omega)$ is the Bose occupation factor, M is the mass of the scattering atoms and N is the number of scattering atoms (42).

It is clear from above equation that the incoherent part of dynamic structure factor varies as Q^2. The coherent part of dynamic structure factor depends on Q in non-trivial way. The two clear features of the boson peak that are seen in experiments are that it is asymmetric and it has universal shape for different glasses when normalized by the peak position and intensity as shown in Figure 2.10.

Likewise Figure 2.11 shows the phenomenon observed experimentally in he heat capacity measurements. Despite many studies on boson peak, the exact nature of excitation responsible for it is still far from solved.

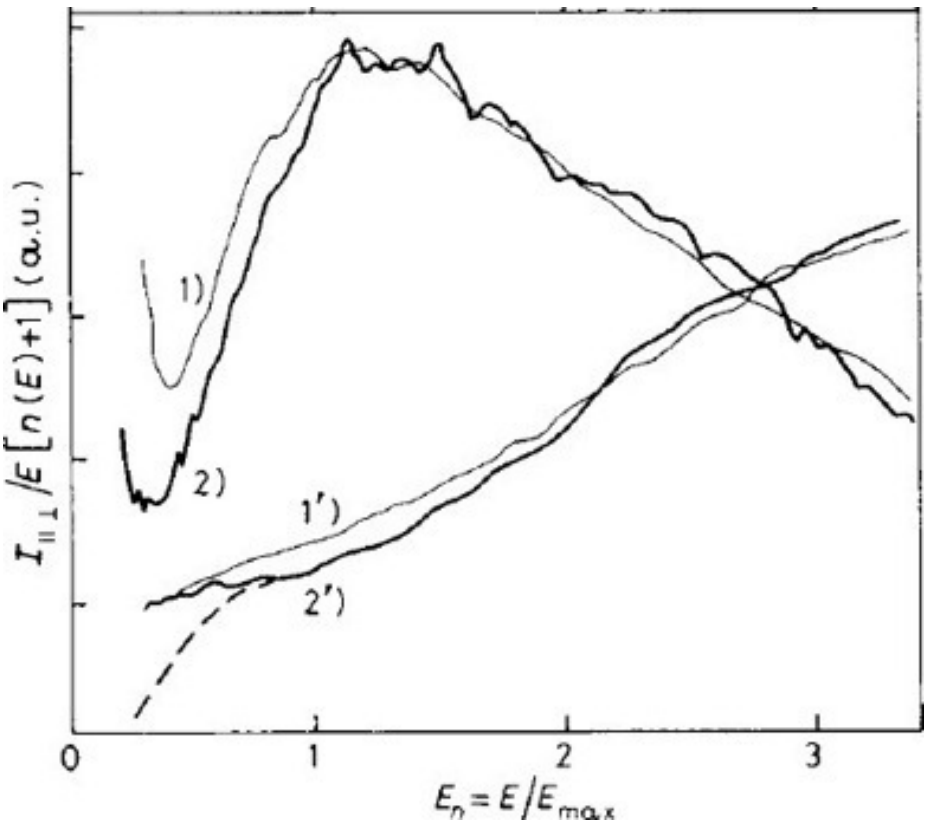

Figure 2.10: Raman spectra of glassy As_2S_3(1) and SiO_3(2) normalized to boson peak intensity and energy, together with light-to-vibration coupling coefficients c(ω)(1' and 2') (43).

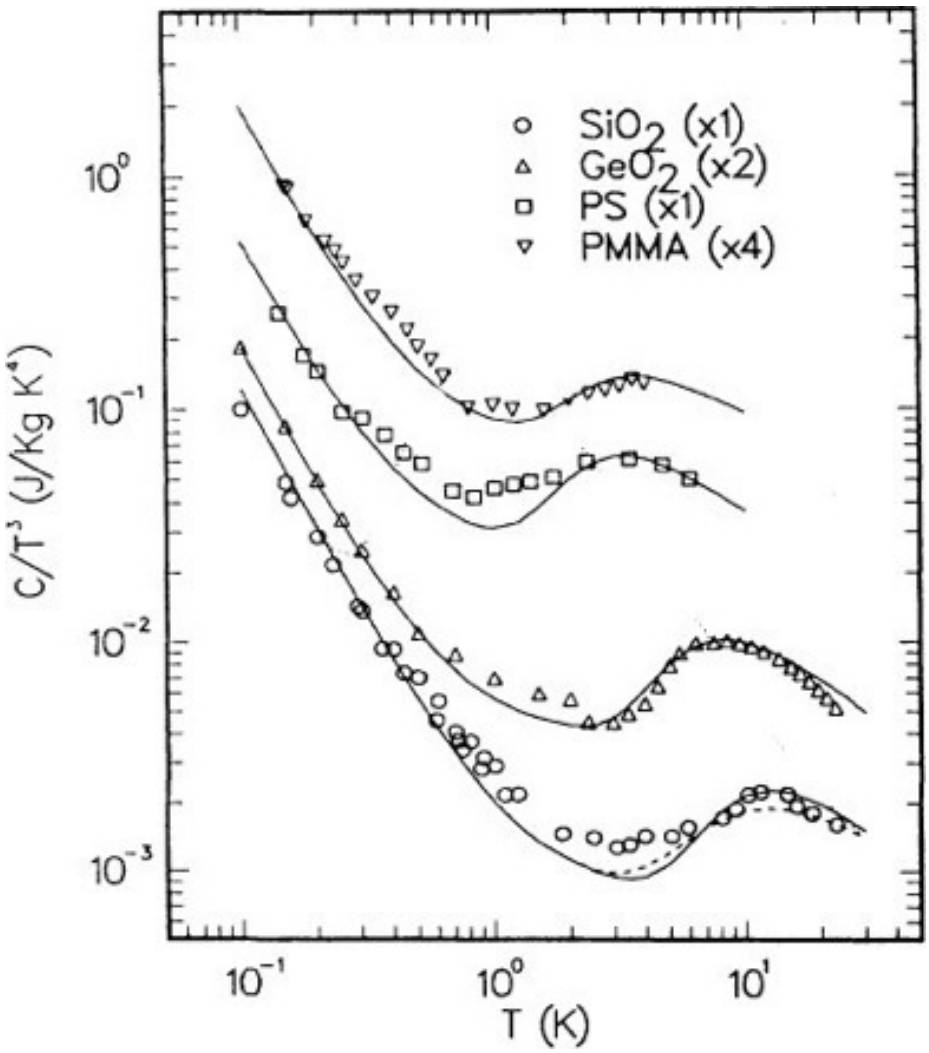

Figure 2.11: Heat Capacity Experiment on network and polymeric glass showing Boson peak (44).

2.5 Radiation Damage

2.5.1 Primary Damage

When a high-energy neutron is incident on a crystalline solid the atoms in the crystal undergo a series of elastic events called the primary radiation damage events or an atomic displacement cascade. The initial atom struck by the neutron is called the

primary knock-on atom (PKA). The PKA transfers its energy to the secondary knock-ons and the secondary knock-on atoms thereby give their energy to the third knock-on atoms and the process continues until all the KE of the PKA has been dissipated. Some energy is always required to displace an atom from its lattice site in a crystal. The minimum energy required to displace an atom from its lattice site is called displacement threshold energy (E_d). The value of the threshold energy depends on the material and the crystallographic direction. The typical values of E_d lies in the range 20 to 40 eV for most metals and alloys (45). For bcc iron the standard value is 40eV (46). In this collision process the atoms are displaced from their normal lattice sites whenever they get energy in excess of the displacement threshold energy leaving vacancies and lodging within the interstices of the lattice becoming interstitials. In this process an equal numbers of vacancies and interstitials are produced. A single stable vacancy and its related interstitial constitute a pair and is called a Frenkel pair. Thus, Frenkel pair formation occurs in an atomic displacement cascade and constitutes the primary radiation damage event in the irradiated material. The number of atoms displaced measures the extent of radiation damage to a material.

The primary damage event that triggers these changes lasts only a fraction of picosecond (ps) but the time required to bring the changes in the physical and mechanical properties could take a very long time. According to a simple but the most widely cited model proposed by Kinchin and Pease (47), the number of Frenkel pair produced by a given PKA is directly proportional to PKA energy between the threshold energy (E_d) and an upper cut-off energy (E_1). This model assumes that above the cut-off energy (E_1) additional energy is dissipated in electronic excitation and ionization. Another, widely used model is the NRT model (46). According to this model, the number of displaced atoms produced by given PKA with kinetic energy E_{PKA} is:

$$N_d = \frac{0.8T_d(E_{PKA})}{2E_d} \tag{2.32}$$

Here, T_d is called damage energy and is a function of E_{PKA} and is equal to the E_{PKA} minus the energy lost in electronic excitation and /or ionization.

2.5.2 Primary Damage Evolution

Due to the high number of vacancies and interstitials the highly damaged region of the material is highly disordered and even a local melting occurs for high PKA energy. Large number of the vacancies and interstitials recombine or annihilate if they are close to each other, this happens during the first few picoseconds (ps). The remaining Frenkel pairs leave the material in the disordered state with point defects. The mobility of the remaining Frenkel pair depends on temperature. They are immobile at low temperatures and there mobility increases with increase in temperature once they get energy in excess of migration energy of defects. They will annihilate when a vacancy comes close to an interstitial but they will form a cluster if they encounter defect of same kinds.

Radiation damage often brings undesired changes to material properties. Some of the properties that are often affected include physical dimensions, strength and hardness, electrical conductivity, conductivity of heat, magnetism, and corrosion resistance. It is observed that the mobility of interstitials is more than the vacancies and they have a tendency to move towards dislocations, grain boundaries or surfaces resulting in annihilation. On the other hand, the vacancies have the tendency to remain in the bulk and accumulate in growing voids thereby causing the material to swell. For example, radiation induced void swelling can bring more than 50% change in density in some grades of austenitic stainless steels (48). Similarly, radiation damage can change a ductile material to become hard and brittle and also it is observed that the ductile-to-brittle transition temperature can be changed by 200 degree Celsius in some low-alloy steel. Therefore, the study of radiation damage in solids is very important for nuclear technology to understand the service-life of any material to be used in nuclear reactors.

Chapter 3

Methods

3.1 Density Functional Theory

The exact many-particle Hamiltonian for a quantum mechanical system can be expressed as:

$$\hat{H} = -\frac{\hbar^2}{2}\sum_i \frac{\nabla_i^2}{m_i} - \frac{\hbar^2}{2}\sum_I \frac{\nabla_I^2}{M_I} - \sum_{i,I} \frac{Z_I e^2}{\left|\vec{r_i} - \vec{R}_I\right|} + \frac{1}{2}\sum_{i\neq j} \frac{e^2}{|\vec{r_i} - \vec{r_j}|} + \frac{1}{2}\sum_{I\neq J} \frac{Z_I Z_J e^2}{\left|\vec{R}_I - \vec{R}_J\right|} \tag{3.1}$$

Here, the first two terms are the kinetic energies of electrons (m_i is the mass of ith electron) and nuclei (M_I is the mass of Ith nucleus) respectively. Third term is the Coulomb interaction energy between the electrons ($\vec{r_i}, \vec{r_j}$) and nuclei ($\vec{R_i}, \vec{R_j}$). Here, e and Z_i, Z_j are electron charge and atomic numbers of atoms respectively. The fourth term is the coulomb interaction energies between the electrons and the last term is the Coulomb interaction energy between the nuclei. In the Born-Oppenheimer approximation the nuclei are much heavier than the electrons therefore above expression can be expressed as:

$$\hat{H} = -\frac{\hbar^2}{2}\sum_i \frac{\nabla_i^2}{m_i} - \sum_{i,I} \frac{Z_I e^2}{\left|\vec{r_i} - \vec{R}_I\right|} + \frac{1}{2}\sum_{i\neq j} \frac{e^2}{|\vec{r_i} - \vec{r_j}|} + \frac{1}{2}\sum_{I\neq J} \frac{Z_I Z_J e^2}{\left|\vec{R}_I - \vec{R}_J\right|} \tag{3.2}$$

The last term does not involve electron coordinates. Therefore, the Hamiltonian acting on electron coordinates is

$$\hat{H} = \hat{T}_e + \hat{V}_{ee} + \hat{V}_{eN} \tag{3.3}$$

where, $\hat{T}_e$ is the kinetic energy operator, $\hat{V}_{ee}$ is the electron-electron interation, and $\hat{V}_{eN}$ is the interaction between the electrons and nuclei.

Electron density, $\rho(\vec{r})$, is defined as:

$$\rho(\vec{r}) = N \int d^3r_2 \int d^3r_3 \cdots \int d^3r_N \psi^*(\vec{r}, \vec{r}_2 \cdots, \vec{r}_N)\psi(\vec{r}, \vec{r}_2 \cdots, \vec{r}_N) \tag{3.4}$$

To solve Schrödinger equation using the Hamiltonian given by equation (3.3) is computationally impossible for real physics problems that contains more than a few atoms.

3.1.1 Kohn-Sham Theorems

The Density functional theory which is widely used to solve many-body Shrödinger equation relies on two theorems by Hohenberg and Kohn (14). They proved that all features of electronic structures of a system of interest in a non-degenerate ground state are completely determined by its electron density.

The first theorem tells us that the ground state electron density $\rho(\vec{r})$ uniquely determines the corresponding external potential V_{ext}.

The theorem can be proved simply using the principle of *reductio ad absurdim* for a non-degenerate system. Let us consider a collection of electrons in a box in an external potential $V_{ext}(\vec{r})$=$V(\vec{r})$. We also suppose that the electron density of the system is known and it also determines $V_{ext}(\vec{r})$=$V(\vec{r})$ and thus all properties of the system. Now, let there be another potential $V'(\vec{r})$ which differ from $V_{ext}(\vec{r})$=$V(\vec{r})$ by more than a constant that can also give the same electron density $\rho(\vec{r})$ for the ground state. This implies that we will have two different Hamiltonians $\hat{H}$ and $\hat{H}'$ whose

ground state electron density is the same but the normalized wave functions ψ and ψ' would be different. Then we can write,

$$\begin{aligned} \mathrm{E}_0 &< \left\langle \psi' \middle| \hat{H} \middle| \psi' \right\rangle = \left\langle \psi' \middle| \hat{H}' \middle| \psi' \right\rangle + \left\langle \psi' \middle| \hat{H} \middle| \psi' \right\rangle - \left\langle \psi' \middle| \hat{H}' \middle| \psi' \right\rangle \\ &= \mathrm{E}'_0 + \int \rho(\vec{r})[V(\vec{r}) - V'(\vec{r})]d\vec{r} \end{aligned} \tag{3.5}$$

Here, E_0 and E'_0 are the ground state energies of $\hat{H}$ and $\hat{H}'$ respectively. Similarly,

$$\begin{aligned} \mathrm{E}'_0 &< \left\langle \psi \middle| \hat{H}' \middle| \psi \right\rangle = \left\langle \psi \middle| \hat{H} \middle| \psi \right\rangle + \left\langle \psi \middle| \hat{H}' \middle| \psi \right\rangle - \left\langle \psi \middle| \hat{H} \middle| \psi \right\rangle \\ &= \mathrm{E}_0 - \int \rho(\vec{r})[V(\vec{r}) - V'(\vec{r})]d\vec{r} \end{aligned} \tag{3.6}$$

This implies that $E_0 + E'_0 < E'_0 + E_0$, which is an obvious contradiction. So there is no different potential that can give the same electron density $\rho(\vec{r})$. Thus it is clear that $\rho(\vec{r})$ uniquely determines external potential $V(\vec{r})$ and all its ground-state properties.

We can determine the ground state wave function given that the external potential is known by solving the Schrödinger equation. We can say that it is also a unique functional of the electron charge density. Likewise, the ground state energy is also the unique functional of the electron charge density.

$$\begin{aligned} E[\rho(\vec{r})] &= \hat{T}_e[\rho(\vec{r})] + \hat{V}_{ee}[\rho(\vec{r})] + \hat{V}_{ext}[\rho(\vec{r})] \\ &= \int \rho(\vec{r}) V_{ext}(\vec{r}) d\vec{r} + T_e[\rho(\vec{r})] + V_{ee}[\rho(\vec{r})] \\ &= \int \rho(\vec{r}) V_{ext}(\vec{r}) d\vec{r} + F_{HK}[\rho(\vec{r})] \end{aligned} \tag{3.7}$$

Here, $F_{HK}[\rho(\vec{r})]$ is given by,

$$F_{HK}[\rho(\vec{r})] = T_e[\rho(\vec{r})] + V_{ee}[\rho(\vec{r})] \tag{3.8}$$

The second theorem of Kohn and Sham states that for a given external potential the energy functional assumes its minimum value, the ground state energy, for the correct ground state density.

$$E_0[\rho_0(\vec{r})] \leq E[\rho(\vec{r})] \tag{3.9}$$

This is a direct consequence of the unique relation between the ground state electron density, $\rho_0(\vec{r})$, and the ground state wave function, ψ, from first theorem of Kohn Sham and Ritz variational principle. Levy (49) gave a particularly simple proof of Hohenberg-Kohn theorems, based on the constrained search approach and it can be found in any standard book on DFT.

3.1.2 Kohn-Sham Equation

Publication of a paper in 1965 by Kohn and Sham transformed DFT into a practical electronic structure theory (15). Though the exact expression for the functional is not known, a simple approximation for the energy functional was put forward by Kohn and Sham as given below:

$$\mathrm{E}[\rho(\vec{r})] = \mathrm{T}_s[\rho(\vec{r})] + \frac{e^2}{2}\int \frac{\rho(\vec{r})\rho(\vec{r})}{|\vec{r}-\vec{r'}|}d\vec{r}d\vec{r'} + \int \rho(\vec{r})V_{ext}(\vec{r})d\vec{r} + E_{xc}[\rho(\vec{r})] \tag{3.10}$$

The equation may also be expressed as:

$$E[\rho(\vec{r})] = \mathrm{T}_s[\rho(\vec{r})] + \mathrm{E}^{Hartree}[\rho(\vec{r})] + \int \rho(\vec{r})V_{ext}(\vec{r})d\vec{r} + E_{xc}[\rho(\vec{r})] \tag{3.11}$$

where T_s is the KE functional of the non-interacting electrons, ρ is the electron density, V_{ext} is the potential due to nuclei and any other external fields, and E_{xc} is the unknown exchange-correlation functional.

We can define an effective potential as:

$$V^{eff} = \frac{\delta\{\int d\vec{r}\rho(\vec{r})V_{ext}(\vec{r}) + E^{Hartree}[\rho(\vec{r})] + E_{xc}[\rho(\vec{r})]\}}{\delta\rho(\vec{r})} = V_{ext}(\vec{r}) + \int \frac{\rho(\vec{r}')}{|\vec{r} - \vec{r}'|} d\vec{r}' + V_{xc}(\vec{r}) \tag{3.12}$$

Here, $V_{xc}(\vec{r})$ is the exchange-correlation potential:

$$V_{xc}(\vec{r}) = \frac{\delta E_{xc}[\rho(\vec{r})]}{\delta\rho(\vec{r})} \tag{3.13}$$

This formulation by Kohn and Sham results into a one-electron SE form:

$$\left[\frac{-\hbar^2}{2}\nabla^2 + V^{eff}\right]\psi_i = \varepsilon_i\psi_i \tag{3.14}$$

Here, ψ_i are called Kohn-Sham one-electron orbitals which satisfy:

$$\rho(\vec{r}) = \sum_{i}^{\varepsilon_i < \varepsilon_F} |\psi_i|^2 \tag{3.15}$$

3.1.3 Exchange-correlation Functional

It is clear that Kohn-Sham formalism is exact provided we have the knowledge of correct exchange-correlation functional. Unfortunately its exact form is unknown. Thus, from the very early state of DFT some sort of approximations for E_{xc} have been used.

Local-Density Approximation(LDA)

In the local density approximation (LDA) approach the system is divided into infinitesimal volumes, and the electron density, $\rho(\vec{r})$, in each of the volumes is taken to be a constant. This approximation assumes that the exchange-correlation energy functional is purely local and hence the corrections to the exchange-correlation energy due to inhomogeneity in electron density can be ignored. The exchange-correlation energy in the LDA approach can be expressed as:

$$E_{xc}^{LDA}[\rho(\vec{r})] = \int \rho(\vec{r})\varepsilon_{xc}^{unif}(\rho(\vec{r}))d\vec{r} \tag{3.16}$$

Here, ε_{xc}^{unif} is the exchange-correlation energy density of electron gas with density $\rho(\vec{r})$. It has two parts viz. exchange part, $\varepsilon_{x}^{unif}(\rho)$ and correlation part, $\varepsilon_{c}^{unif}(\rho)$. The first part is exact known from Hartree-Fock and the second part can be calculated using quantum Monte Carlo.

Generalized Gradient Approximation(GGA)

Improvements to LDA can be achieved by including the gradient of the density, $\nabla\rho(\vec{r})$, as well as the density itself to the exchange-correlation functionals as shown below:

$$E_{xc}^{GGA}[\rho(\vec{r})] = \int \rho(\vec{r})\varepsilon_{xc}^{GGA}[\rho(\vec{r}), \nabla\rho(\vec{r})]d\vec{r} \tag{3.17}$$

GGAs are often called "semi-local" functionals due to their dependence on $\nabla\rho(\vec{r})$. We might think that because GGA includes more physical information than the LDA it must be more accurate. Actually, this is not always true.

As there are different ways in which information from the gradient of the electron density can be included in a GGA functional, there are large numbers of different GGA functionals. Becke (B88) (50), Predrew-Wang functional (PW91) (51) and the Perdrew-Burke-Ernzerhof functional (PBE) (52) are three of the GGA functionals that are widely used. Generally when reporting calculations using DFT it is general practice to mention the functional used in the calculation as different functionals give somewhat different results for particular configuration of atoms.

To do electronic structure calculations using DFT the following steps are followed.

1. Initial trial electron density, $\rho(\vec{r})$, is defined.

2. Kohn-Sham equation is solved using the potential (Eq. 3.12) corresponding to the trial electron density defined in step 1 and the single-particle wave functions $\psi_i(\vec{r})$ are found.

3. Once single particle wave functions obtained from step 2 is used to calculate the electron density $\rho_{KS}(\vec{r}) = \sum_i |\psi_i(\vec{r})|^2$.

4. The calculated electron density is compared with trial electron density. If the densities are different, then the trail electron density must be updated in some way and the process begins again from step 1 but if the two densities are the same within a specified tolerance then the ground-state electron density has been obtained and the calculation is stopped.

3.2 Multiple Scattering Theory

Multiple scattering theory (MST) provides a general approach for calculating electronic structure in solids. MST was first introduced by Lord Rayleigh in 1892 (53). It has been applied to wide variety of systems. Korringa applied MST to calculate the electronic states in crystals (54). Korringa's results were later verified and re-derived by Kohn and Rostoker in 1954 (55) and became the basis of the KKR band theory methods (56; 57; 58).

3.2.1 Multiple-Scattering Theory Equations

A solid can be described as a collection of individual scatterers characterized by non-overlapping spatially bounded potentials, v_i, centered at lattice position $\vec{R}_i$. In multiple scattering theory the effective potential, $V(\vec{r})$, is written as a sum of non-overlapping potentials $v_i(\vec{r} - \vec{R}_i)$ centered on each of the atomic sites (59),

$$V(\vec{r}) = \sum_{i=1}^{N} v_i(\vec{r} - \vec{R}_i) = \sum_{i=1}^{N} v_i(\vec{r}_i) \; ; \; \vec{r}_i = \vec{r} - \vec{R}_i \tag{3.18}$$

In the spherical approximation, potentials $v_i(\vec{r} - \vec{R}_i)$ are assumed to be zero outside the bounding sphere of radius S_i i. e.,

$$\mathrm{v}_i(\vec{r}_i) = \begin{cases} \mathrm{v}_i(r_i) & if\ r_i < S_i \\ 0 & if\ r_i > S_i \end{cases} \tag{3.19}$$

Here, each electron propagates like a free particle between the sites. The most general MST one-electron Greens function for the crystal, for $|\vec{r}| > |\vec{r}'|$ (i.e. valid for inside or outside the bounding sphere) can be expressed as (60).

$$G(E, \vec{r}, \vec{r}') = \sum_{L,L'} Z_L^i(E, \vec{r}) \tau_{LL'}^{ij}(E) Z_{L'}^i(E, \vec{r}') - \sum_L Z_L^i(E, \vec{r}) J_L^i(E, \vec{r}') \tag{3.20}$$

In the above equation $Z_L^i(E, \vec{r})$ and $J_L^i(E, \vec{r}')$ are regular and irregular solutions of the Schrödinger equation in the ith Wigner-Seitz cell, L stands for the pair of angular momentum indices l and m and $\tau_{LL'}^{ij}(E)$ (61) are the scattering path matrices and describe the propagation of the electron around all paths in the solid that begins at on site j and end on site i. The superscripts on the scattering path matrices refer to the cells centered at the lattice sites $\vec{R}_i$ and $\vec{R}_j$, the subscripts are the usual angular momentum indices. Here,

$$\tau^{ij}(E) = t_i(E)\delta_{ij} + \sum_{k \neq i} t_i(E) G(\vec{R}_i - \vec{R}_k; E) \tau^{ik}(E) \tag{3.21}$$

It carries all the information about the scattering processes within the solid. The scattering path matrix can be calculated by inverting the Matrix **M**.

$$\tau^{ij} = \left(M^{-1}\right)^{ij} \tag{3.22}$$

The matrix **M** is given as,

$$M_{LL'}^{ij} = m_i \delta_{LL'} \delta_{ij} - G_{LL'}^{ij} \tag{3.23}$$

$$M(E) = \begin{pmatrix} t_0^{-1} & -G^{01}(E) & \dots & -G^{0M}(E) \\ -G^{10}(E) & t_1^{-1} & \dots & -G^{1M}(E) \\ \vdots & \vdots & \ddots & \vdots \\ -G^{M0}(E) & \cdots & \cdots & t_M^{-1} \end{pmatrix} \tag{3.24}$$

The single site t-matrix is given by,

$$t_{LL'} = -\frac{1}{2i\kappa}(e^{2i\eta_l(E)} - 1)\delta_{ll'}\delta_{mm'} \tag{3.25}$$

The matrix $\mathbf{m}$ is the inverse of the scattering t-matrix for the atoms on site i. The only non-zero elements of matrix $\mathbf{m}$ are diagonal blocks corresponding to $i = j$. If the potential is spherically symmetric then the elements of matrix $\mathbf{m}$ are given by,

$$m^i_{LL'} = (-\kappa \cot \eta^i_l + i\kappa)\delta_{LL'} \ (\kappa = \sqrt{E}) \tag{3.26}$$

Here, the phase shifts η_l contain all the scattering information and are energy dependent. The structural Green functions G are defined in the real space as,

$$G^{ij}_{LL'}(E) = -4\pi\kappa i^{l-l'+1} \sum_{L''} C^{L''}_{LL'} i^{-l''} h^+_{l''}(\kappa \left|\vec{R}_i - \vec{R}_j\right|) Y_{L''}(\vec{R}_i - \vec{R}_j)(1 - \delta_{ij}) \tag{3.27}$$

It is clear that the matrix elements of diagonal blocks ($i = j$) are equal to zero. The gaunt factors $C^{L''}_{LL'}$ are given by,

$$C^{L''}_{LL'} = \int Y_L(\Omega) Y^*_{L''}(\Omega) Y_{L'}(\Omega) \tag{3.28}$$

Here, Y_L and h_l^+ are respectively spherical harmonics and Hankel functions and $L = l, m$. The Gaunt factors are non-zero only if $l + l' + l''$ is even. Furthermore, they also vanish unless $\left|l - l'\right| < l'' < l + l'$ and $m + m' = m''$

Generally MST equations are truncated at some maximum angular momentum because the scattering of high angular momentum states is quite small. For l_{max} of 3 or 4 a good convergence is obtained. If N be the number of atoms in a crystal, the dimension of matrix M are $N(l_{max}+1)^2 \times N(l_{max}+1)^2$ and the matrix elements $\tau_{LL'}^{ij}$ are the elements of matrix $\mathbf{M^{-1}}$. In MST we can separate potential dependent quantities and geometry dependent quantities. Because of this separation the geometrical dependent quantities can be calculated just once for a given geometry.

When the Green's function is calculated using Eq. 3.20, different parameters that are used to describe the electronic structure of a system can be obtained from it. In other words MST can be used to calculate physical properties of solids directly using Green's function.

Density of states is given by,

$$n(E) = -\frac{1}{\pi} \operatorname{Im} \int_{\Omega_{ws}} G(\vec{r}, \vec{r}', E) d\vec{r} \tag{3.29}$$

Similarly, charge density and magnetization density are given by,

$$\rho(\vec{r}) = -\frac{1}{\pi} \operatorname{Im} \int_{-\infty}^{E_F} TrG(\vec{r}, \vec{r}', E) dE \tag{3.30}$$

$$m(\vec{r}) = -\frac{1}{\pi} \operatorname{Im} \int_{-\infty}^{E_F} TrG(\vec{r}, \vec{r}', E) \vec{\sigma} dE \tag{3.31}$$

Evaluation of magnetization density requires implementation of spin. The sum of one-electron eigenvalues is given by,

$$\Sigma = \int_{-\infty}^{E_F} E\ n(E) dE \tag{3.32}$$

In above equations E_F is Fermi energy and Ω_{ws} is the volume of volume of Wigner-Seitz cell. We are assuming the use of the Atomic Sphere Approximation (ASA).

Usually, above quantities are difficult to calculate directly using equation 3.20 because $G(E, \vec{r}, \vec{r}')$ varies rapidly with energy. We can view the Green's function as a function of complex energy $G(z, \vec{r}, \vec{r}')$. As a function of complex energy they are holomorphic everywhere except for poles at the bound states. So integration can be done with a cut on the part of the real axis starting at lowest eigenvalue in the conduction band and ending at E_F with a contour in the upper half plane (62).

3.2.2 Muffin-Tin and Atomic Sphere Approximation

In MST there is no restriction on the shape of the individual potentials but it is always easier to apply MST if the potentials possess spherical symmetry.

In the simplest Muffin-Tin (MT) approximation method atomic cells are divided into two regions viz. muffin-tin (MT) and interstitial. The potential is spherically symmetric inside the MT region and it is assumed constant outside the muffin-tin sphere i.e. in the interstitial region.

In another approximation called Atomic Sphere Approximation (ASA), the space is approximated by a collection of spheres centered at the nuclei, whose volume equals to the volume of the corresponding atomic cell. In this approximation the spheres overlap but do so only slightly and the effects of overlapping are expected to be small. In this approximation the interstitial region, which was present in muffin-tin approximation is removed. In this case our integration over space becomes an integration of atomic spheres. This approximation is suitable when the system is

close packed and we know that many crystals are close-packed in fcc, bcc and hcp lattices. Otherwise, we need to pack the system with empty spheres to apply MST.

3.3 The Locally Self-Consistent Multiple Scattering Theory(LSMS) Method

There are some important classes of problems in which we have to treat the interaction between large number of atoms (hundreds or even thousands) using ab initio calculations. Examples include disordered or amorphous alloys, grain boundaries, surface and interface structures etc. In such problems we generally need a very large unit cell (super cell) with very large number of atoms. In conventional calculations using LDA the time required to do electronic structure calculations with N number of atoms in a unit cell is proportional to N^3. It is unrealistic to carry out calculation in such systems even with very powerful computers. Due to the progress in parallel computing the development of order-N (computational time is linearly proportional to the number of atoms, N, in the system) calculation in such a system is feasible.

The locally self-consistent multiple scattering (LSMS) method takes advantage of very modern massively parallel supercomputers to handle clusters with thousands of atoms using parallel algorithms (17). The developers of the LSMS code have been awarded Gordon Bell prize two times to recognize the power, performance and speed of the method. LSMS is based on the analytic properties of the single particle Greens function and the stationary properties of a LDA free energy functional (18). LSMS applies electronic multiple scattering process in a finite spatial region centered at each atom and the cluster of M atoms in this region is called local interaction zone (LIZ) of its central atom.

It assumes that a good approximation to the electron density, and density of states (DOS), on the site at the center of an LIZ, and consequently the total energy, E, of the system can be achieved only by calculating multiple scattering within the LIZ. In

the LSMS scheme, every atom in the system is considered to be at the center of its own LIZ. In this approach one can obtain an approximation to the electron density and density of states associated with every atom in the system. We can reconstruct the potential by solving Poisson's equation for a crystal electron density made up of a sum of the single site densities. This reconstructed potential now can be used in the next iteration of the self-consistent field (SCF) calculation.

Thus, in the LSMS approach the electron-structure calculation problem is reduced to that of calculating the single particle Greens function at the central atom of a LIZ. In other words LSMS assigns a compute node to each site in the system to decompose the N-atom problem into N linked sub-problems and it approximates the electron density and the density of states (DOS) on each site by considering the scattering process in a cluster of M atoms within a LIZ. Generally in LSMS approach calculation of the single-site quantities are assigned to each node. Therefore, each node has to invert a matrix of dimension $(l_{max}+1)^2 M$. Thus, in LSMS the overall scaling is proportional to $M^3 N$.

3.3.1 LSMS Algorithm

An LSMS algorithm with one atom per node implementation scheme is shown schematically in Figure 3.1. Let us consider an atom i in the N atom system. In the first step, an initial guess for the potential, and electron density, , at this site i of this atom, and the positions of all the atoms, are fed to the i^{th} node. Each node gets information about all the nodes within its LIZ. Once this information is obtained each node calculates the t-matrix corresponding to potential at site i.

Also, at this point, it receives the t-matrices from other nodes and it also sends its own t-matrix to the nodes for which it is one of the atoms in the other nodes's LIZ. The node at this point has all the information to calculate the scattering path matrix and electron density. After this, total electron density and the potential for next iteration are constructed. This self-consistency cycle is repeated until convergence is reached.

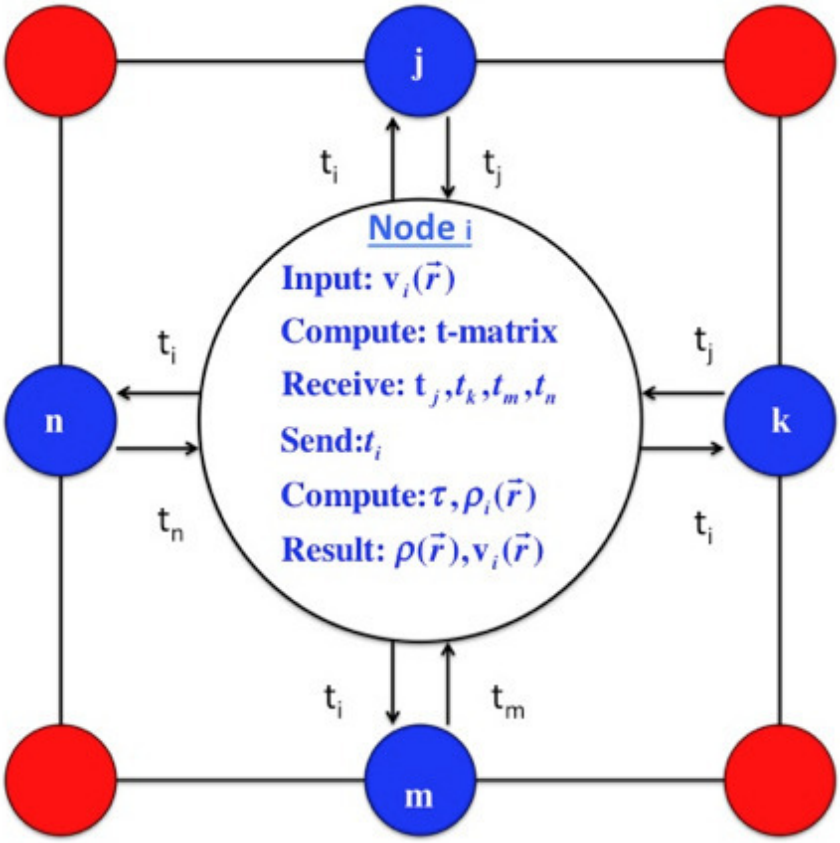

Figure 3.1: Schematic of a parallel SCF algorithm.

3.4 Dynamic Pair-Density Function

Dynamic pair-density function was initially proposed by Prof. Egami as a characterization tool to describe atomic dynamics in materials (9; 10). An inelastic neutron scattering measurement gives the dynamic structure factor, which is defined as:

$$S(Q,E) = \frac{1}{N\langle b\rangle^2}\sum_i\sum_j b_i b_j \left\langle\left\langle e^{i\vec{Q}.(\vec{R}_i(0)-\vec{R}_j(t))}\right\rangle\right\rangle e^{-i\omega t} \tag{3.33}$$

Here, $\vec{Q}$ and $E = \hbar\omega$ are respectively the momentum and energy transfer of scattering, b_i is the neutron scattering length of the i^{th} atom, $\langle....\rangle$ and $\langle\langle....\rangle\rangle$ are respectively the thermal average and ensemble average and $\vec{R}_i$ is the position of the i^{th} atom at time t. It describes the probability with which a neutron can transfer the energy $\hbar\omega$ and momentum $\vec{Q}$ to the sample and thus contains information about the structure of the sample and the dynamics. The van Hove correlation function, $G(\vec{r},t)$, which is linked to by Fourier transformation is given by:

$$\begin{aligned} G(\vec{r},t) &= \int S(\vec{Q},E)e^{-i(\vec{Q}.\vec{r}-\omega t)}d\vec{Q}dt \\ &= \frac{1}{N\langle b\rangle^2}\sum_i\sum_j b_i b_j \left\langle\left\langle \delta(\vec{r}-(\vec{R}_i(0)-\vec{R}_j(t))\right\rangle\right\rangle \end{aligned} \tag{3.34}$$

This function is not very frequently used in neutron scattering, as there is no direct method of measuring this quantity experimentally. But, the function that is most frequently used in the neutron scattering community is the intermediate scattering function, which is obtained by partial Fourier transform of over energy as shown below:

$$\begin{aligned} F(\vec{Q},t) &= \int S(\vec{Q},\omega)e^{i\omega t}dE \\ &= \frac{1}{N\langle b\rangle^2}\sum_i\sum_j b_i b_j \left\langle\left\langle e^{i\vec{Q}.(\vec{R}_i(0)-\vec{R}_j(0))}\right\rangle\right\rangle \end{aligned} \tag{3.35}$$

This function is frequently used in the analysis of the neutron scattering data. It was proposed (9; 10) that a more informative partial correlation function could be

the Dynamic pair-density function (DPDF), which can be obtained by partial Fourier transform of $S(\vec{Q}, E)$ over energy as shown below:

$$\begin{aligned} \rho(\vec{r}, E) &= \int S(\vec{Q}, E) e^{-i\vec{Q}.\vec{r}} d\vec{Q} \\ &= \frac{1}{N\langle b \rangle^2} \int \sum_i \sum_j \left\langle \left\langle e^{i\vec{Q}.(\vec{R}_i(0) - \vec{R}_j(0))} \right\rangle \right\rangle e^{-i(\omega t - \vec{Q}.\vec{r})} d\vec{Q} \end{aligned} \tag{3.36}$$

Equivalently, we can also obtain the dynamic pair-density function by Fourier transforming :

$$\begin{aligned} \rho(\vec{r}, E) &= \int G(\vec{r}, t) e^{i\omega t} dt \\ &= \frac{1}{N\langle b \rangle^2} \sum_i \sum_j b_i b_j \left\langle \left\langle \delta \left[(\vec{r} - (\vec{R}_i(0) - \vec{R}_j(t))) \right] \right\rangle \right\rangle e^{i\omega t} dt \end{aligned} \tag{3.37}$$

Furthermore, the elastic component of the dynamic PDF gives the time averaged pair-density function whereas the energy integral of DPDF gives the instantaneous pair-density function as shown below.

$$\rho(\vec{r}, 0) = \frac{1}{N\langle b \rangle^2} \int \sum_i \sum_j b_i b_j \left\langle \left\langle \delta[\vec{r} - (\vec{R}_i(0) - \vec{R}_j(t))] \right\rangle \right\rangle dt \tag{3.38}$$

$$\begin{aligned} \rho_{ins}(\vec{r}) &= \int \rho(\vec{r}, E) dE \\ &= \frac{1}{N\langle b \rangle^2} \sum_i \sum_j b_i b_j \left\langle \left\langle \delta[\vec{r} - (\vec{R}_i(0) - \vec{R}_j(0))] \right\rangle \right\rangle \end{aligned} \tag{3.39}$$

Recently, the method of dynamic pair-density function was implemented to study polycrystalline nickel and relaxor ferroelectric PMN (11). Using the method of DPDF the authors reported that the intensity of the DPDF peak is augmented for localized or non-dispersive modes with high density of states. Thus, it is claimed that the method of DPDF is an ideal technique to study localized phonons in disordered materials like liquids, glasses where phonons are scattered and have a very short lifetime as compared to crystalline samples.

3.5 Theory of Atomic Level Stress

In order to describe the atomic environment reasonably the concept of atomic-level stress, which results from the incompatibility between a given atom and its surroundings, was introduced (12). A perfect crystal at absolute zero with one atom per unit cell we will not observe any atomic-level stress. But, even in perfect crystals atomic-level stresses appear due to lattice vibrations and lattice defects. The theory assumes that in the case of liquids and glasses the atoms are not ideally packed as in the case of a closed packed structure. Because of this situation in the case of liquids and glasses the atomic environment of each atom is sharply altered and each atom is under stress. The atomic level stress is defined as (12):

$$\sigma_i^{\alpha\beta} = \frac{1}{\Omega_i} \sum_{j \neq i} f_{ij}^{\alpha} r^{\beta}{}_{ij} \tag{3.40}$$

Here α and β are Cartesian coordinates, f_{ij}^{α} is the α component of the two-body force between atoms i and j, and r_{ij}^{β} is the β component of the distance vector between atoms i and j; Ω_i is Voronoi Polyhedra volume of i^{th} atom.

We can expand any pair-wise interatomic potential $V(r)$ around the potential minimum at $r = r_0$ as shown below:

$$V(r) = V(r_0) + A\left(\frac{r}{r_0} - 1\right)^2 + B\left(\frac{r}{r_0} - 1\right)^3 + ... \tag{3.41}$$

Where A and B are constants and for most of the potentials $A > 0$ and $B < 0$. For a system interacting by pair-wise potential $B = 0$ in Eq. 3.41. Using Eq. 3.41 for the case of pair-wise potential in Eq. 3.40 we get,

$$\sigma_i^{\alpha\beta} = \frac{2A}{V_i} \sum_{j \neq i} \left(\frac{r_{ij}}{r_0} - 1\right) r_{ij}^{\alpha} r_{ij}^{\beta} \tag{3.42}$$

Thus, from the atomic level stress we get information about the environment of the atom away from the ideal environment, where all neighbors are at $r_{ij} = r_0$. The

atomic level stress is a nine-component tensor of which six are independent and the trace of atomic level tensor gives the pressure (12).

Even though the theory was initially proposed to define the intangible defects in the glassy structures, it has now found a broader usefulness. This theory was effectively used in calculating the composition limit of glass formation in binary glasses (63).

Nielsen and Martin (64; 16) showed that the total macroscopic stress could be written as a sum of expectation values of certain operators defined at individual particles in general quantum mechanical case. According to them, the Hamiltonian can be expressed as:

$$\widehat{H} = \sum_i \frac{\widehat{P}_i}{2m_i} + \widehat{V}_{\text{int}} \tag{3.43}$$

where $\hat{P}_i$ and m_i are respectively the momentum operator and mass of the i^{th} particle and $\widehat{V}_{\text{int}}$ is the interaction energy of the system. Here i denotes both nuclei and electrons. The total stress is given by:

$$\sigma^{\alpha\beta} = \sum_i \left\langle \psi \left| r_i^{\beta} \frac{dV_{\text{int}}}{dr_i^{\alpha}} - \frac{p_i^{\alpha} p_i^{\beta}}{m_i} \right| \psi \right\rangle \tag{3.44}$$

Here, r_i^{α}, r_i^{β}, p_i^{α} and $p_i^{\beta}$are the Cartesian components of position and momenta of i^{th} particle respectively and ψ is the exact eigen function of the Hamiltonian.

It is more appropriate if we can define stress averaged over an appropriate local atomic volume. In this dissertation work we are defining atomic level stress using first principle calculation averaged over Voronii polyhedral volume of an atom ((Wigner-Seitz cell of an atom).

The evaluation of atomic level stress depends on the method to calculate the total energy of the system. We can use, density functional theory (DFT), or embedded atom method, or simple pair potential. It is convenient if the total energy of the system can be decomposed to atomic contributions, i.e.,

$$E_{system} = \sum_{i=1}^{N} E_i \text{ with } \sigma_i^{\alpha\beta} = \frac{\delta E}{\delta \varepsilon^{\alpha\beta}} \tag{3.45}$$

Here, in this dissertation work we have followed this approach to calculate the total energy and atomic level stress from first principle. The details about our approach will be presented in chapter six.

3.6 Molecular Dynamics Simulation

3.6.1 Background and History

Molecular dynamics simulation is based on Newtons equations of motion. For a system of N interacting atoms the potential and acceleration are related:

$$\vec{F_i} = m_i \frac{d^2 \vec{r_i}}{dt^2} = -\overrightarrow{\nabla}_i V \tag{3.46}$$

Here, $\vec{F_i}$ is the force on atom i of mass m and V is the interatomic potential of the system describing the interaction present. It is clear that MD method depends on the interatomic potential, which can describe the energy of the system and the forces on each atom as a function of its position relative to the other atoms of the system. In statistical mechanics, the ensemble average is given by,

$$\langle A \rangle_{ens} = \frac{\int d\vec{p}_i^N d\vec{r}_i^N A(\{\vec{P}_i\}, \{\vec{r}_i\}) \exp[-H(\{\vec{P}_i\}, \{\vec{r}_i\})/k_B T]}{\int d\vec{p}_i^N d\vec{r}_i^N \exp[-H(\{\vec{P}_i\}, \{\vec{r}_i\})/k_B} \tag{3.47}$$

In Eq. 3.47 $\vec{p_i}$ and $\vec{r_i}$ are respectively linear momentum and position of the i^{th} particle of the system. In molecular dynamics simulation the time average is given by,

$$\langle A \rangle_{time} = \lim_{\tau \to \infty} \frac{1}{\tau} \int_{t_0}^{t_0+\tau} A(\{\vec{P}_i\}, \{\vec{r}_i\}) dt \approx \frac{1}{M} \sum_{i=1}^{M} A(\{\vec{P}_i\}, \{\vec{r}_i\}) \tag{3.48}$$

In Eq. 3.48 τ is the simulation time and M is the total number of time steps. According to Ergodic hypothesis,

$$\langle A \rangle_{ens} = \langle A \rangle_{time} \tag{3.49}$$

This is only valid if the system is in equilibrium. Thus by MD simulation one can calculate different observables.

Alder and Wainwright first introduced molecular dynamics simulation in 1957 (65). In 1964 Rahman successfully carried out MD simulation of a collection of argon atoms interacting with Lennard-Johnes potential (66) which was more realistic compared to the system of hard spheres of Alder and Wainwright colliding elastically and moving with constant speed between the collisions.

During the four decades of time since Rahman worked with a model of 864 atoms much progress has been achieved in terms of computing power that now we can easily carry out MD simulation of a system with multi million atoms in a time of few hours using super computers that use parallel computing.

3.6.2 Equations of Motion

When the suitable interatomic potential for a system is chosen, the total energy of the system can be calculated by summing over all atoms in the system. The forces on each atom is given by the gradient of the interatomic potential as given in Eq. 3.46. These forces can be used to calculate each atom's acceleration according to Newtons second law ($F = ma$). The equations of motion of for every atom of the system can be solved by numerical integration using an appropriate time step. The forces are recalculated at the end of each time step for new atomic positions and this process is continued till we reach desired total time of simulation.

3.6.3 Solution of Equation of Motion: Integration Algorithm

An integrator advances the trajectory of atom over small time increments. Various integration algorithms are used depending on the nature of the problem and also on the desired accuracy. Some of the widely used algorithms are: central difference methods (Verlet, Leap Frog, Velocity Verlet, Beeman) (67; 68) and predictor-corrector methods (69). In this dissertation work fifth order predictor corrector method is used to integrate the equations of motion.

3.6.4 Periodic Boundary Condition

Normally, in molecular dynamics (MD) simulation the system is enclosed in a box (simulation box) although other configurations exist. The size of this simulation box is usually chosen depending on the nature of the problem, storage capacity and speed of the computing resources. But, the number of atoms within this box is far below Avogadros number ($N_A = 6.02 \times 10^{23}$). Therefore, to simulate bulk environment with small number of atoms compared to Avogadros number, periodic boundary condition (PBC) are normally used (67). Without using PBC surface effects will normally affect simulated bulk properties. Periodic boundary conditions are used to mimic an infinite bulk lattice. PBC attach the simulation box to its own images side by side. Figure 3.2 shows schematically shows PBC in two-dimensional box.

The middle portion in grey color is the simulation box and the other white boxes are the images. When simulation starts and an atom near the boundary of the central box leaves the simulation box, its image enters the box at the same time crossing the boundary from the opposite side. This arrangement eliminates some of the problems caused by small surface to volume ratio but the simulation box should be kept large enough to avoid any self-interaction at boundary crossing so that a meaningful simulation of equilibrium thermodynamic properties can be evaluated.

3.6.5 Temperature Control

Molecular dynamics simulation can be run with different ensembles depending on the simulation problem. The commonly used ensembles are micro-canonical (NVE), grand canonical (μVT), canonical (NVT) and isothermal-isobaric (NPT). The symbols N, P, E, T and μ respectively stand for number of atoms, pressure, energy, temperature and chemical potential. In order to control temperature, various types of thermostats have been proposed. Among them Berendsen (70), Lengevin (71) and Nose-Hoover (72; 73) are widely used. In this dissertation work Nose-Hoover thermostat is used.

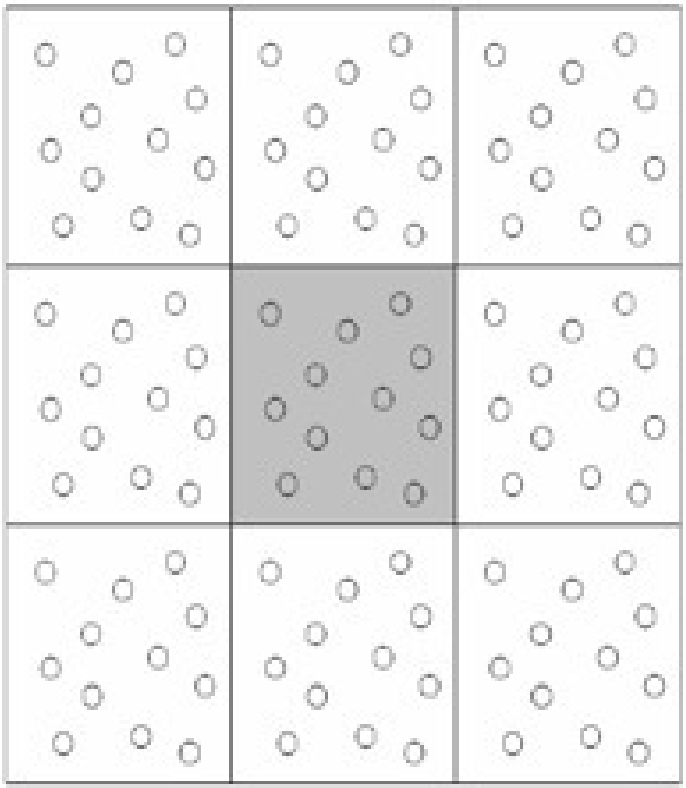

Figure 3.2: Schematic picture showing PBC in 2D.

3.7 MD Simulation of Displacement Cascade

Molecular-dynamics (MD) simulations are now routinely used to study the radiation damage process. For studying radiation damage using MD simulation it is usual practice to use many-body potentials. Daw and Baskes (74; 75) and Finnis and Sinclair (76) introduced the use of many body potentials in 1980s to study complex systems like metals. To describe metals and alloys the embedded-atom method, EAM, is generally used (77). In embedded-atom methods, the energy is expresses as

$$E_{Total} = \sum_{i=1}^{N} E_i = \sum_{i=1}^{N} \left[\frac{1}{2} \sum_{j \neq i}^{N} V(r_{ij}) + F_i(\rho_i) \right] \tag{3.50}$$

Here, $V_{ij}(r_{ij})$ is a short-range potential which gives the contribution to the energy coming from the repulsion between the cores of the atom, F_i represents an embedding energy function of an atom in the solid, $\rho_i = \sum_{i \neq j}^{N} \rho(r_{ij})$ represents the electron density at the location of atom i, and r_{ij} is the distance between the atom i and j. The functions V and F are usually determined empirically from known properties of the solids.

MD simulation has been used as a primary tool to study the displacement cascade evolution and point defect behavior in iron (78; 79; 80; 81; 82; 83; 84; 85) using embedded-atom type interatomic potentials developed by Finnis and Sinclair (83) and a modified version by Calder and Bacon (80). Variable time steps are generally used in the simulation to maintain numerical accuracy in the integration with initial time steps in the range from $\sim$1 to 10×10^{-18} s and later in the range $\sim$1 to 10×10^{-15} s . MD cascade simulations are usually run for 10-100 ps.

3.8 First Principle Calculations of MD Simulated Data

To get information on effect of radiation damage on magnetic structures in irradiated sample of bulk iron ab-initio calculation using Locally Self-Consistent Multiple Scattering (LSMS) has been used to process the time-framed data obtained from the MD simulations (86; 87)

Chapter 4

Dynamic Pair-Density Function of Liquid Iron

4.1 Introduction

A Crystalline solid possesses a periodic assembly of atoms or ions and the atomic dynamics is vibrational in nature. They are characterized by normal modes which are plane waves because the interatomic forces are harmonic for small displacements. Hence, a well-defined relationship between the frequency and wavelength of the density fluctuations called phonon exists in crystalline solids. Therefore, in crystals we observe sharp peaks in the energy spectrum for a given momentum. The line-width of these peaks in the energy spectrum of the crystals is related to the phonon lifetime and is due to lattice defects or the presence of anharmonicity. The phonon description is not very successful to describe the dynamics in liquids because in addition to anharmonicity strong structural disorder plays a significant role to make the situation more complicated. Molecular dynamic simulation is a powerful tool to study the atomic dynamics in liquids because one can investigate single-particle and the collective dynamics easily, although the finite size of the box is a technical restriction. Generally, the collective dynamics in liquids is described by the coherent

dynamic structure factor, $S(Q, \omega)$. But, recently it has been shown that its Fourier transform called Dynamic Pair-density function (DPDF), $\rho(r, E)$, is a more useful quantity in the study of the disordered systems like liquids and glasses (11). In this chapter the result of the DPDF of the liquid iron at high temperature interacting with a pair-potential is discussed.

4.2 Molecular Dynamics Simulation

Classical Molecular-dynamics (MD) simulations were performed for a single component system of particles with the mass of iron. The simulations were done for liquid and glassy phases of iron. The modified Johnson (mJp) pair wise potential was used for the particle interaction (88; 89; 90). The details of the potential is discussed by Levashov et. al. (90) and it is as shown in Figure 4.1 . The simulation was performed on a system consisting of 5488 particles. The time step was chosen to be 10^{-15} s (femto second). An in-house MD code was used with a modification to include the modified Johnson pair-wise potential in the canonical ensemble (specific N, V and T). Periodic boundary conditions were applied and a fifth-order Gear Predictor-Corrector method was used to integrate the equations of motion (69; 67).

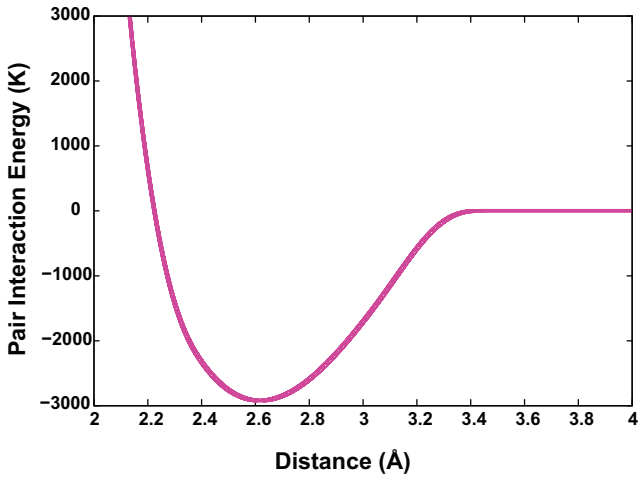

Figure 4.1: Modified Johnson's potential.

The simulation was done for a single density at temperatures of 3000 K, 2500 K, 2000 K, 1500 K and 300 K. The temperature of the system was controlled using Nose-Hoover Thermostat (72). In the MD simulation 10^5 steps of equilibration and 10^5 steps of production were used.

4.3 Results

4.3.1 Pair-Density Function (PDF)

The pair-density function, or partial pair-density function in the case of multiple component systems, can be obtained from experiment by Fourier transforming the static scattering factor, $S(q)$. The limited range of momentum transfer in the elastic scattering experiments always results in in the PDF errors at small r in the experimentally determined PDF. Conversely, simulations are of limited size, resulting in errors at large r due to periodic boundary conditions. As implied by the name they give the ratio of the number of pairs in a spherical shell to the number in the same shell for completely random homogeneous placement of atoms. Integrals over the peaks give the coordination numbers.

Figure 4.2 shows the pair-density function for the liquid phase of iron at 3000 K, 2500 K, 2000 K and 1500 K and also for glassy phase at 300 K. It is clearly seen that there is no basic difference in correlation function except that the peaks in glassy phase are sharper as compared to the liquid phase thereby showing no fundamental structural difference between the two phases. The first peak in the glass is narrower and at smaller separation than in the liquid in a manner that is consistent with thermal contraction under cooling and reduced thermal vibration. The splitting of the second peak is a characteristic feature of glasses and it results from the steric effects of local packing. There are higher order structural correlations, for example the probability of particular triangular geometries that are not visible in the PDF (although completely determined by the PDF for pair-wise interactions).

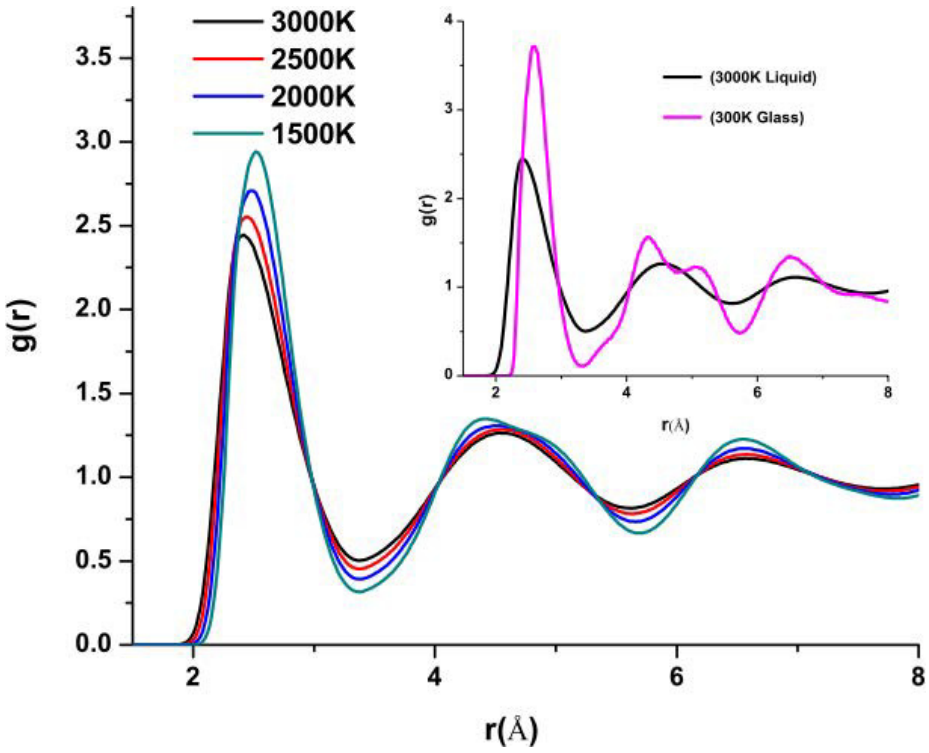

Figure 4.2: Pair density function of liquid and glassy phase iron.

4.3.2 Static Structure Factor

The static structure factor, $S(q)$, is the standard result of counting elastic scattering events as a function of the change in momentum, q, of the scattered particle (photon, neutron, or electron). It can be interpreted as the response of the system to a perturbation as a function of the wave vector of the perturbation through the fluctuation-dissipation theorem. For example, at long wavelength $S(q)$ gives the compressibility. The first peak of $S(q)$ is what remains of the smallest reciprocal lattice vectors that determine the Brillouin zone (bisectors of the nearest reciprocal lattice vectors) in the crystal. The pseudo-Brillouin boundary of the glass or liquid can create pseudo-gaps in the electron density of states that have consequences for structural stability and electron transport if the Fermi energy is in the pseudo-gap.

The pair correlation functions for liquid and glassy phase iron were Fourier-transformed to get the static structure factor and the Figure 4.3 below shows the results. Again we see no basic difference among the static structure factors except for the sharpness of the peaks in the glassy phase.

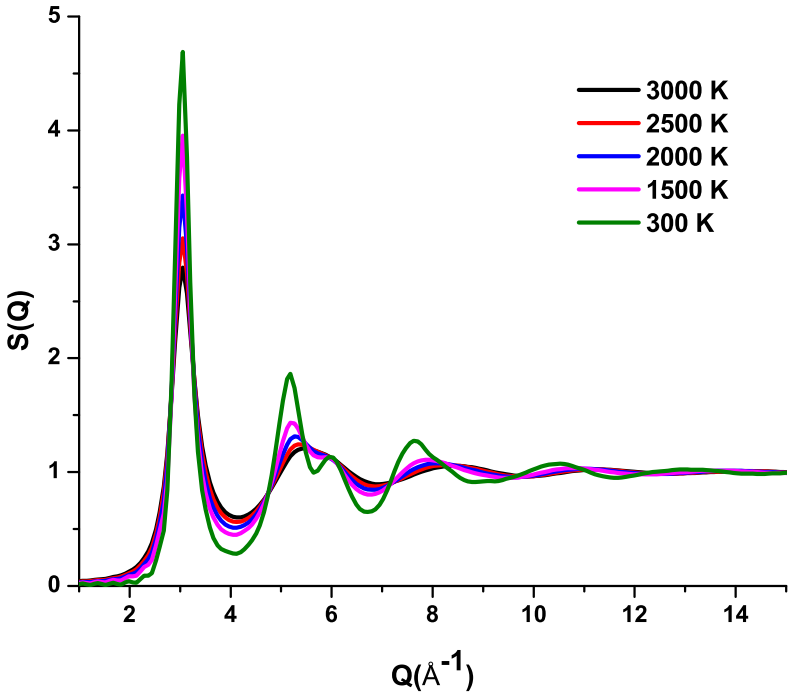

Figure 4.3: Static Structure factor of liquid and glassy iron.

4.3.3 Dynamic Pair-Density Function

From the particle trajectory file one can calculate the self-part of Van-Hove Correlation function $G_s(r,t)$ which gives the probability that a given particle travels a distance r in the time interval t and the distinct-part of Van-Hove Correlation function $G_d(r,t)$ which gives the probability of finding two particles at distance r in time interval t (24). The self and distinct-part of Van-Hove Correlation functions are defined as (24; 91):

$$G_s(\vec{r},t) = \frac{1}{N}\left\langle \sum_i \delta[\vec{r} - |\vec{r}_i(t) - \vec{r}_i(0)|] \right\rangle \tag{4.1}$$

$$G_d(\vec{r},t) = \frac{1}{N}\left\langle \sum_i \sum_{j\neq i} \delta[\vec{r} - |\vec{r}_j(t) - \vec{r}_i(0)|] \right\rangle \tag{4.2}$$

Here, the angular brackets represent he usual time average over a system at equilibrium, and δ is the Dirac delta symbol. N is the number of particles, $\vec{r}$, $\vec{r_i}$ and $\vec{r_j}$ are the particle coordinates and t is the time.

The dynamic pair-density function for collective motion, which gives the density of pair of different atoms i and j separated by distance r and vibrating with frequency ω, is calculated by Fourier transformation of $G_d(r,t)$

$$\rho(\vec{r},E) = \int G_d(\vec{r},t)e^{i\omega t}dt \tag{4.3}$$

The dynamic pair-density function, $\rho(\vec{r},E)$, is defined as (9):

$$\rho(\vec{r},E) = \frac{1}{N\langle b\rangle^2}\sum_i\sum_j b_i b_j \left\langle\left\langle \delta\left[(\vec{r} - (\vec{R}_i(0) - \vec{R}_j(t)))\right]\right\rangle\right\rangle e^{i\omega t}dt \tag{4.4}$$

Here, E and ω respectively energy and angular frequency ($E = \hbar\omega$), N is the number of atoms, $\vec{R}_i$ and $\vec{R}_j$ are particle coordinates and are function of time. δ is Dirac delta function, b_i is the neutron scattering length of i-th atom; $\langle....\rangle$ and $\langle\langle....\rangle\rangle$

are respectively thermal average and ensemble average. The dynamic pair-density function for liquid iron at 3000 K is shown in Figure 4.4.

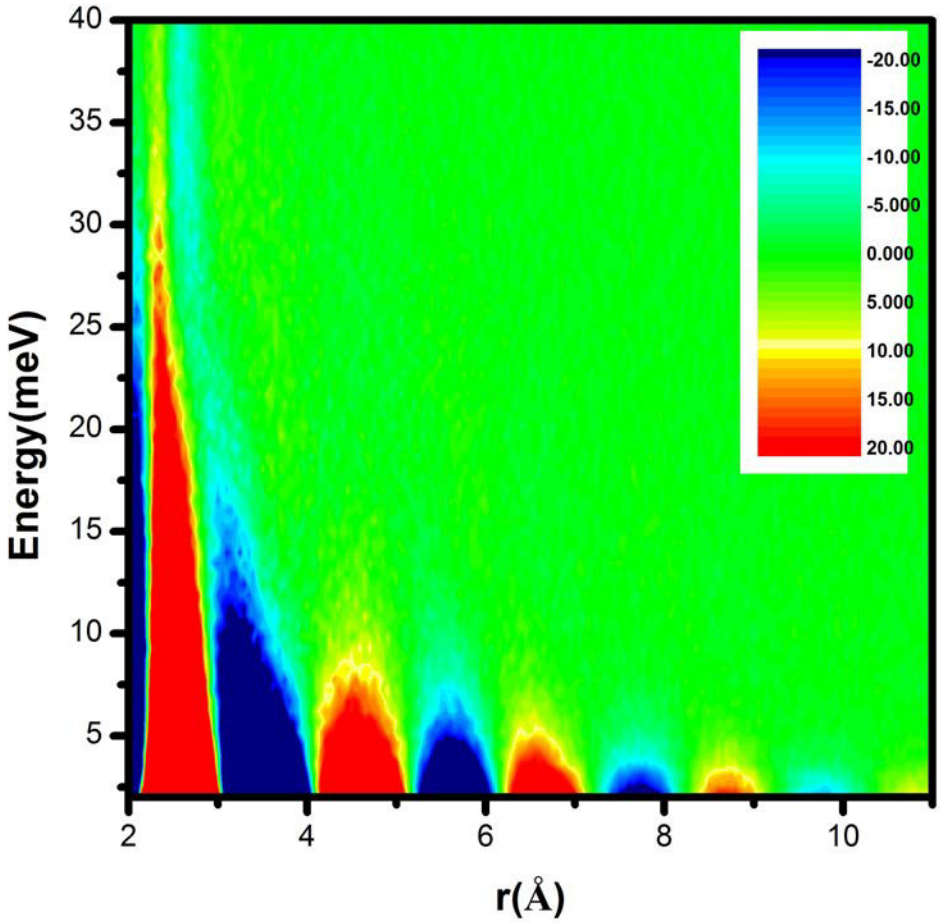

Figure 4.4: Dynamic pair-density function of liquid iron at 3000 K.

4.4 Discussion

The elementary excitations of the lattice in crystalline solids are phonons. Many of their thermal properties can be predicted easily by using phonons as the basis to calculate the partition function. In crystalline solids normal modes are obtained by diagonalizing the dynamical matrix (92). Similar analysis has been made for liquids (93). However, in the case of liquids, the conventional Born-Von Karman approach to phonons does not work, as the dynamical matrix is time-dependent. The long wavelength phonons survive in liquids because for long-wavelength phonons the disorder only affects through the bulk elastic constants, which depends on averages over many atomic sites. Except the long-wavelength phonons other phonons are highly damped, and scattered and short-lived.

Recently it has been shown that the self-energies associated with atomic level stresses satisfy the $\frac{3}{2}k_BT$ law (equipartition theorem) for various pair-wise potentials including Lennard Jones, modified Johnson and repulsive part of Johnson potentials at high temperatures at various particle densities (90; 94). This observation suggests that the fluctuations of the atomic level stresses could be used as normal modes for high temperature liquids. It is seen from Figure 4.4 that the dynamic pair-density function in liquid iron at high temperature is limited to the nearest neighbors at energies more than 10 meV (=2.5 THz). This shows that most of the atomic dynamics depends primarily to the nearest neighbors. In other words most of atomic dynamics in the high temperature liquid iron is super-localized to the nearest neighbors. Therefore, the dynamics of the atomic level stresses, which depends primarily on the nearest neighbors, provides a good description of the atomic dynamics in liquid at high temperatures.

Chapter 5

Crystalline and Amorphous Models of Highly Damaged Fe

A similar version of this chapter appeared as "*Crystalline and Amorphous Models of Highly Damaged Fe*" Madhusudan Ojha, D. M. Nicholson, Bala. Radhakrishnan, R. E. Stoller and Takeshi Egami (2011), MRS Proceedings, 1363 , mrss11-1363-rr05-32 doi:10.1557/opl.2011.1364

5.1 Introduction

In modern nuclear reactors, including fusion reactors, nuclear materials have to withstand very high levels of radiation damage, and understanding the mechanism of irradiation damage is an important subject. Materials damaged by high-energy particles are locally so strongly disordered to the level akin to amorphous or glassy material. Therefore our approach on liquids and glasses may be of use for description of materials highly damaged by irradiation. A useful basis for understanding the structural integrity of irradiated materials should begin with the simulation of individual radiation cascades. This is the level at which the ameliorating influence of composition or processing modifications can be identified. The success of advanced

designs for fission and fusion reactors may well depend on advanced materials that improve mechanical performance under irradiation (95).

In this chapter we describe the application of novel structural characterization tools to a sequence of configurations that follow the evolution with time of a 54000 atom sample of alpha Fe after one atom (the primary knock-on atom, PKA) is given a velocity in the (1,1,3) direction corresponding to an impulse delivered by a 1 KeV neutron. The sample is initially in equilibrium at a temperature of 100K, periodic boundary conditions are in effect, the pressure is maintained at zero, and the atoms move according to embedded atom forces integrated with variable time steps to account for initial high atomic velocities (96). Specifically, the MOLDY (84) Molecular Dynamics, MD, code was used with the force fields developed by Finnis and Sinclair (76; 83) as modified by Calder and Bacon (80). Yang Wang et al. recently reported first principles calculation of the magnetic structure of similarly constructed 9,826-atom cascade samples (86; 87).

We are not attempting to unravel a structure from, for example, scattering experiments. There are no experiments that probe the local atomic structure at the initiation of a cascade. The structures that we analyze may or may not be representative of actual cascades; the physical accuracy of the structures depends on the fidelity of the model ionic forces to the many-body electronic forces that they represent. The structures are, however, completely specified; our objective is to provide interpretive tools that describe the structure in alternative ways that will be useful in explaining electronic, magnetic, thermodynamic, and elastic properties.

5.2 Computational Approach

For homogeneous systems in equilibrium at temperature, T, interacting through central-pair-wise forces, the free energy is fully described by the pair distribution function (97), PDF or $g(r)$. Because the pair interaction is usually dominant, the PDF is a logical starting-point for structural description even for an inhomogeneous

system interacting with any body interactions. The PDF is calculated by summing over all pairs of atoms and counting the number of pairs that are separated by a distance, r, to within a small tolerance, Δr. To adapt the PDF for the inhomogeneous case one of the two atoms in a pair was restricted to be within a specified distance, R, from the center of the cascade:

$$g(r) = \left\langle \frac{1}{N_{r_i<R}} \sum_{i,r_i<R}^{N_{r_i<R}} \sum_{j=1}^{N} \delta\left(r - |\vec{r}_i - \vec{r}_j|\right) \right\rangle \tag{5.1}$$

An average over a short time interval is indicated by the angle brackets. The, PDF describes the instantaneous average local environment of atoms within the sphere, R. At large r it resembles the PDF of a perfect crystal because the sample is undisturbed far from the cascade. At small r the distribution of separations is large because of the high temperature and large number of defects.

Because the peaks in the PDF at short distance have widths similar to those of the liquid we were motivated to perform a comparative analysis of the atom mobility in terms of the mean squared displacement, MSD, of atoms that are in the vicinity of the cascade.

$$MSD\left(t, \Delta t\right) = \left\langle \frac{1}{N_{r_i<R}} \sum_{i,r_i<R}^{N_{r_i<R}} \left|r_i\left(t + \Delta t\right) - r_i(t)\right|^2 \right\rangle \tag{5.2}$$

Here the angle brackets would optimally represent an ensemble average, however, we follow the usual pragmatic procedure of averaging over times in a range around, t. The MSD describes the mobility of atoms; mobility is typically larger in liquids than in crystals. Recall that at large Δt the slope of the MSD curve is proportional to the diffusivity and that at small Δt the curvature is proportional to the average velocity squared that in turn is proportional to an effective local temperature, T_R.

$$T_R(t) = \frac{m}{3k_B N_{r_i<R}} \sum_{i,r_i<R}^{N_{r_i<R}} \left|\dot{\vec{r}}(t)\right|^2 \tag{5.3}$$

5.3 Results and Discussion

In Figure 5.1a the PDF calculated with $R = 1\ nm$ at an early time (0.78 ps after cascade initiation) is compared to the PDF at the peak of the cascade induced vacancy count. At the early time the PDF is roughly that of a perfect crystal at 100K. There are a few anomalous atomic environments surrounding the PKA that contribute, particularly at small r. At the height of the cascade the first and second nearest neighbor peaks of the crystal broaden to form a single peak with a shoulder and a split second peak replaces the third, fourth, and fifth peaks of the crystal. Comparison to the PDF of the bulk super-cooled liquid displayed in Figure 5.1b shows similar peak widths and coalescence of the crystalline neighbor shells.

The sixth neighbor shell peak is absent in both. The second peak is split in the cascade with the larger component of the peak being at larger r corresponding to the 24 fourth nearest neighbors in the bcc structure. In the liquid the second peak is not split at high temperature but begins to split at low temperature. The relative heights of the two components of the second peak are reversed relative to the cascade structure. This reversal of the weight of the two sub-peaks clearly distinguishes the structure from that of a liquid.

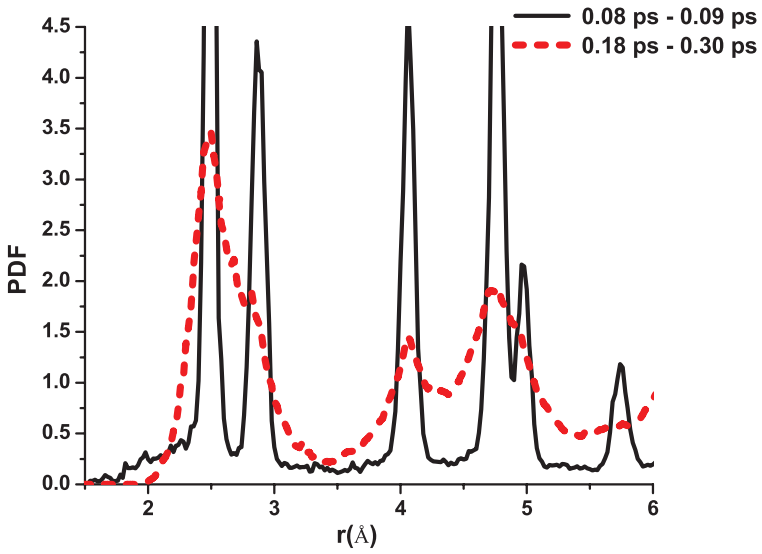

(a)

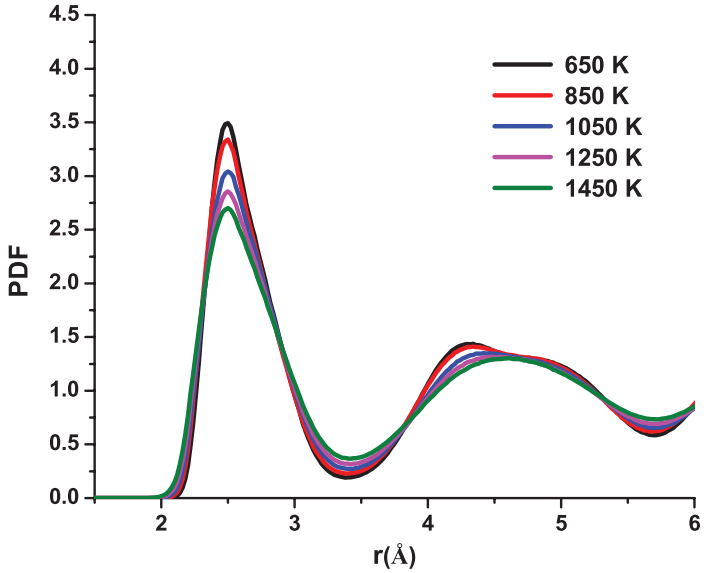

(b)

Figure 5.1: (a) The PDF shortly after cascade initiation (dashed) and at the peak of vacancy count (solid). (b) The PDF of super-cooled liquid Fe at several temperatures.

Figure 5.2a shows the number of vacancies within spheres of various radii as a function of time. The average temperature within spheres of various radii as a function of time is shown in Figure 5.2b.

Although, we know that the structure within the cascade is not a super-cooled liquid because it maintains average bond orientations aligned with the bcc lattice; we

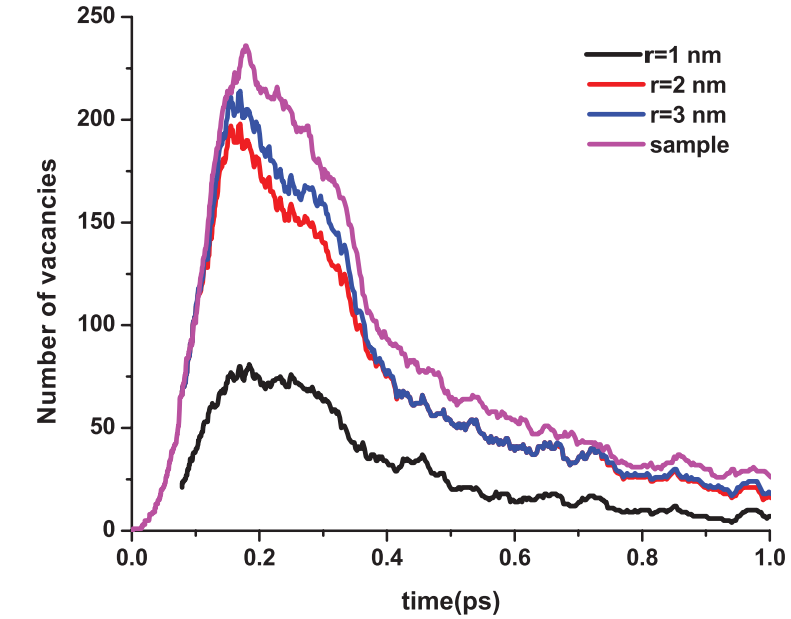

(a)

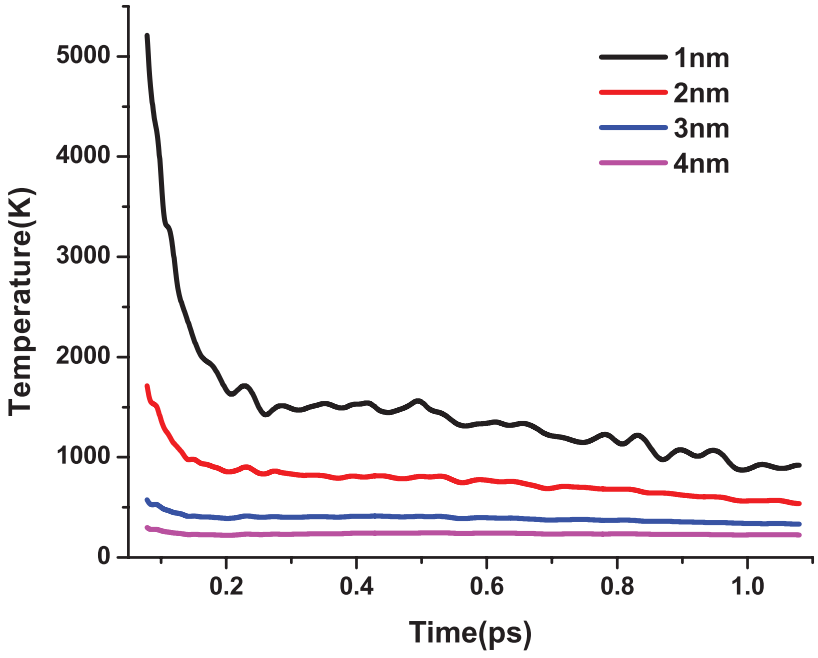

(b)

Figure 5.2: (a) The number of vacancies within spheres of various radii as a function of time. (b) The average temperature within spheres of various radii as a function of time.

explore the relevance of a liquid-like description by calculating the MSD for spheres of different radius measured from the center of the cascade.

The length of time used for the time averaging is 1 ps. Over this time period the PDF remain sufficiently unchanged that we may consider the MSD to correspond to the average MSD over the life of the cascade. As the radius is increased the contribution from the portion of the crystal that is undisturbed by the cascade increases and correspondingly the MSD decreases. This decrease is expected because the undisturbed crystal that is enclosed in the larger spheres has a lower density of vacancies and a lower average temperature.

The number of vacancies and the average temperature for each sphere size is shown as a function of time over the lifetime of the cascade in Figures 5.2a and Figure 5.2b.

The MSD of the cascade (R=1 nm) is very similar to that of liquid iron (Figure 5.3b) in the appropriate temperature range. The average temperature is reflected in the curvature at small Δt thus the cascade effective temperature is about 1350K; this is consistent with the temperature as a function of time in Figure 5.2b.

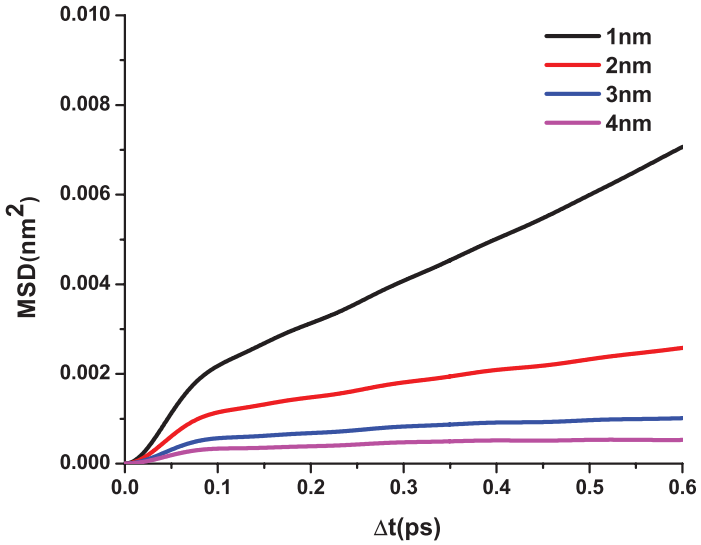

(a)

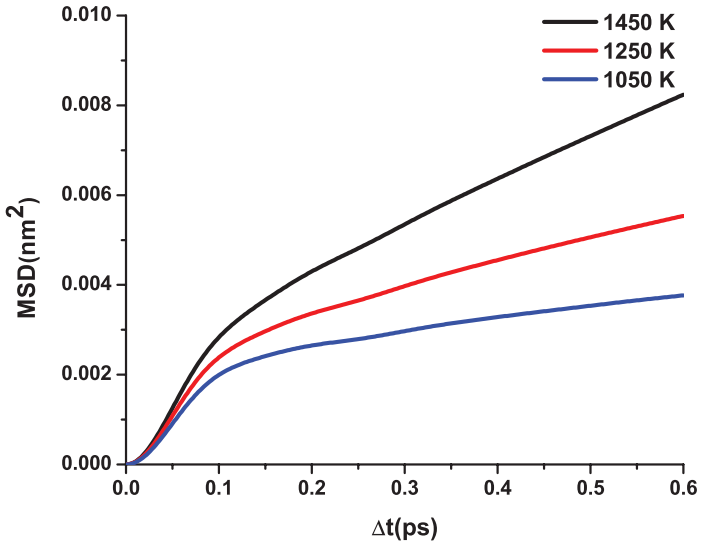

(b)

Figure 5.3: (a) MSD over spheres of various radii over the cascade life as a function of time difference. (b) MSD of liquid Fe at various temperatures as a function of time difference.

Diffusion can often be related to atomic volume or free volume; Figure 5.4a and 5.4b compares the volume distribution within the cascade at initiation to the distribution at the time of the crest of the cascade. The volumes are those of the Voronoi polyhedrons surrounding each atom (98). Figure 5.4c shows a distribution for liquid Fe at 1250K that is very similar to that if the cascade at its crest.

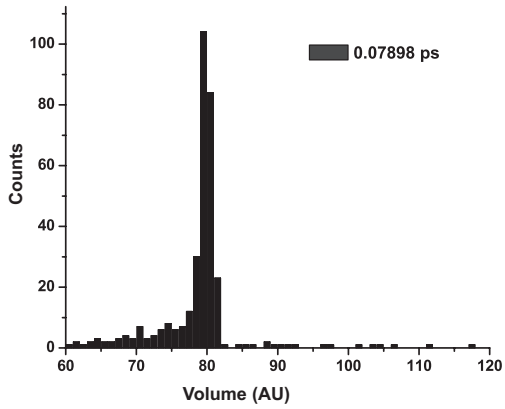

(a)

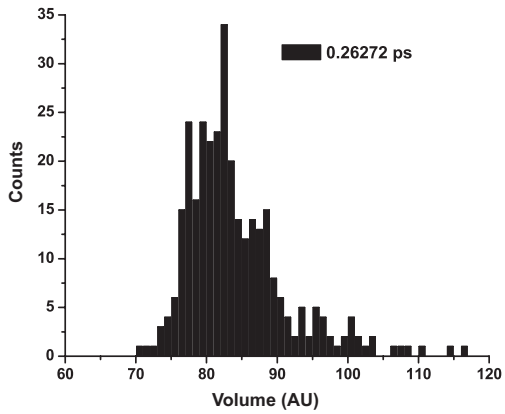

(b)

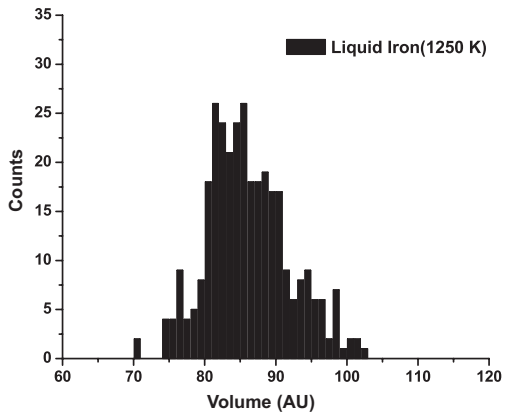

(c)

Figure 5.4: (a) Distribution of atomic volumes within 1 nm radius shortly after cascade initiation. (b) Distribution of atomic volumes within 1 nm radius at peak of vacancy count. (c) Distribution of atomic volumes within 1 nm radius sphere of super-cooled liquid Fe at 1250K.

The distribution for the liquid was calculated for a sphere of radius 1 nm cut from a single configuration of the liquid so that it would be directly comparable to the result for the 1 nm sphere centered on the cascade. Similar statistical noise is also evident in the appearance of the distributions. The distribution of free volume (not shown) is very different between the cascade containing crystal and the liquid because the large vacancy volume dominates the crystal distribution.The MSD may be more closely related to the volume distribution than to the free volume distribution.

5.4 Conclusion

Central pair-wise forces give reasonable thermodynamics and structures for metals. It is therefore reasonable to describe the metallic structure in terms of the PDF. For example the potential energy (for central-pair-wise forces) is simply an integral of the product of the pair potential and the PDF. Here we adapt the PDF to an inhomogeneous, non-equilibrium system and observe some commonality of behavior between the radiation damaged sample and the super-cooled liquid. This does not lead us to say that the heart of the cascade is a liquid but simply to say that analysis in terms of the PDF and MSD that is typically used in liquids can be useful for describing the locally the radiation damage. Continued use of these tools is expected to contribute to the discovery of correlations between properties and structure in radiation-damaged materials.

Chapter 6

First principle local stress

This chapter is a draft of a paper "*First principle local stress*" D. M. Nicholson, M. Ojha and T. Egami to be submitted to Phy. Rev. B.

6.1 Introduction

The past two decades have seen rapid growth in the use of Density Functional Theory (DFT) (14; 99; 100; 101; 49; 15) to explain the behavior of materials. This growth is attributable to the general accuracy of the method, especially with respect to trends in energy as function of the positions of the nuclei. The availability of the dependence of the energy on nuclear positions implies that the forces can be calculated, and this leads naturally to DFT based molecular dynamics. Other useful quantities can also be obtained, for example the lowest occupied one-electron energy levels of the Kohn-Sham potential (band structure) that are needed to evaluate the electron density. The density of the occupied and unoccupied levels (DOS) can be calculated and it is natural to associate partial occupation of the higher bands with excited states. When trying to unravel the behavior of a material it is common to perform many calculations as a function of nuclear positions, i.e. different volumes, structures, defects, chemical order and for each to investigate auxiliary quantities such as the DOS, elastic constants, Fermi surfaces, atomic charge, band structure,

phonon dispersion, local magnetic moments, covalent bond charge, etc. On the basis of trends within a subset of these quantities an interpretation is made often evoking the behavior of simpler models such as tight binding or chemical concepts such as the formation of covalent bonds. Especially for crystalline systems this procedure has been very productive and the number of calculated quantities upon which to base explanations has expanded impressively, leading to improved understanding of materials phenomenon. However for disordered structures less progress has been made, even though many of the same capabilities are available simply by using large supercells or with methods that directly calculate ensemble averaged properties, most notably the Coherent Potential Approximation (CPA) for random alloys (102). We propose the atomic level stress as a new tool for understanding the behavior of disordered materials.

The macroscopic elastic responses, elastic constants, are often calculated directly from the variation of the energy with respect to deformation of the supercell or from the scaling equations introduced by Nielsen and Martin (64; 16). However, the connection at the atomic level between stress, strain, and continuum elasticity is less utilized. An atomic level interpretation of stress makes it possible to develop an intuitive understanding of behavior based on concepts from continuum mechanics (12). Such a treatment may be especially useful for understanding behavior of disordered materials where the description in terms of phonons breaks down for all but long wavelengths. Several studies point to the value of using the local stress to characterize liquids and glasses (90; 103).

The formulation by Nielsen and Martin gives the stress field on electrons and nuclei, which can be integrated over the atomic volume to yield the atomic level stresses (104; 105). In this paper, however, we chose to define the atomic level stresses in a different way, the electron density relaxes to the ground state for the displaced atomic positions as in the frozen-phonon method and the Born-Oppenheimer approximation. Only the nuclei are deformed in the affine manner, whereas the electronic degrees of freedom are relaxed. Then the atomic level

stresses are defined as the change in the local electronic energy of each atom due to deformation. Of course, the decomposition of the total energy into the local energies is far from unique. For example, different choices of volume associated with an atom affect its value of atomic level stress. Furthermore, gauge transformations give terms with vanishing integrals over the unit cell but that do not necessarily vanish for integrals over each atomic volume. For example the Bader (106) choice is a volume defined by the surface where the electron density gradient is zero. Trinkle et al (107; 108) selects different volumes for the kinetic and Coulomb contributions; for the Coulomb term they make the Bader choice while the kinetic volume is based on a vanishing of the gradient of the Kohn-Sham potential.

In this paper we discuss various choices for the definition of the local stress and compare the resulting values of stress for several crystalline, liquid, and glassy metals. In the first section we describe several choices for the separation of energy into contributions associated with each atomic site. In the second section we derive the stress from the total energy and discuss the separation of the stress into atomic contributions and explain why this differs from the stress obtained from the derivative of the local energy. The third section gives details of calculations within the atomic sphere approximation using the Locally Self-consistent Multiple Scattering (LSMS) method (18; 17). Results are presented in the fourth section and conclusions are drawn in the fifth section.

6.2 Local Energy

The total energy in Local Density Approximations (LDA) consists of the kinetic energy of a noninteracting electron gas in an effective potential, Kohn-Sham potential, and the classical Coulomb energy of all charged particles. Corrections are made to adjust for correlation in both the kinetic and Coulomb energies. In the following paragraphs we will discuss each of these terms in the total energy.

We express the kinetic energy in term of the DOS because non-interacting electron eigenvalues are very widely used to explain materials behavior. Understanding often hinges on details of the band structure or the density of states, (DOS). The DOS can be further decomposed according to site and angular momentum as local DOS to provide more detailed assessment of phenomena. The difference in the sum of occupied eigenvalues measured from an electrostatically set energy zero is sufficient to give the energy difference between two structures or two magnetic states according to the force theorem also known as the frozen potential approximation. The difference in self-consistent eigenvalue sums of two structures with energies measured from the Fermi level is also often sufficient to explain structural energy differences. To maintain contact with the long-standing use of the DOS as an interpretive tool we choose to assign the site kinetic energy according to:

$$T = \sum_i \int^{\epsilon_F} \epsilon n^i(\epsilon) \mathrm{d}\epsilon - \int_{\Omega_i} V_{KS}(\mathbf{r}) \rho(\mathbf{r}) \mathrm{d}\mathbf{r}, \tag{6.1}$$

where $n^i(\epsilon)$ is the local density of states on site i and $V^i_{KS}(\mathbf{r})$ is the Kohn-Sham potential, i. e. the potential for which the Schrödinger equation must be solved in order to obtain an electron density, $\rho(\mathbf{r})$. This form is directly related through the Schröginger equation (Rydberg atomic units) to the asymmetric form of the kinetic energy:

$$T = -\sum_i \int_{\Omega_i} \psi^\dagger \nabla^2 \psi \mathrm{d}\mathbf{r}, \tag{6.2}$$

The symmetric form of the kinetic energy differs from the symmetric form by a surface contribution:

$$T = \sum_i \int \nabla\psi^\dagger \nabla\psi^\dagger \mathrm{d}\mathbf{r} - \int_{s_i} \mathrm{d}\mathbf{n} \cdot \psi^\dagger \nabla\psi, \tag{6.3}$$

Turning to the electrostatic energy, we describe two approaches and how they are related. One way to construct a local electrostatic energy is to follow the standard path to the electromagnetic stress field for the case where there is no magnetic field

present:

$$U = \frac{\epsilon_0}{2} \int \mathrm{d}\mathbf{r} \mathbf{E} \cdot \mathbf{E} \tag{6.4}$$

where $\mathbf{E}$ is the electric field and $\epsilon_0 = \frac{1}{4\pi}$ is the permittivity of free space. Another approach is to follow the classical expression for the atomic level stress by attributing half of the bonding energy between each pair of atoms to each of the atoms.

$$\begin{aligned} U &= \frac{1}{8\pi} e^2 \left[\sum_{i,j} \frac{Z_i Z_j}{|\mathbf{R_i} - \mathbf{R_j}|} \right. \\ &+ \left. \int_{\Omega_i} \mathrm{d}\mathbf{r} \int_{\Omega_j} \mathrm{d}\mathbf{r}' \frac{\rho(\mathbf{r})\rho(\mathbf{r}')}{|\mathbf{r} - \mathbf{r}'|} - 2 \int_{\Omega_i} \mathrm{d}\mathbf{r} \frac{\rho(\mathbf{r}) Z_j)}{|\mathbf{r} - \mathbf{R_j}|} \right] \end{aligned} \tag{6.5}$$

For either starting point the interaction of a nucleus with itself, U_0, should be removed; it has no physical consequences because it is a constant (infinite for point nuclei) and is the same independent of the placements of the nuclei.

$$U_0 = \frac{1}{8\pi} \sum_i \int \mathrm{d}\mathbf{r} \mathbf{E}_{\mathbf{Z_i}} \cdot \mathbf{E}_{\mathbf{Z_i}} \tag{6.6}$$

where,

$$\mathbf{E}_{\mathbf{Z_i}} = \frac{e Z_i (\mathbf{r} - \mathbf{R_i})}{|\mathbf{r} - \mathbf{R_i}|^3}. \tag{6.7}$$

Expressions in terms of the electrostatic field can be transformed into expressions in terms of "bonds" through the the identities:

$$\begin{aligned} \frac{\epsilon_0}{2} \int \mathrm{d}\mathbf{r} \mathbf{E} \cdot \mathbf{E} &= \frac{\epsilon_0}{2} \int \mathrm{d}\mathbf{r} \mathbf{E} \cdot (-\nabla \phi) \\ &= \frac{\epsilon_0}{2} \left[\int \mathrm{d}\mathbf{r} \nabla \cdot \mathbf{E}(-\phi) + \int_S \mathrm{d}\sigma \cdot \mathbf{E}\phi \right] \\ &= \frac{\epsilon_0}{2} \sum_i \left[\int_{\Omega_i} \mathrm{d}\mathbf{r} \frac{\rho_c}{\epsilon_0}(-\phi) + \int_{S_i} \mathrm{d}\sigma \cdot \mathbf{E}\phi \right] \end{aligned} \tag{6.8}$$

where ϕ is the Poisson potential and ρ_c is the charge density. The two expressions differ by the surface contributions in Eq. 6.8. We will adopt the bond energy form Eq. 6.5 because of its close association with the pair potential based local stress, which is an established procedure in the study of structural disorder.

The exchange-correlation energy, E_{xc}, includes corrections to the kinetic and Coulomb energy due to correlation (including exchange). The exact E_{xc} could be separated into site contributions in several different ways; the utility of each could then be debated. However, in the local approximation E_{xc} has a straightforward site decomposition; we will adopt this decomposition,

$$E_{xc} = \sum_i \int_{\Omega_i} \mathrm{d}\mathbf{r}\rho\epsilon_{xc}(\rho). \tag{6.9}$$

In summary we take the local energy to be

$$\begin{aligned} E_i &= \int^{\epsilon_F} \epsilon n^i(\epsilon)\mathrm{d}\epsilon - \int_{\Omega_i} V_{KS}(\mathbf{r})\rho(\mathbf{r})\mathrm{d}\mathbf{r} \\ &- \frac{1}{2}\int_{\Omega_i} \mathrm{d}\mathbf{r}\rho_c\phi \\ &+ \int_{\Omega_i} \mathrm{d}\mathbf{r}\rho\epsilon_{xc}(\rho) \\ &- \frac{1}{8\pi}\int \mathrm{d}\mathbf{r}\mathbf{E}_{\mathbf{Z_i}}\cdot\mathbf{E}_{\mathbf{Z_i}}, \end{aligned} \tag{6.10}$$

where Ω_i is the Voronoi polyhedron. If the electron density transformation is assumed to be affine with an isotropic linear scaling parameter, λ, as the volume in changed from its an initial volume, V_0, the energy is

$$\begin{aligned} E_i &= \lambda^{-2}\left(\int^{\epsilon_F} \epsilon n_0^i(\epsilon)\mathrm{d}\epsilon - \int_{\Omega_i} V_{KS}^0(\mathbf{r})\rho(\mathbf{r})\mathrm{d}\mathbf{r}\right) \\ &- \lambda^{-1}\left(\frac{1}{2}\int_{\Omega_i} \mathrm{d}\mathbf{r}\rho_c^0\phi^0\right) \\ &+ \int_{\Omega_i} \mathrm{d}\mathbf{r}\rho^0\epsilon_{xc}(\rho^0(\lambda\mathbf{r}). \end{aligned} \tag{6.11}$$

6.3 Local Stress

In the method by Nielsen and Martin the macroscopic stress can be evaluated from the first order change in energy when an affine deformation is performed on both the set of nuclear positions and the electron density. In our approach, however, we allow the electronic degree of freedom to relax, by solving the DFT equation for the deformed nuclear positions. In such a case the electron density, $\rho_{\bar{\lambda}}(\mathbf{r})$, is different from the electron density obtained by an affine transformation. The difference between the actual variations of the electron density with deformation results in a contribution to the change in energy,

$$\int \mathrm{d}\mathbf{r}\Delta V(\mathbf{r})\Delta\rho_{\lambda}(\mathbf{r}) = 0, \tag{6.12}$$

where,

$$\Delta\rho_{\lambda}(\mathbf{r}) = \rho_{\lambda}(\mathbf{r}) - det(\lambda)^{-1}\rho(\lambda^{-1}\mathbf{r}), \tag{6.13}$$

and

$$\Delta V(\mathbf{r}) = -V_{KS}(\mathbf{r}) + \frac{\delta U + E_{xc}}{\delta\rho(\mathbf{r})}. \tag{6.14}$$

For ground state density, ρ, the Kohn-Sham approach demands $V_{KS} = \frac{\delta U + E_{xc}}{\delta\rho}$. Therefore, the error in the electron density does not contribute to the total stress or forces; this observation is known as the Hellmann-Feynman theorem (109; 110). Forces and stresses for which this theorem is utilized for their evaluation are often referred to as Hellmann-Feynman forces or stresses. However, the contribution to the

change in local energy associated with the site i is not zero,

$$\begin{aligned}
&\int_{\Omega_i} \mathrm{d}\mathbf{r} \left(\Delta V(\mathbf{r}) - \frac{1}{2} \sum_{j \neq i} \int_{\Omega_j} \mathrm{d}\mathbf{r}' \frac{\rho(\mathbf{r}') - \delta(\mathbf{r}' - \mathbf{R_j}) Z_j}{|\mathbf{r} - \mathbf{r}'|} \right) \Delta\rho_\lambda \\
&+ \int_{\Omega_i} \mathrm{d}\mathbf{r} \left(\frac{1}{2} \sum_{j \neq i} \int_{\Omega_j} \mathrm{d}\mathbf{r}' \frac{\Delta\rho_\lambda}{|\mathbf{r} - \mathbf{r}'|} \right) (\rho(\mathbf{r}') - \delta(\mathbf{r}' - \mathbf{R_i}) Z_i) \\
&= \int_{\Omega_i} \mathrm{d}\mathbf{r} \left(-\frac{1}{2} \sum_{j \neq i} \int_{\Omega_j} \mathrm{d}\mathbf{r}' \frac{\rho(\mathbf{r}') - \delta(\mathbf{r}' - \mathbf{R_j}) Z_j}{|\mathbf{r} - \mathbf{r}'|} \right) \Delta\rho_\lambda \\
&+ \int_{\Omega_i} \mathrm{d}\mathbf{r} \left(\frac{1}{2} \sum_{j \neq i} \int_{\Omega_j} \mathrm{d}\mathbf{r}' \frac{\Delta\rho_\lambda}{|\mathbf{r} - \mathbf{r}'|} \right) (\rho(\mathbf{r}') - \delta(\mathbf{r}' - \mathbf{R_i}) Z_i)
\end{aligned} \tag{6.15}$$

Even though, ΔV is zero there are two terms that remain: 1) the error density, $\Delta\rho$, within volume, Ω_i, interacting with the field from the charge outside Ω_i and 2) the interaction of charge inside Ω_i interacting with the field from the error density outside Ω_i. The stress contribution comes only from derivatives of $\Delta\rho$ because $\Delta\rho$ vanishes when the system is not deformed. Note that these terms are not site diagonal; they are essentially Madelung contributions. They are negligible if the sites are neutral or if the charge on a site does not change with deformation; note that an affine transformation of the electron density does not change integrated amounts of charge on a site. It therefore misses the charge tansfer effect.

Eq. (6.15) specifies the local contribution due to deviations from affine behavior of the electron density. The value of the local stress that would be obtained if the electron density were to have perfect affine behavior can be found from the scaling properties of each of the energy terms : non-interacting Coulomb, exchange-correlation, and non-interacting kinetic.

$$\frac{\partial E_i^{Coulomb}}{\partial \epsilon_{\alpha\beta}} = \frac{e^2}{2}\int_{\Omega_i} \mathrm{d}\mathbf{r} \int \mathrm{d}\mathbf{r}' \rho(\mathbf{r})\rho(\mathbf{r}') \frac{(\mathbf{r}-\mathbf{r}')_\alpha (\mathbf{r}-\mathbf{r}')_\beta}{|\mathbf{r}-\mathbf{r}'|^3} - \frac{e^2}{2}\sum_I \int_{\Omega_i} \mathrm{d}\mathbf{r} \rho(\mathbf{r}) Z_I \frac{(\mathbf{r}-R_I)_\alpha (\mathbf{r}-R_I)_\beta}{|\mathbf{r}-R_I|^3} + \frac{e^2}{2}\sum_{J\neq I} Z_I Z_J \frac{(R_I-R_J)_\alpha (R_I-R_J)_\beta}{|R_I-R_J|^3} \tag{6.16}$$

and

$$\frac{\partial E_{xc}^i}{\partial \epsilon_{\alpha\beta}} = \delta_{\alpha\beta} \int_{\Omega_i} \mathrm{d}\mathbf{r} (\epsilon_{xc}(\rho(\mathbf{r})) - \mu_{xc}(\rho(\mathbf{r}))). \tag{6.17}$$

The kinetic contribution depends on the orbitals. The orbitals have the property that their norm squared sum gives the density and simultaneously minimizes the kinetic energy. If a set of orbitals gives a particular density the set of strained orbitals leads to the strained density but the orbitals may not minimize the kinetic energy as the strain changes. The strained orbitals will be correct to zeroth order which is all that is required to obtain the macroscopic stress. However, the local stress will have an additional contribution because the orbitals that minimize the kinetic energy under a strain differ slightly from the strained orbitals. If this small contribution is ignored we obtain from scaling,

$$\frac{\partial T^i}{\partial \epsilon_{\alpha\beta}} = 2\int_{\Omega_i} \mathrm{d}\mathbf{r} \psi^\dagger(\mathbf{r})(-\nabla_\alpha \nabla_\beta)\psi(\mathbf{r}). \tag{6.18}$$

In a plane wave basis the basis-functions are eigenstates of the gradient operator with eigenvalue $i\mathbf{k}$. If the integral in Eq. (6.18) extends over the entire volume, as it does for evaluating the macroscopic stress, the orthogonality of the basis results in a simple expression for the kinetic contribution to stress that is a sum over the orbital coefficients weighted by $k_\alpha k_\beta$. There is additional simplification if the stress

is isotropic, i.e. hydrostatic pressure. In this case we only require,

$$\sum_{\alpha} \frac{\partial T^i}{\partial \epsilon_{\alpha\alpha}} = 2 \int_{\Omega_i} \mathrm{d}\mathbf{r} \psi^\dagger(\mathbf{r})(-\nabla^2)\psi(\mathbf{r}). \tag{6.19}$$

We observe that an isotropic scaling of the density such as that which governs the hydrostatic pressure obeys

$$\sum_{\alpha} \frac{\partial T^i}{\partial \epsilon_{\alpha\alpha}} = 2T^i. \tag{6.20}$$

Scaling relations can simplify calculation of the macroscopic stress; scaling also simplifies the calculation of the local hydrostatic pressure but in this role it is an approximation to the derivative of the local energy with respect to volume because the actual density does not scale with the volume. Scaling relations do not, in general, provide a simple approach to local stress (non-hydrostatic), therefore, we calculate the local stress by calculating the local energy for finite deformations and then approximate the stress from the numerical derivatives of the local energy. Another advantage of using numerical differentiation to obtain the stress is that the stress can be further decomposed into contributions of different origin, for example, kinetic, electrostatic, or exchange-correlation. The use of scaling to separately evaluate these contributions is flawed because the scaling assumption is a poor approximation and it is only through the cancelations between these terms that a valid total stress is achieved.

Although scaling in far from accurate it provides a rough guide for the behavior of various contributions to the atomic level pressure. For a simple x-alpha exchange model, scaling gives a pressure:

$$3P^i\Omega_i = 2T^i + U^i + E^i_{xc}. \tag{6.21}$$

From this we see that the kinetic energy contribution to the pressure is positive (the sum over all sites is positive definite) while both the electrostatic and exchange-correlation terms are generally negative. The electrostatic term can be further

separated into contributions local to site i and those, which arise from the Madelung interactions with the charges on other sites. The Madelung energy is what stabilizes ionic crystals; it is negative under most conditions because the charges arrange themselves in a way that alternates sign in order to minimize the Madelung energy. The on-site electrostatic energy is that of the electron density sitting in a repulsive potential from half the electron density interacting combined with the attractive potential from the protons of the nucleus. The attractive potential from the protons can be expected to dominate because the full proton charge contributes whereas only half the electron charge contributes to this potential and because the protons are point charges which are not diminished near the center of the Wigner-Seitz Cell. There is an important counter example, the vacant site, for which the local electrostatic pressure is always positive.

Another commonly used subdivision of the energy is between band-energy and "double counting terms." This form has the advantage that the explicit interaction between electrons and nuclei is removed and the contribution of the electron-electron and exchange-correlation terms are reduced in magnitude. This form places the band-energy at the fore.

$$E_i = \sum_{\epsilon_k < \epsilon_F} \epsilon_k^{(V(\mathbf{r}))} \int_{\Omega_i} \mathrm{d}\mathbf{r} |\psi_k(\mathbf{r})|^2 - \frac{1}{2} U_{ee}^i + \frac{1}{2} U_{ZZ}^i + \int_{\Omega_i} \mathrm{d}\mathbf{r} \rho(\epsilon_{xc} - \mu_{xc}) \tag{6.22}$$

where either $V(\mathbf{r}) = V_{out}(\mathbf{r}) \equiv \frac{\delta U + E_{xc}}{\delta \rho(\mathbf{r})}$ for the variational Harris functional energy (111) or $V(r) = V_{KS}(\mathbf{r})$ for a non variational expression for the Kohn-Sham ground state energy. The two different potentials have different scaling behavior. When ρ is scaled $\rho \to \lambda^{-3}\rho(\frac{\mathbf{r}}{\lambda})$ the potential referred to as V_{out} has a somewhat complicated behavior. The part that arises from electrostatics scales like the Coulomb energy, the remaining exchange potential has a scaling behavior that cannot be easily simplified.

$$V_{out}(\mathbf{r}) \to \lambda^{-1}(V_{out}(\frac{\mathbf{r}}{\lambda}) - \mu_{xc}(\frac{\mathbf{r}}{\lambda})) + \mu_{xc}(\lambda^{-3}\rho(\frac{\mathbf{r}}{\lambda})) \tag{6.23}$$

When ρ is scaled $\rho \rightarrow \lambda^{-3}\rho(\frac{\mathbf{r}}{\lambda})$ the V_{KS} scales like the kinetic energy, becoming $\lambda^{-2}V_{KS}(\frac{\mathbf{r}}{\lambda})$, as can be seen by considering the Schrödinger equation

$$\left(-\nabla^2_{\mathbf{r}} + \frac{V_{KS}(\frac{\mathbf{r}}{\lambda}) - \epsilon}{\lambda^2}\right)\psi(\frac{\mathbf{r}}{\lambda})\lambda^{-\frac{3}{2}} = 0 \tag{6.24}$$

The proton-proton interaction, U_{ZZ}, always adds to the pressure. The electon-electron term always subtracts from the pressure because it enters with a negative sign. The exchange energy favors a build up of electrons near the nucleus, but because μ_{xc} is larger thad ϵ exchange-correlation adds to the pressure. The band-energy can add or subtract from the pressure depending roughly on whether the system the valence band is more or less than half full.

Because the two potentials, V_{out} and V_{KS} are equal at self consistency they can be substituted for each other in expressions for the ground state energy. However, the resulting expressions will have different scaling behaviors leading to different values for component stresses. When the replacement leads to a non-variational expression for the energy then the macroscopic stress obtained from scaling will be incorrect.

For these reasons we advocate numerical differentiation for determination of local stress and the various terms that contribute to it . Because the macroscopic or average stress is already established by standard procedures, we are mainly interested in the variations in stress from one atomic environment to another. For pair potential models the expression for the local stress at site i, σ^i, is (12)

$$\Omega_i\sigma^i_{\alpha\beta} = \sum_j \mathbf{r}^{ij}_\alpha \mathbf{F}^{ij}_\beta \tag{6.25}$$

where $\mathbf{r}_{ij} = \mathbf{r}_i - \mathbf{r}_j$ and $\mathbf{F}_{ij}$ is the force on site i exerted by neighboring site j that are within the range of the pair potential. The average stress on species A in an A-B alloy is,

$$\sigma^A_{\alpha\beta} = \frac{\sum_{i\epsilon A}\left(\sum_{j\epsilon A}\mathbf{r}^{ij}_\alpha\mathbf{F}^{AAij}_\beta + \sum_{j\epsilon B}\mathbf{r}^{ij}_\alpha\mathbf{F}^{ABij}_\beta\right)}{\Omega^A} \tag{6.26}$$

where

$$\Omega^A = \sum_{i \epsilon A} \Omega_i. \tag{6.27}$$

The symmetry, $F_{ij}^{AB} = -F_{ij}^{BA}$ results in the cancelation of cross terms in the difference between the stress of the two species, A and B.

$$\sigma_{\alpha\beta}^A \Omega^A - \sigma_{\alpha\beta}^B \Omega^B = \sum_{i,j \epsilon A} \mathbf{r}_\alpha^{ij} \mathbf{F}_\beta^{AAij} - \sum_{i,j \epsilon Bj} \mathbf{r}_\alpha^{ij} \mathbf{F}_\beta^{BBij} \tag{6.28}$$

The species average pressure

$$P^A = -\frac{1}{3} Tr(\sigma^A) \tag{6.29}$$

has a difference of

$$3P^A \Omega^A - 3P^B \Omega^B = \frac{1}{2} \sum_{i,j \epsilon A} r^{ij} \frac{\mathrm{d}V^{AA}}{\mathrm{d}r^{ij}} - \frac{1}{2} \sum_{i,j \epsilon B} r^{ij} \frac{\mathrm{d}V^{BB}}{\mathrm{d}r^{ij}}. \tag{6.30}$$

This difference can be rexpressed in terms of partial pair distribution functions, $g^{\alpha\beta}$

$$= \frac{\Omega^A}{2} n c_A \int \mathrm{d}\mathbf{r} g^{AA}(\mathbf{r}) r \frac{\mathrm{d}V^{AA}}{\mathrm{d}r} - \frac{\Omega^B}{2} n c_B \int \mathrm{d}\mathbf{r} g^{BB}(\mathbf{r}) r \frac{\mathrm{d}V^{BB}}{\mathrm{d}r}. \tag{6.31}$$

This form is particularly convenient for liquids or glasses but is also valid for crystals. This expression shows that the criterion that specifies which atoms are under positive pressure and those which are not, is determined by the interactions with like atoms in the cage of surrounding atoms. The local pressure goes beyond atomic size as a probe of the local atomic environment, it incorporates the influence of bonding.

6.4 Calculation Details

The calculations of local stress were performed in the Atomic Sphere Approximation (ASA) using the Locally Self-consistent Multiple Scattering (LSMS) method. The

exchange-correlation energy was treated in the local approximation using the functional of Von Barth and Hedin (112). The LSMS sums the multiple scatter contributions within a zone, the local interaction zone (LIZ) around each site to obtain the electron density on that site. Although the results presented in this paper are for systems containing 100 or fewer atoms we anticipate future calculation of atomic level stress in large disordered systems. The LSMS method is well suited to large models because it assigns a processor to each site; the calculations take the same amount of wall clock time independent of the system size. Once the electron density (including core electrons) within the ASA sphere of each site is determined the Poisson equation for the entire periodically reproduced structure is solved to obtain the Hartree potential. The exchange-correlation potential is added to the electrostatic potential and the self-consistency cycle continues with a subsequent solution of the multiple scattering equations (solution of the Schrödinger equation) until convergence in the electron density is reached. In the unstrained (zero pressure) structure the LIZ is taken to be a sphere of radius 11.5 a.u. (81 atoms). Angular momentum through $l = 3$ were used.

The local energy as specified in Eq. (6.10) was calculated as a function of strain. In the ASA the local energy is

$$\begin{aligned} E_i &= \int^{\epsilon_F} \mathrm{d}\epsilon\ \epsilon n^i(\epsilon) - 4\pi \int^{r^i_{WS}} \mathrm{d}r\ r^2 \rho(r) V_{KS}(r) \\ &+ e^2(4\pi)^2 \int^{r^i_{WS}} \mathrm{d}r\ r^2 \rho(r) \int^{r^i_{WS}} \mathrm{d}r'\ r'^2 \rho(r') \\ &+ \frac{1}{2}\Delta q_i \sum_{j \neq i} M_{ij} \Delta q_j \\ &+ 4\pi \int^{r^i_{WS}} \mathrm{d}r\ r^2 \rho(r) \epsilon_{xc}(\rho(r)), \end{aligned} \tag{6.32}$$

where r^i_{ws} is the Wigner-seitz radius, M is the Madelung matrix, and Δq_i is the net charge on site i.

The LIZ is strained in the same manner as the supercell so that the set of atoms in every LIZ remain unchanged as the lattice is strained. The local energy Eq. (6.11) obtained under the assumption that the electron density undergoes an affine scaling transformation can also calculated for isotropic strain by exploiting the virial theorem which gives in the ASA

$$\begin{aligned} 3\Omega_i P_i^{virial} &= 2\int^{\epsilon_F} \mathrm{d}\epsilon\ \epsilon n^i(\epsilon) - 8\pi \int^{r^i_{WS}} \mathrm{d}r\ r^2\rho(r)V_{KS}(r) \\ &+ 2\pi \int^{r^i_{WS}} \mathrm{d}r\ r^2\rho(r) \int^{r^i_{WS}} \mathrm{d}r'\ r'^2\rho(r') \\ &+ \frac{1}{2}\Delta q_i \sum_{j\neq i} M_{ij}\Delta q_j \\ &+ 4\pi \int^{r^i_{WS}} \mathrm{d}r\ r^2\rho(r)(\epsilon_{xc}(\rho(r)) - \mu_{xc}(\rho(r))) \end{aligned} \tag{6.33}$$

The B2 structure is chosen as a baseline for the investigation because of it's simplicity, the structure (apart from the lattice constant) is completely determined by symmetry and has only two distinct atomic sites (Fig. 6.1). Fig. 6.2 shows the local energy of the two sites of CuZn in the B2 structure plotted as a function of the atomic volume.

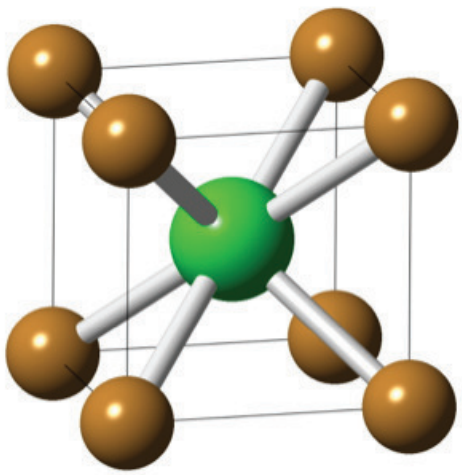

Figure 6.1: B2 structure; larger central(corner) atom represents Zr(Cu).

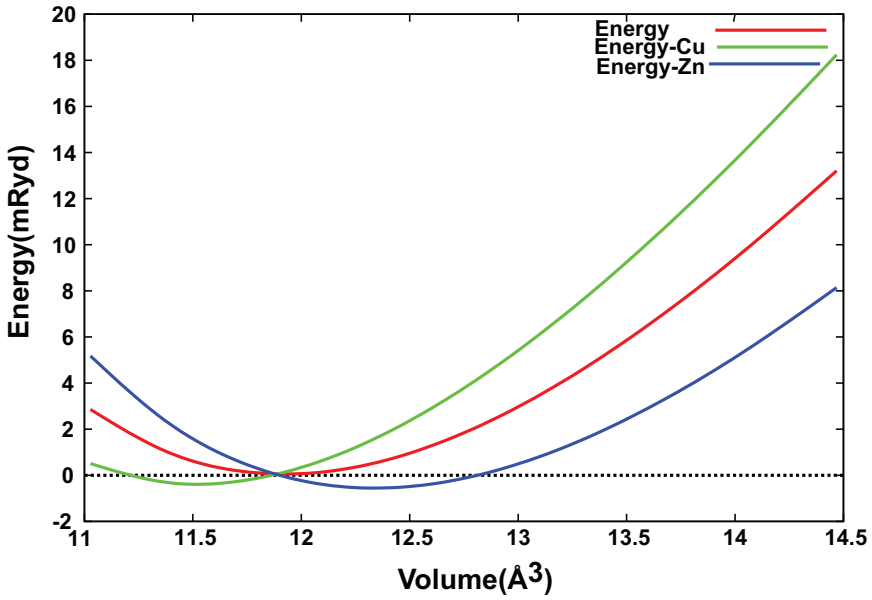

Figure 6.2: Atomic and total energy as a function of atomic volume for B2 CuZn. Curves are shifted to be zero at the equilibrium volume.

The total energy per atom, which is the average of the two site energies is also plotted. The equilibrium atomic volume is that for which the total energy per atom is minimum. The pressure, which is the negative of the derivative of the energy per atom with respect to the atomic volume is clearly zero at the minimum. Because B2 has only two atoms per cell the site pressures, (negative derivative of the site energy with respect to site atomic volume) are the negatives of each other.

The relationships between the pressure, atomic level pressures, and atomic volume are shown in Fig. 6.3. The larger atom, Zn, is found to be under positive (compressive) pressure. The local pressure given by Eq. 6.21 which assumes that the electron density scales uniformly with the volume is shown at the equilibrium volume. The fact that the virial pressure is similar to the pressure from direct numerical differentiation is expected because the electron transfer is small in CuZn.

The B2 structure is cubic and both sites also have cubic point group symmetry, therefore, the stress is completely described by the energy response to two independent types of strain, any one of the three equivalent shear strains, $\epsilon^{\alpha \neq \beta}$, and any one of

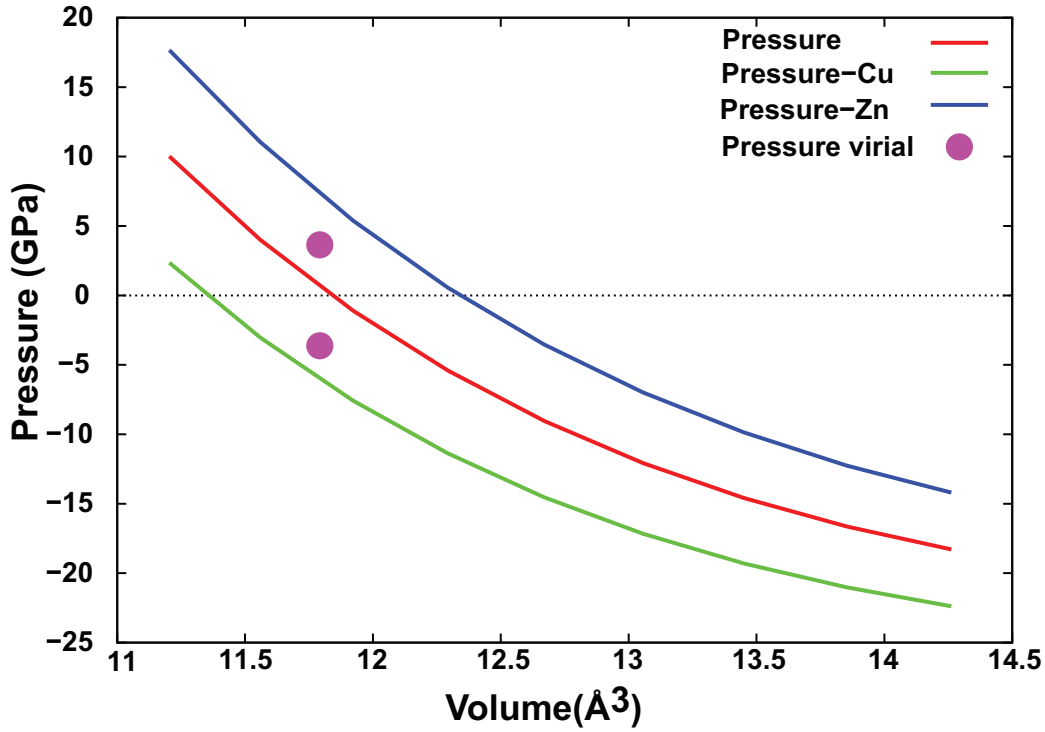

Figure 6.3: Atomic and average pressure as a function of atomic volume for B2 CuZn. The two dots indicate local pressure from virial expression at equilibrium volume.

the three equivalent tensions, $\epsilon^{\alpha\alpha}$, or their sum, $\sum_\alpha \epsilon^{\alpha\alpha} = \frac{\Delta V}{V}$, which is the volume strain. In glasses and liquids the macroscopic stress is similarly described by only two strains. The distribution of atomic level stresses will also show high symmetry; for example, the distribution of atomic level tensions in the x direction will be the same as the distribution of tensions in the y direction. The energy response to the volume strain is more amenable to the ASA, therefore, we predominately calculate the response of the local energy to changes in volume, the pressure. Exactly the same calculational procedures apply to all components of strain, the energy change in B2 CuZn with respect to fractional elongation is shown in Fig. 6.4 . Note that by symmetry the local shear stress is zero in B2. The Fig. 6.5 shows the atomic level stress verses the strain in the case of CuZn.

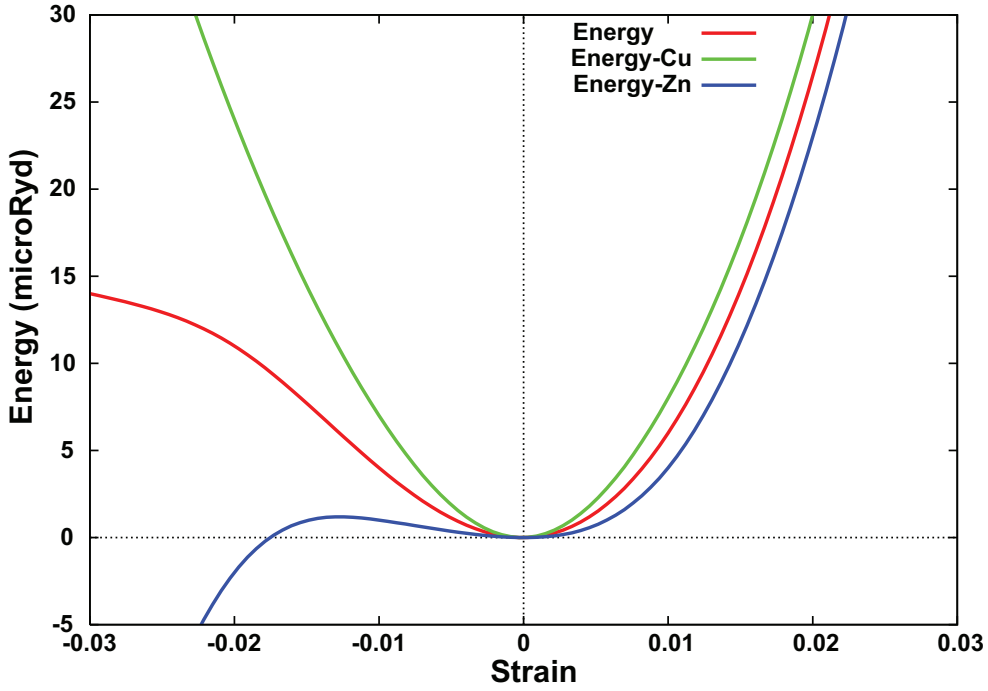

Figure 6.4: Energy versus strain in the z direction (strain in x and y directions maintain volume). Curves are shifted to be zero at the equilibrium volume.

The B2 structure is simple but anomalous; by symmetry no relaxation is possible and there are no like nearest neighbors.

The bcc random solid solution structure was investigated because it is similar to B2 but has lower symmetry and half of the nearest neighbors are like neighbors. The bcc random alloy was modeled by a small (8 atom) special quasi-random structure (SQS) (113) with specified chemical occupations on a bcc lattice.

A liquid with 50 percent stoichiometry was prepared by first principle MD at 1500K using VASP (114; 115). A 100 atom random packed structure was first equilibrated at an expanded volume for 3ps. The structure was then scaled to the experimental number density. The energy (time average) was calculated for equilibrated structures (2ps) at several nearby volumes. The system was run for 3ps at the volume corresponding to minimum average energy and the partial pair distribution functions were determined. The final configuration was taken

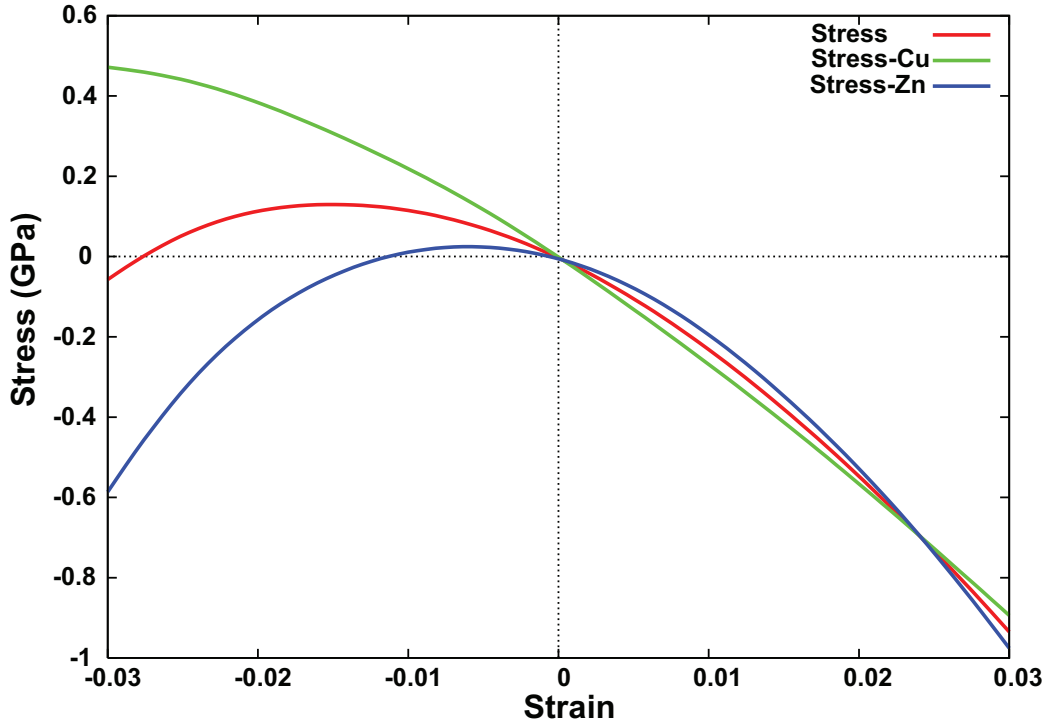

Figure 6.5: Stress versus strain in the z direction (strain in x and y directions maintain volume).

as a representative configuration for the liquid. This liquid configuration was instantaneously quenched to zero temperature and then relaxed by steepest descent to a metastable minimum; the resulting relaxed structure is taken as an approximation to the glass structure.

6.5 Results

In this paper we focus on a counterintuitive result; in CuZr the smaller atomic species, Cu, is under pressure (compressive) rather than the larger atomic species, Zr. This reversal occurs for crystalline, liquid, and glass structures. Fig. 6.6 shows this behavior, the pressure on Cu is spectacularly large for the B2 structure. In the random alloy modeled with a SQS the number of like nearest neighbors is increased from zero to four. The increase in like nearest neighbors results in the much reduced

atomic pressures in the random alloy as discussed below. The average size of the pressure on Cu and Zr atoms in the liquid is less than half that of the B2.

In all cases the average pressure on Cu is positive and that on Zr is negative. The pressures observed in the glass are slightly reduced from those in the liquid. In the liquid and glass the atoms have individual pressures that scatter between those of Cu and Zr in the B2 structure. In Fig. 6.7 some individual Cu and Zr atomic pressures agree with the intuitive notion that large atoms should be under positive pressure and small atoms should be under negative pressure, however, most exhibit the counterintuitive behavior. We have observed this counterintuitive behavior in several B2 systems, for example, NiAl. We can begin to understand this behavior by considering the pair potential expression for the difference in pressure, Eq. 6.31.

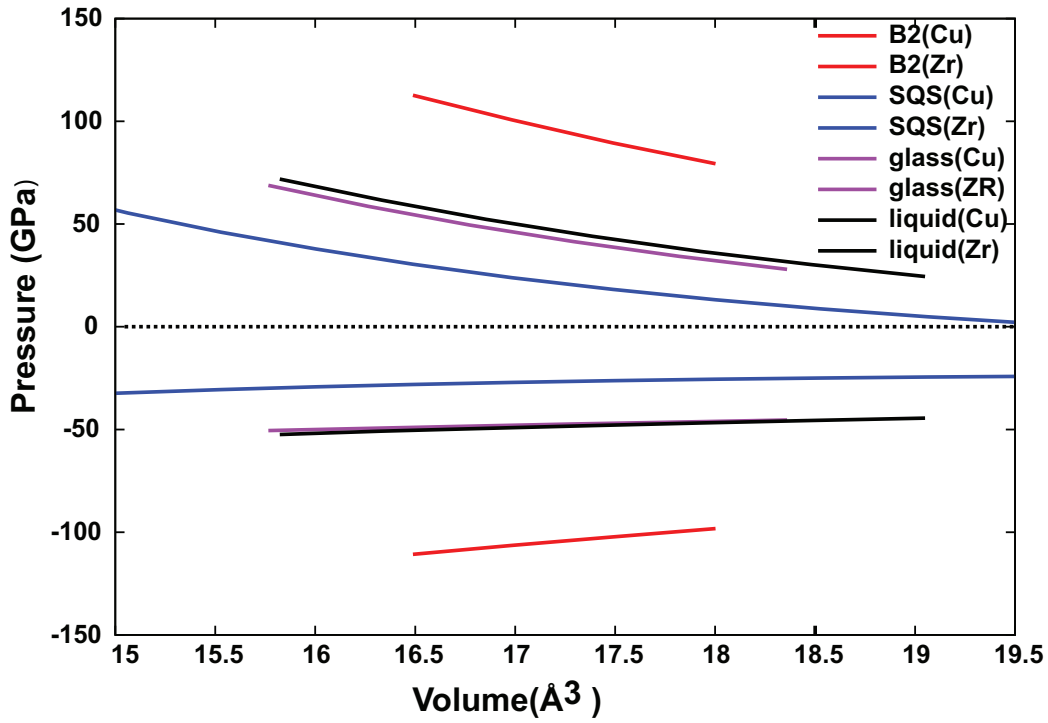

Figure 6.6: Average species pressure for CuZr in the B2, SQS, liquid and glass structures as a function of atomic volume.

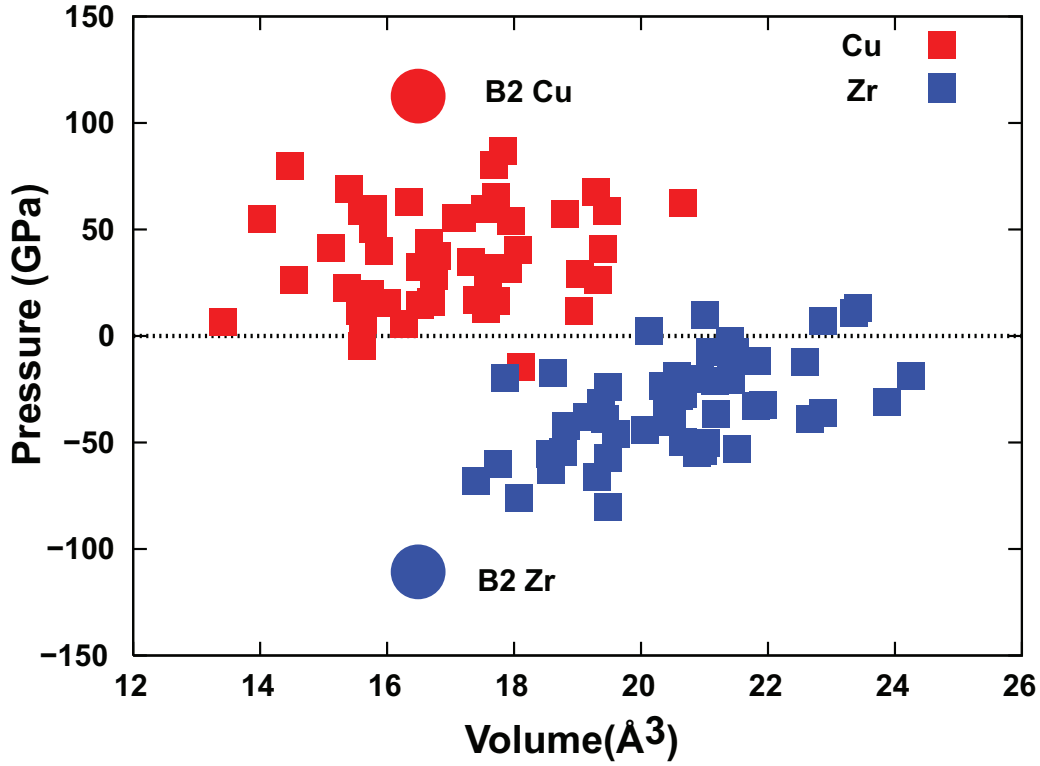

Figure 6.7: Individual atomic pressures in CuZr liquid structure as a function of individual atomic volume.

A DFT based approximate pair potential can be easily generated from the the partial pair distribution function from DFT MD at high temperature (1500K in this example),

$$V_{\alpha\beta} \approx -k_B T \, ln(g_{\alpha\beta}(r)). \tag{6.34}$$

The species diagonal partial pair distribution functions and their corresponding approximate pair potentials are plotted for CuZr in Fig. 6.8. We see that the Zr atoms are under negative pressure because they are exclusively second neighbors on the bcc lattice and therefore have a significantly larger separation than that which would align them with the minimum in the Zr-Zr potential.

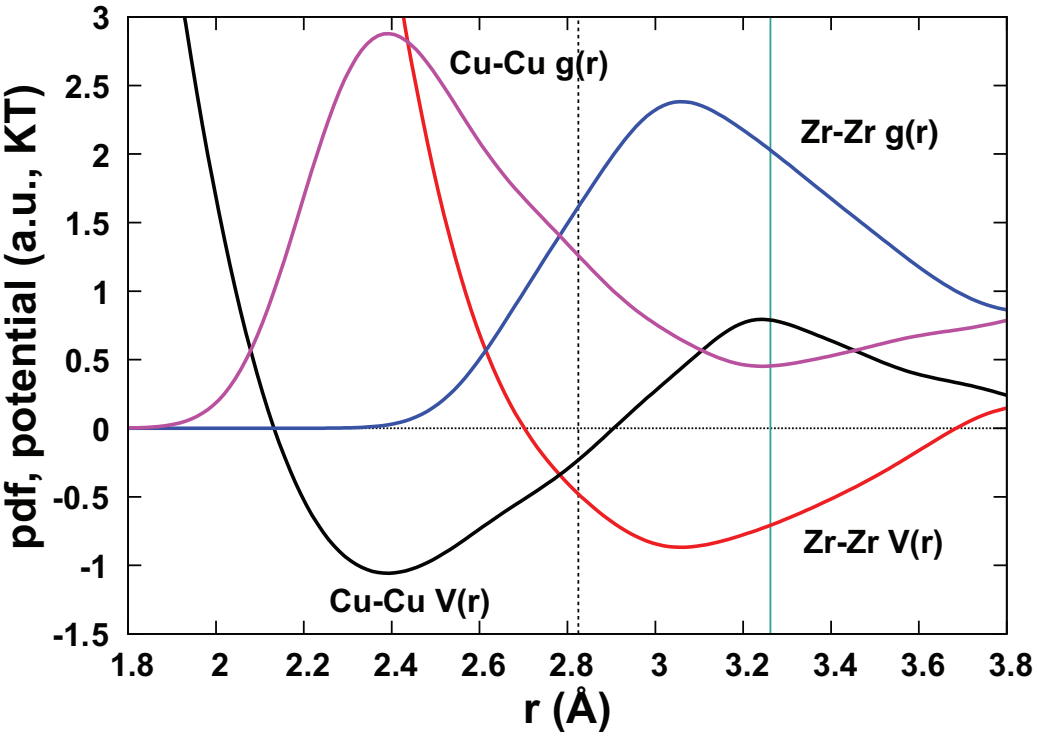

Figure 6.8: The Cu-Cu and Zr-Zr pair distribution functions and their associated approximate potentials for liquid CuZr. The first and second neighbors distance are indicated by vertical dotted and solid lines respectively.

On the other hand the smaller atom Cu are separated from their nearest Cu neighbors by a distance (exactly the same second neighbor distance that separates Zr-Zr neighbors) that corresponds to a position on the Cu-Cu pair potential that has a negative slope, indicating that the energy can be reduced by expansion. More typically the potential of the smaller atom will be near zero and slowly changing at the second nearest neighbor distance and the potential of the larger atom will be increasing with separation indicating a negative pressure. The determination of which atomic is under pressure for a pair potential model of B2 depends on the slope of the potential at separation equal to the lattice constant (assuming the interactions do not extend to the third nearest neighbors).

6.6 Discussion and Conclusions

We have discussed the various ways in which the atomic level stress can be formulated and argued in favor of basing the atomic level stress on the numerical derivative of a local energy. By numerical differentiation with relaxed electronic degree of freedom we avoid the assumption that the electron density and orbitals undergo the same affine transformation as the nuclear positions and use the actual electron density of the deformed lattice. Due to the stationary nature of the energy the accuracy of the transformation of the electron density and orbitals has no effect on the macroscopic stress, however it does affect the value of the stress components in any decomposition of the stress. This effect on stress components applies to decomposition with respect to energy type (kinetic, Coulomb or exchange-correlation) or with respect to site. We have selected a local energy that consists of the local eigenvalue sum obtained from the local DOS, pairwise Coulomb terms similar to the classical pair-potential expressions, and a local exchange-correlation term. We focus on the difference in pressure on the two atomic species in binary alloys. We were drawn in this direction because of the counterintuitive result that the larger of the two atoms was often not under compressive pressure. We analyzed this result in detail for several ordered and disordered Cu-Zr structures and concluded that the bonding in the cage of surrounding atoms controls the pressure on an atom. We propose the atomic level stress as a new tool that can contribute to the understanding of crystals and disordered materials at the atomic level.

Chapter 7

Glass Formability and Atomic level Stress in Al-Au system

A similar version of this chapter appeared as "*Glass Formability and Atomic level Stress in Al-Au system*" T. Egami, M. Ojha, D. M. Nicholson, D. Louzguine-Luzgin, N. Chen, and A. Inoue, Philosophical Magazine 92, 655 (2012)

7.1 Introduction

The ability to make glass artificially has been known to mankind for at least two millennia but our understanding of phenomenon underlying glass formation is not yet completely known, even qualitatively. Most of the glasses that are known to us and used by us are oxide glasses. Metallic glasses are newcomer in the field of glass. Rapid cooling of some binary, ternary, etc. liquid metallic alloys form metallic glasses. Because of their many technologically applicable properties they are currently the most actively studied metallic materials. Metallic glasses being atomic glasses have relatively simpler structure; hence they have been center of research for advancing our understanding of physics of liquid and glass as a whole. Formation of metallic glasses is more difficult than the oxide glasses and hence the question of metallic glass

formability is one of the most active areas of research. Metallic glass was discovered nearly 50 years ago. The first discovered metallic glass was an alloy of gold and silicon ($Au_{75}Si_{25}$). It was produced in 1960 by Duwez and co-orkers at Caltech by rapid cooling (10^6 K/s) the melt to avoid crystallization (20). Initially produced metallic glasses were in the form of ribbons, foils, or wires with cooling rates between 10^3 K/s and 10^6 K/s. Recent discovery of bulk metallic glasses with low critical cooling rate (116; 117; 118; 119) encouraged interest in this new field of metallic glass and their formability (120; 121; 122; 123). Here, Au-Al alloy, a negative test case of metallic glass formation, is discussed using first principle calculation of atomic level stresses. The Au-Si alloy, which was the first metallic glass obtained by rapid cooling has a deep eutectic around the composition of 18.6 at. % Si in the phase diagram as shown in Figure 7.1.

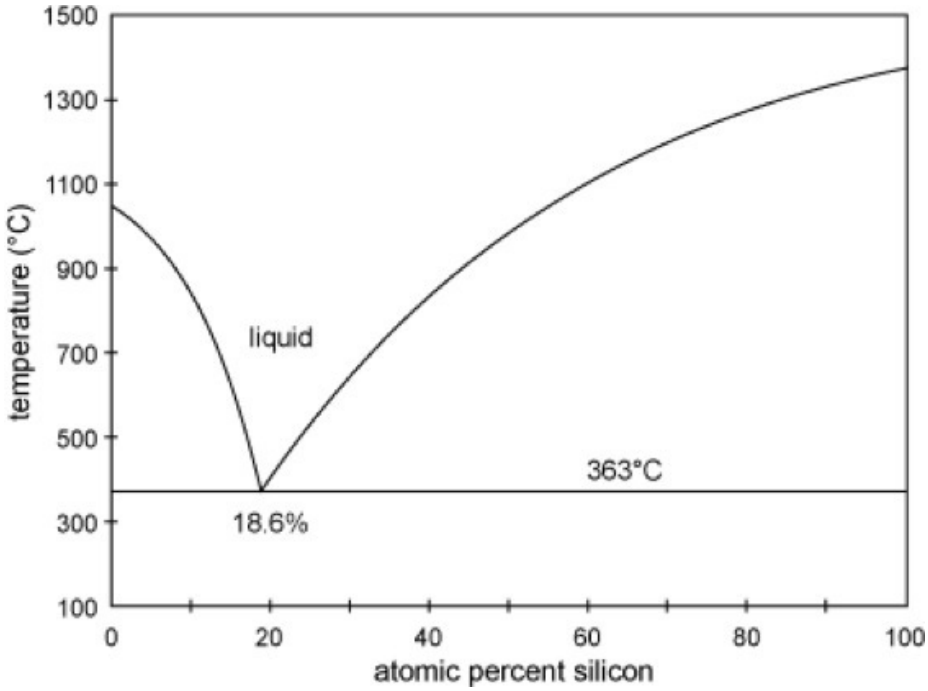

Figure 7.1: Au-Si Phase Diagram (124).

Likewise Au-Al alloy also has deep eutectic at $Au_{78}Al_{22}$. As the glass transition temperature (the temperature at which the viscosity of melt becomes approximately 10^{13} Poise), T_g does not change significantly with composition as compared to the liquidus temperature (the maximum temperature at which a crystal is at thermodynamic equilibrium with its melt), T_l. The ratio T_g/T_l is considered to be an important indicator for glass formability is increased in the presence of a deep eutectic (125).

Here, the Au-Al system has a deep eutectic as shown in Figure 7.2 as did the Au-Si system but does not form glass hinting that deep eutectic does not necessarily mean good glass forming condition. Figure 7.3 shows an X-ray diffraction (XRD) pattern of $Au_{75}Al_{25}$. When X-ray diffraction of ribbon samples (20 mm thick and 1mm wide) of Au-Al alloys were taken none of the studied sample were found do be glassy (126).

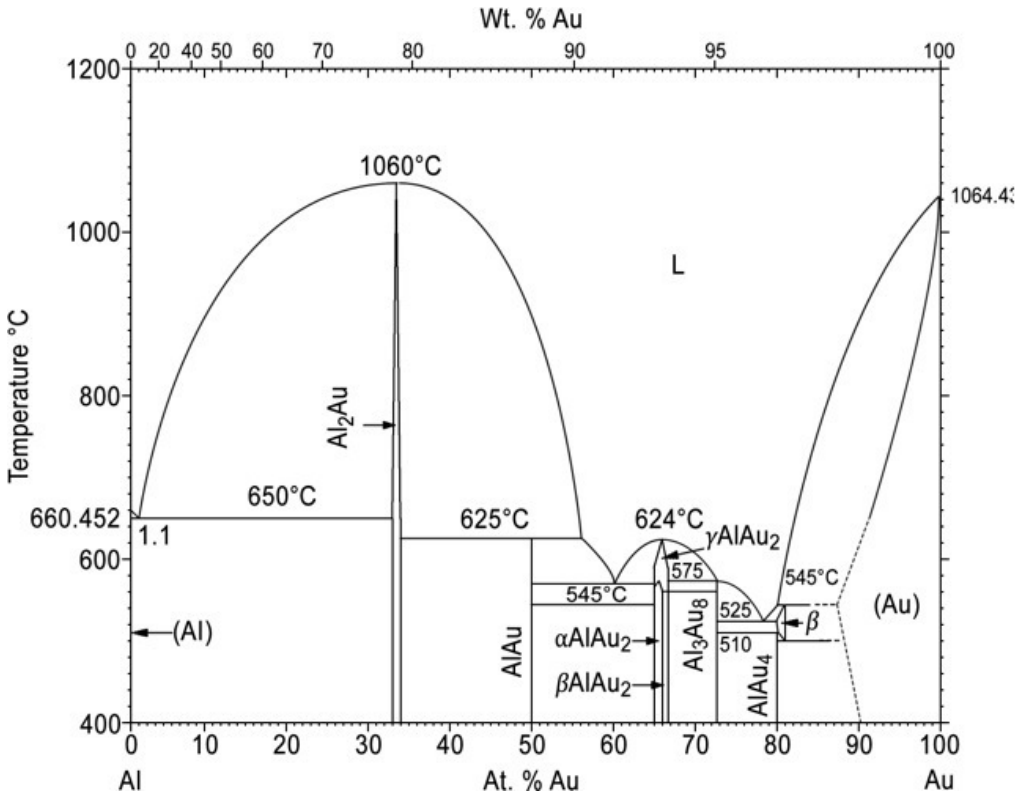

Figure 7.2: Au-Al Phase Diagram (127).

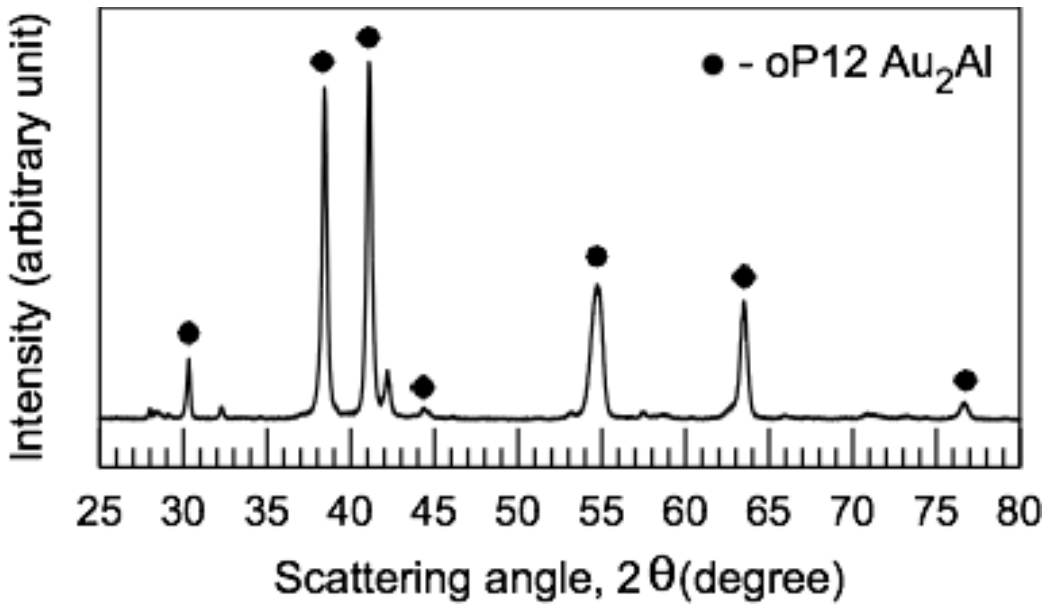

Figure 7.3: XRD pattern of rapidly solidified $Au_{75}Al_{25}$ alloys (126).

7.2 Au-Al System

7.2.1 Glass Formability

Au and Al do not form a solid solution even though both of them form FCC lattice with very similar lattice constants (a_{Al}=4.0496 $\mathring{A}$ and a_{Au}=4.0785 $\mathring{A}$). The phase diagram of Au-Al system is not simple compared to the case of Au-Si system; instead it is very complex and very unsymmetrical with one strong intermetallic compound Al_2Au (T_m = 1333 K) in the Al-rich side and many in the Au-rich side with a deep eutectic at $Au_{78}A_{l22}$ (T_m = 798K). Even though the estimated T_g/T_l ratio is equal to 0.63 (126) for the eutectic composition, which is excellent value for glass formation, this system does not form a glass.

7.2.2 Au-Al Phase Diagram

Furthermore, the heat of formation, ΔH, for the Au-Al system is -23eV/atom (128), which is strongly negative indicative of favorable criteria for glass formability. Thus, the Au-Al system satisfies both the criteria of deep eutectic and negative heat of formation but does not form glass. This system does not fulfill the condition of size difference required for the glass formation as suggested by the theory of atomic level stress (63) suggesting that this is the main reason for not forming glass. To explain this issue we performed first principle calculations on some of the representative intermetallic compounds in the Au-Al system to calculate atomic level stresses. The Au-Al phase diagram is shown in Figure 7.2. We studied three phases viz. Al_2Au in the Al-rich side and $AlAu_4$ and $AlAu_2$ in the Au rich side.

Al_2Au Phase

The Al_2Au has 12 atoms per unit cell (4 Au and 8 Al) with lattice constant 6.00 $\mathring{A}$ with symmetry space group Fm-3m as shown in Figure 7.4 (129).

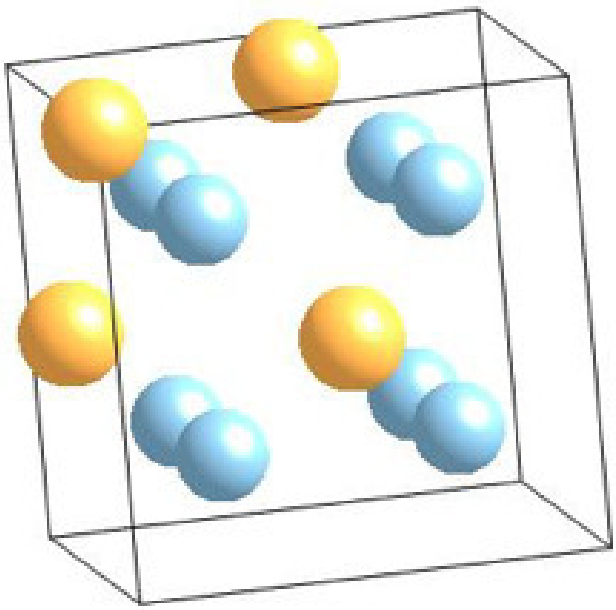

Figure 7.4: Al_2Au crystal structure showing unit cell.

It is made up of blocks of $AuAl_8$, a cubic cluster with Au at the body-center with Au vacancies in alternating $AuAl_8$ cluster as shown in Figure 7.5. The density of this phase is lower due to Au vacancies in the alternating $AuAl_8$ cluster. Also this phase has reduced Al-Au distance (2.6 $\mathring{A}$) that is less than the sum of the radii of aluminum and gold which is equal to 2.86 $\mathring{A}$

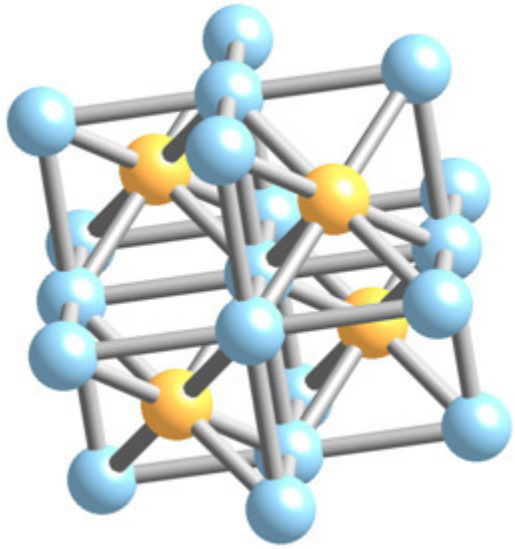

(a)

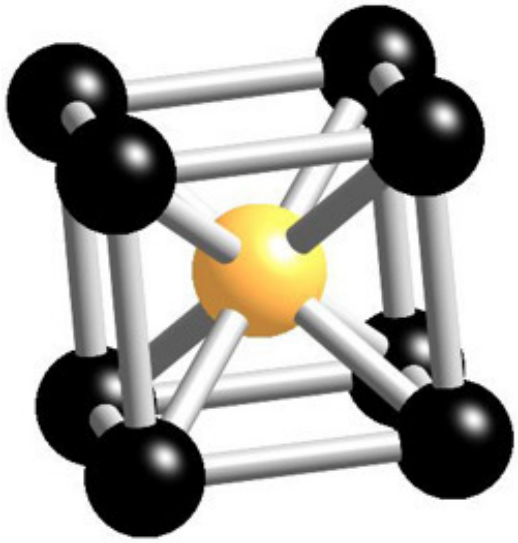

(b)

Figure 7.5: Al_2Au structure showing Au vacancies and (b) $AuAl_8$ cluster found in Al_2Au compound around Au.

$AlAu_4$ Phase

This phase is closest to the eutectic point in the phase diagram. This phase has 20 atoms in its unit cell (4 Aluminum atoms, 4 gold atoms in one environment (Au_1 site), and 12 gold atoms in different environment (Au_2 site)). The structure is very complex (β-Mn structure, P213, a=6.923 $\mathring{A}$) (130). In this phase the local structures are distorted icosahedron. A unit cell of $AlAu_4$ is shown in Figure 7.6

$AlAu_2$ Phase

There are three complex $AlAu_2$ phases (a high temperature γ phase and low temperature α and β . Here we have studied phase of $AlAu_2$ because the phase that was observed in Figure 7.3 was very close to β -AlAu2. β -$AlAu_2$ phase has the structure of oP12, with symmetry of P_{nma} with lattice constants a=6.71 $\mathring{A}$, b=3.21 $\mathring{A}$ and c=8.81 $\mathring{A}$. The structure is complex distorted $MoSi_2$ as shown in as shown in Figure 7.6b (131).

7.3 Electronic States in Al-Au

7.3.1 First Principle Calculations

Relativistic self-consistent multiple scattering (LSMS) method based on density functional theory was used to carry out first principle calculation on Al_2Au, $AlAu_2$ and $AlAu_4$ compounds. The method was used to calculate the magnitude of charge transfer, the atomic level stress (pressure) and bulk modulus in each component in these compounds.

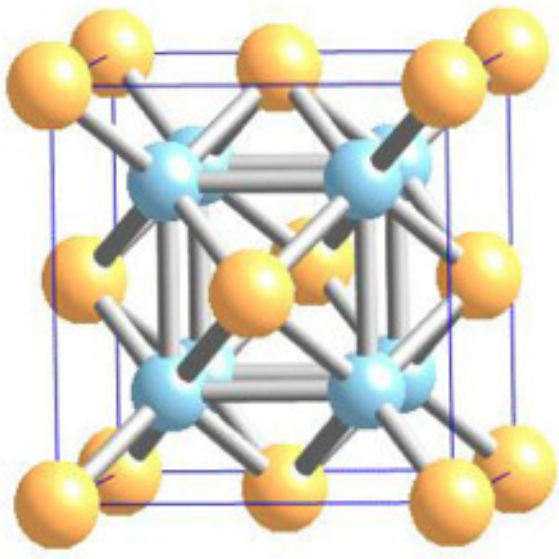

(a)

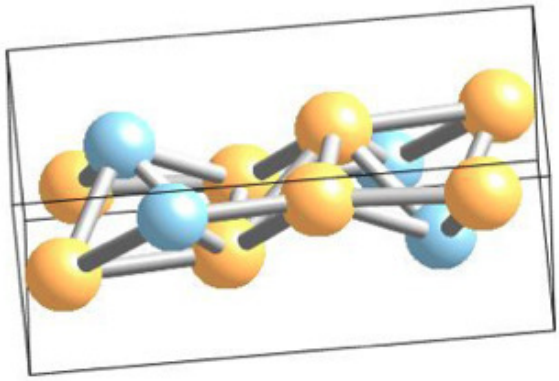

(b)

Figure 7.6: (a) Unit cell of $AlAu_4$; (b) Unit cell of$AlAu_2$.

Charge Transfer

Table 7.1 shows the excess electron in each site in these compounds and it was calculated by integration of the electron density within the Voronoi polyhedral associated with each site in each compound.

It is seen from Table 7.1 that the amount of charge transfer, in the case of Al_2Au is quite large for a metallic system. Here, the electrons move from both Al site and Au site and collect to the vacancy site making the amount of electrons at the vacancy

Table 7.1: Deviation in local electron density (electron per atom) in Al_2Au, $AlAu_2$ and $AlAu_4$.

Al_2Au		$AlAu_2$		$AlAu_4$	
Al	-0.2664	Al	-0.0226	Al	-0.1252
Au	-0.2871	Au_1	0.005	Au_1	-0.151
Vacancy	0.8192	Au_2	0.0176	Au_2	-0.0921

site approximately equal to one electron. This may be the reason that the vacancy is so stable in this compound. The amount of charge transfer is smaller for $AlAu_4$ and here charge transfer occurs from Al and Au_1 sites to Au_2 site of the unit cell. Likewise the charge transfer is even smaller for $AlAu_2$. In the case of $AlAu_2$ electrons move from Al site to Au site.

Atomic Level Pressure and Volume Strain

The total energy of the system is expressed as a sum of the local atomic level energy as given below.

$$E = \sum_i E_i \tag{7.1}$$

LSMS method was used to calculate the local response to affine deformation, ϵ_β , to obtain the atomic level stress by using the formula.

$$\sigma_i^\beta = \frac{1}{\Omega_i}\frac{dE_i}{d\varepsilon_\beta} \tag{7.2}$$

The local modulus, $C_i^{\alpha\beta}$, is given by the expression shown below.

$$C_i^{\alpha\beta} = -\frac{1}{\Omega_i}\frac{d^2E_i}{d\varepsilon_\alpha d\varepsilon_\beta} \tag{7.3}$$

The quantity, Ω_i, used in above equations is the Voronii polyhedral volume associated with each atomic site. The atomic level volume strain, e_v , is given as a ratio of atomic level stress (P) to the atomic bulk modulus (B), i.e.,

$$e_v = \frac{P}{B} \tag{7.4}$$

Table 7.2 shows the results of the calculation. The atomic level volume strain on Au in the case of Al_2Au is quite large and positive indication the atom is under compression and it wants to expand. But, the volume strain on vacancy site is low suggesting the stability of the site. The atomic level pressure on Al is negative in $AlAu_4$, which is consistent with the fact that the lattice constant gets reduced on alloying Al on Au (132). Furthermore, the volume strain on Al is strongly negative and exceeds unity thereby invalidating the linear approximation. Therefore, in this case the atomic level volume can give semi-quantitative explanation of the effect of atomic level pressure. Also, we see that the atomic level volume strain in the case of $AlAu_2$ is smaller than in $AlAu_4$ but it is substantial.

7.3.2 Electron Density, Fermi Level and Charge Transfer

Looking at the electronic configurations of Aluminum ([Ne] $3s^2 3p^1$) and Gold ([Xe] $4f^{14} 5d^{10} 6s^1$) we see that Au has a filled 5d shell and only one 6s electron but Al has three 3s-3p valence electrons and hence the electron density of Al is much higher than that of Au. Furthermore, the Fermi energy of Al (11.6 eV) is higher than that of the Au (5.5 eV). Also, there is a large difference in electronegativity of the two elements [$(Electronegativity)_{Al} = 1.5$ and $(Electronegativity)_{Au} = 2.4$]. These facts suggest to us that there is a strong likelihood for electron flow from Al to Au when they form an alloy.

In metals there is a tendency for this charge transfer to be screened. Atoms can maintain ionic character by strong charge transfer as in the case of some conducting oxides if the density of conduction electrons is very low and the screening length of

Table 7.2: Deviation in local electron density (electron per atom) in Al_2Au, $AlAu_2$ and $AlAu_4$.

Al_2Au		$AlAu_2$		$AlAu_4$	
P_{Al}	-43.56	P_{Al}	-66.36	P_{Al}	-70.86
P_{Au}	82.82	P_{Au_1}	33.62	P_{Au_1}	30.28
P_{Vac}	6.78	P_{Au_2}	29.88	P_{Au_2}	11.61
B_{Al}	178.20	B_{Al}	159.60	B_{Al}	66.58
B_{Au}	167.25	B_{Au_1}	171.81	B_{Au_1}	278.81
B_{Vac}	106.87	B_{Au_2}	233.26	B_{Au_2}	244.61
e_{v}^{Al}	-0.2440	e_{v}^{Al}	-0.4158	e_{v}^{Al}	-1.0640
e_{v}^{Au}	0.4952	$e_{\mathrm{v}}^{Au_1}$	0.1957	$e_{\mathrm{v}}^{Au_1}$	0.1086
e_{v}^{Vac}	0.0634	$e_{\mathrm{v}}^{Au_2}$	0.1281	$e_{\mathrm{v}}^{Au_2}$	0.0475

Friedel oscillation (π/k_F) is much larger than the intermolecular distances. In the Au reach side of the phase diagram the length of Friedel oscillation is about 2 $\mathring{A}$ and hence large charge transfer cannot take place from Al to Au due to screening effect. As shown in Table 7.2 the amount of charge transfer is small in the case of $AlAu_2$ and $AlAu_4$. This also justifies why the effective size of Al in Au (1.382 $\mathring{A}$) is not very different from the atomic size of Al in FCC lattice (1.425 $\mathring{A}$) (132). Generally large charge transfer results into changes in size of the atoms in alloys. Here in the Au rich side the Al atoms are trapped into the volume nearly equal to the volume of Al atoms in FCC lattice and hence are not able to transfer large charge to Au atoms. As a result Al atoms in $AlAu_4$ are under considerable pressure to expand as shown in Table 7.2. But, the pressure on Au atoms is not that large.

We found that the amounts of charge transfer in Al_2Au (as shown in Table 7.1) are quite large for metals. But, it is interesting to note that the electrons are not transferred between Al and Au but they flow out from both Al and Au and are

collected at the vacancy site. Evidently, the presence of vacancy in this structure is an important feature, which made the strong charge transfer possible. The coulomb energy associated with the transferred charge greatly plays a part in the stability of the vacancy in this compound and the stability of the compound itself. Also, in this compound the Al-Au distance is reduced by 9% which is significant even though both Al and Au are positively charged. As Al has high electron density the screening length (π/k_F=1.8 $\mathring{A}$ for Al) is shorter than the Al-Al and Au-Au distances. Because of this reason it is easier to change the electron density locally to screen and suppress charge transfer, and to form localized Al-Au covalent bond. Thus, the case of Al_2Au is atypical in structure as well as in the amount of charge transfer.

7.3.3 Origin of the Deep Eutectic

The above discussion provides important clues about the origin of the deep eutectic on the right side (i.e. Au rich side) of the Al-Au phase diagram. Deep eutectics happen most commonly due to the instability of solid solution, e.g. due to size difference. As the effective size difference between Al and Au is at most 4% and hence the eutectic in this case is not due to the size effect.

It seems that the origin of the instability of crystalline phases on the right side of the Al-Au phase diagram is electronic. As discussed above in the Au-rich side of the charge transfer is greatly blocked. This leaves Al atoms strongly frustrated with high pressure. Thus, we can say that this electronic frustration must be the origin of the instability of the compounds such as $AlAu_4$. This electronic frustration is reflected in the structures of intermetallic compounds $AlAu_4$ and $AlAu_2$. Icosahedra clusters and strong local distortions are found in the local structures of $AlAu_4$ phase and these structures must be very similar to the structures that are found in liquid phase. Furthermore, the $AlAu_2$ also shows frustration and compromise thereby making the energies of the compound high and similar to that of the liquid phase. Therefore,

the above mentioned structural and electronic frustration must be the origin of the presence of deep eutectic in the Al-Au phase diagram.

7.3.4 Glass-Forming Ability

Figure 7.7 shows the local environments of Al, Au_1 and Au_2 in the case of $AlAu_4$.

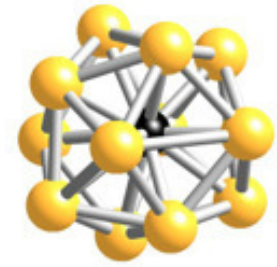

(a)

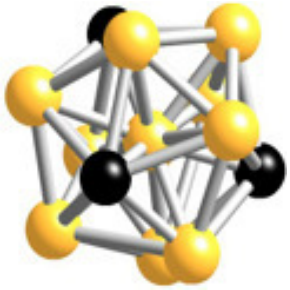

(b)

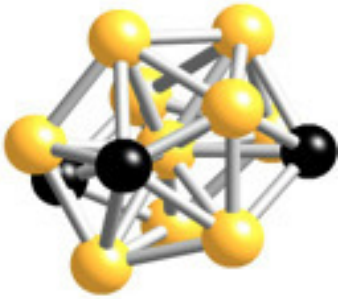

(c)

Figure 7.7: (a) Environment of Al in $AlAu_4$ (distorted icosahedra); (b) Environment of Au_1 in $AlAu_4$ (distorted icosahedra); (c) Environment of Au_2 in $AlAu_4$ (defective and distorted icosahedra).

To explain the experimental demonstration of supercooling by Turnbull (133). Frank suggested that the liquid should possess icosahedra clusters, and the major difference between the structure between the crystal and liquid makes the interfacial energy between the two phases large and hence nucleation is difficult (134). In the Au reach side of the phase diagram the crystal structure of $AlAu_4$ is already basically made of icosahedra as shown in Figure 7.7 and contains much distortion.

Likewise, the local structure of $AlAu_2$ has many pentagons and heptagons as shows in Figure 7.8.

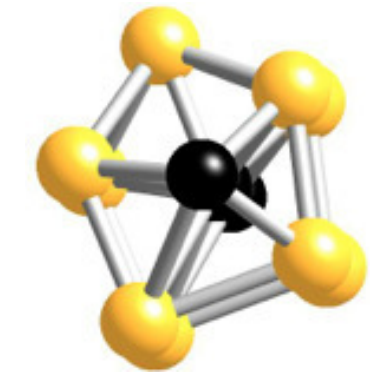

(a)

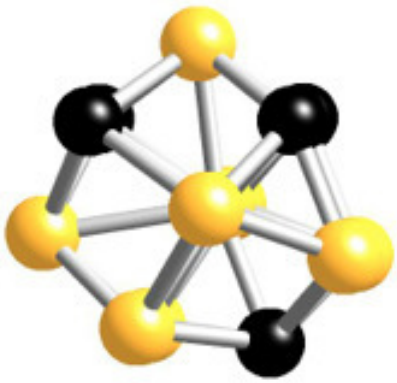

(b)

Figure 7.8: (a) Local pentagonal atomic arrangement around Al in $AlAu_2$; (b) local heptagonal atomic arrangement around Au in $AlAu_2$.

From this it is seen that the structures of $AlAu_2$ and $AlAu_4$ crystals and liquids are not very different. This makes the interfacial energy low and thereby making nucleation easy. According to the theory of critical solute concentration for glass formation, a glass is formed as a default when the solid solution is not stable (63). In this theory the limit of solute solution was calculated through the atomic level strain. The Al-Au system discussed here finds this theory useful to explain the glass forming ability in this system.

As the formation of crystalline phase in the Au rich side is compromised by electronic frustration resulting into unstable crystalline phases that produces a deep eutectic but at the same time the similarity between the structures of the crystalline and liquid phases lowers the kinetic barrier, making glass formation difficult.

The case of Al-Au suggests that if the heat of formation is too strongly negative glass formation is not possible because it helps the formation of strong intermetallic compounds as we see in Al_2Au in the Al rich side of the Al-Au phase diagram. Furthermore, the formation of cluster, in liquid instead of helping the formation of glass (135) is detrimental to glass formation because it stabilizes crystals. Strong local bonds that reduce configuration entropy cannot be good for metallic glass formation because a liquid is stable due to its high configurational entropy.

7.3.5 Conclusion

Glass formation is complex phenomena. It depends on properties such as interfacial energy between liquid and glass, which are difficult to determine. To understand it we need other information in advance viz. the glass transition temperature, the crystallization temperature. Therefore, estimating the glass formability is more of an art than science. The atomic size effect for binary alloys is the only theoretically studied factor for glass formation (63; 136). In this case also the definition of atomic size is not unambiguous.

Here, we discussed the reasons why glass formation is not possible in Au-Al system despite the fact that it shows deep eutectic on the Au-rich side of the phase diagram and the estimated T_g/T_l is high. We explained it by discussing the charge transfer, the atomic level stress, effective atomic radius, local cluster formation, electronic frustration and interfacial energy. The arguments made here are partially supported by the computed results of charge transfer and atomic level stresses, which are evaluated using first principle calculations.

Chapter 8

The Use of Atomic Level Stress to Characterize the Structure of Irradiated Iron

A similar version of paper "*The Use of Atomic Level Stress to Characterize the Structure of Irradiated Iron*" Madhusudan Ojha, D. M. Nicholson, Bala. Radhakrishnan, R. E. Stoller, and Takeshi Egami has been submitted to CCP 2011 Conference proceedings.

8.1 Introduction

Radiation damage occurs when a highly energetic particle incident on a solid transfers its energy to the atoms in the solid displacing atoms from their original crystal lattice positions through absorption of energy in excess of the displacement threshold energy. This displacement of atoms creates vacancy (V) and interstitial (I) defects in pairs, Frenkel pairs. The initially displaced atom is called the primary knock-on atom (PKA); it interacts with other atoms in the crystal displacing them from their lattice sites and thereby generating a displacement cascade. Thus, irradiating a solid with

ions or neutrons creates a cascade of Frankel pairs. This process continues until the crystal absorbs all the energy of the incident particle. In the case of iron, the cascade continues to generate defects until no single atom has energy in excess of the displacement threshold energy (40 eV in Fe) to cause further displacements. The remaining kinetic energy is eventually taken away by lattice phonons.

A complex sequence of events is initiated by the irradiation, which produces mainly undesirable changes in the materials properties. The radiation damage caused by fast neutrons to solids is due to the direct transfer of kinetic energy in the range of several tens of keV to the lattice atoms. This transfer happens on a length scale of nanometers and in the time scale of sub-picoseconds (ps) to a few ps. Figure 8.1 shows the evolution of Frenkel pairs in displacement cascades in alpha iron at 100K for different PKA energies (137).

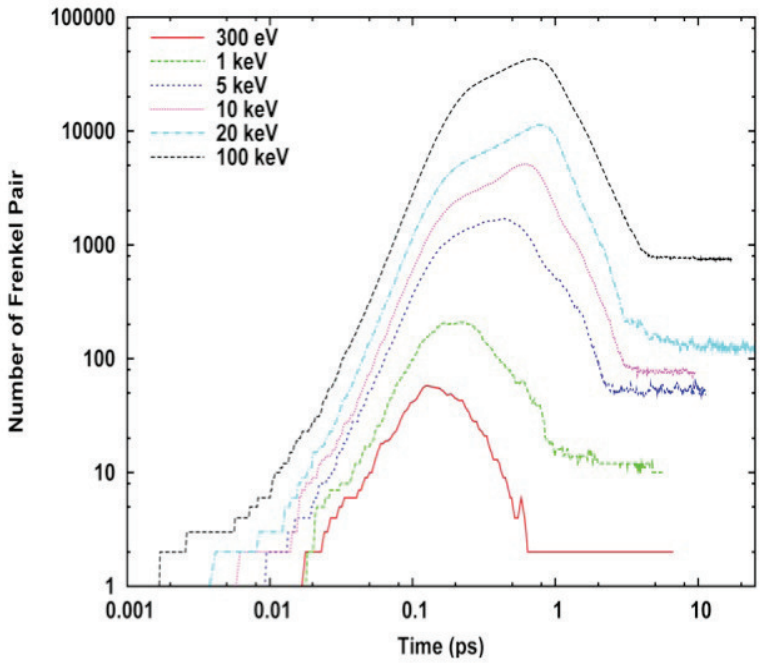

Figure 8.1: The calculated (Modified Finnis and Sinclair (80) molecular dynamics (MD)) number of Frenkel pairs is shown as a function of time after cascade initiation for a series of PKA energies.

A detailed and basic understanding of the initial damage event itself is very important to understand all the later events and the changes caused by radiation damage in microstructure and mechanical properties.

8.2 Local Energy and Pressure

A general first principles approach to the problem of defining the local stress (64; 105) is to start by defining a first principles local energy associated with each atom in the system. The local stress can then be determined from the response of the local energy to the application of small affine strains to the system. The local stresses and elastic moduli can be determined by the first and second derivatives of the local energy with respect to strain. In this paper we make a single, simple choice for the definition of local energy and observe the correlation of several local quantities with the local pressure. The local stress has been used for systems that interact through classical potentials to explain glass stability (103) and as the basis for an equipartition theorem (90) for local elastic energy in MD simulations. For classical pair potential systems the local stress has been derived on the basis of pairwise forces without resorting to the definition of a local energy (12). This result has been extended to the Embedded Atom Method (138; 139; 140), which has force fields that include many-body interactions. For both these types of force fields, expressions can be obtained by first defining a local energy and then evaluating the variation of the local energy with respect to strain, for example an atom can be assigned a local energy given by half the energy of bonding with each atom within the range of the potential.

In the ideal gas limit there are no forces and the only stress is the pressure that results from collision with the walls of the container. In another extreme case, a zero temperature solid, nuclei are stationary and forces are present but sum to zero on each atom. Even though the forces on each atom sum to zero they can contribute to large local stresses, for example: in intermetallic compounds, defects in single component materials, or even in single component perfect crystals if the volume differs from the

equilibrium value. Here we will ignore the pressure due to the motion of the nuclei and will evaluate the contribution from the electron bonding. This bonding includes electron but not nuclear kinetic energy.

The energy of the electron-nuclear system is the foundation of the Density Functional Theory (DFT) based calculations (14) . The energy is often separated into the kinetic energy, T_S, of an auxiliary system with the same electron density as that of the interacting ground state, the classical electrostatic energy of all charges in the system, U_c, and correction energy, E_{xc}, that accounts for the correlation (including that which results from exchange) between electrons. The correlation affects both kinetic and electrostatic energy. The challenge is to further decompose the energy into local contributions that have the greatest descriptive power.

In the Local Density Approximation (LDA) (15), E_{xc}, is defined locally; this makes the association with an atomic site apparently straightforward. Although we will take local E_{xc} to be given by the integral over the local atomic volume of the product of the electron density and its energy density, we acknowledge that other assignments are possible especially when approximations beyond LDA are considered.

The kinetic energy can be evaluated as the negative of the expectation value of the Laplacian. A natural choice for the local contribution is that obtained by limiting the expectation value integral to the volume of the atomic site. An alternative choice is based on the symmetric form of the kinetic energy, which is the integral of the modulus squared of the gradient of the wave function. The two definitions differ by a surface integral that vanishes over the boundary of the supercell or at a boundary at infinity if the system is finite. We argue in favor of the asymmetric form because: 1) it has the form of an expectation value, 2) it conforms to our physical notions, that the kinetic energy contribution is highest at the potential minimum (as opposed to zero for the symmetric form) for a harmonic oscillator in its ground state, and 3) it is more closely associated with the sum of eigenvalues, a quantity that has proved very useful in qualitative descriptions of bonding.

Because the classical electrostatic force is pairwise, the underlying nature of the classical electrostatic energy is that of a pair interaction. It can be recast as a local quantity by considering half the bonding energy of the local electron density with all the system charge (because it is classical it includes the self-interaction of electrons) and half the bonding of the local nucleus with all other charge. The classical electrostatic interactions are hence treated in exactly the same manner as in the classical formula for the stress in a classical pair-potential system. The treatment of the classical electron-electron interaction differs only in that the electron is treated as a continuous distribution; this leads to the inclusion of self-interaction, which is absent in the case of force fields, being excluded by the ij exclusion on energy sums.

$$E_i^\lambda = \int_{V_i} dr \left[-\sum_{\varepsilon_i<\varepsilon_F} \psi_k^{\dagger\lambda} \nabla^2 \psi_k^\lambda + n^\lambda \left\{ \tfrac{1}{2} e^2 \varphi_e \left[n^\lambda \right] - \sum_j \frac{e^2 Z_j}{\left| \vec{r} - \lambda \vec{R}_j \right|} + \varepsilon_{xc} \left(n^\lambda \right) \right\} \right] + \tfrac{1}{2} \sum_{j \neq i}^{N} \frac{e^2 Z_i Z_j}{\left| \lambda \vec{R}_i - \lambda \vec{R}_j \right|} \tag{8.1}$$

$$n^\lambda = \lambda^{-3} n^\lambda (\vec{r}/\lambda) \tag{8.2}$$

$$\psi^\lambda = \lambda^{-3/2} \psi^\lambda (\vec{r}/\lambda) \tag{8.3}$$

$$P_i = -\left. \frac{dE_i^\lambda}{d\lambda} \right|_{\lambda=1} \left(\frac{dV_i}{d\lambda} \right)^{-1}; \frac{dV_i}{d\lambda} = 3V_i \tag{8.4}$$

8.3 Procedure

Calculations were performed with the Locally Self-Consistent Multiple Scattering Method (LSMS) (17; 18) on 9826 cores of Jaguar-PF, a high performance computer of the Oak Ridge Leadership Computing Facility. The electron multiple scattering includes atomic scattering up to $l = 3$ for atoms within 7.5 $a.u.$ and to $l = 2$ out to 11.3

$a.u.$ The local Kohn-Sham potential was treated in the Atomic Sphere Approximation (19). We applied the LSMS to calculate the atomic level pressure of a 9826-atom sample of alpha Fe after a PKA with a velocity in the [113] direction that corresponds to an impulse delivered by a 1 keV neutron. The sample was initially in equilibrium at a temperature of 100K, periodic boundary conditions were in effect, the pressure was maintained at zero, and the atoms moved according to embedded atom forces integrated with variable time steps to account for initially high atomic velocities (96). Specifically, the MOLDY-MD code (83) was used with the force fields developed by Finnis and Sinclair (76) as modified by Calder and Bacon (80) . The LSMS calculations correspond to a time 3.6 ps after the initial impact.

8.4 Distribution of Volume and Pressure

The variation of the local Voronoi polyhedron (VP) volumes is depicted in Figure 8.2; sphere sizes indicate the difference in volume from the average; color also indicates the difference from the average, red is expanded and blue is contracted.Therefore, the sites with volume very close to that of the bulk appear as small white dots. At a particular instant of time the VP-volumes vary from site to site due to the thermal motion of the atoms; there are also significant changes in VP-volume at defects. Furthermore, the impulse from the cascade initiates a pressure wave that reflects from the periodic boundary conditions. Multiple reflections from the boundaries of our small cell result in modulation of the strain field over a length scale of many lattice spacings that results in the extended red and blue regions in the figure. In figure 8.3 the local pressure at each site is shown. The representation is identical to that of the VP-volumes; sites with pressure near zero appear as small white dots. Comparing Figures 8.2 and 8.3 a correlation between volume and pressure can be seen.

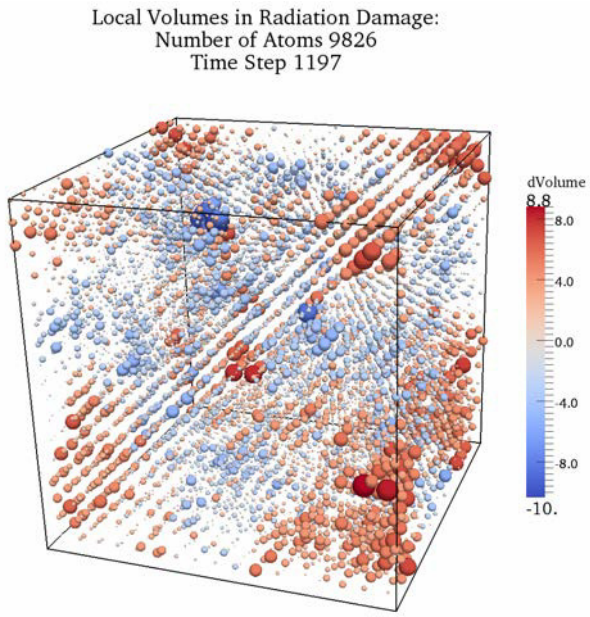

Figure 8.2: Deviation of VP-Volume from average (79.5 $a.u.$)

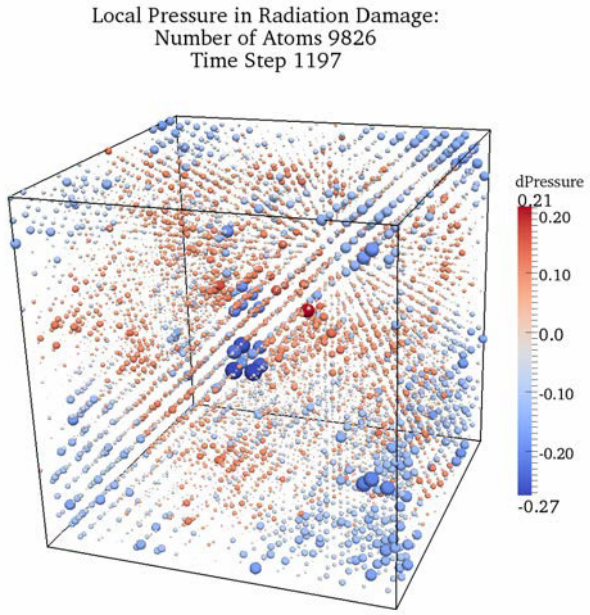

Figure 8.3: Deviation of local pressure from average value ($a.u.$).

In Figure 8.4 the VP-volumes appear correlated with the pressure in a natural way, compressive (positive) pressure is associated with lower volume. Although the volumes at a particular pressure have considerable scatter, the maximum volume appears to be clearly demarked by a line, a line of critical volume as a function of pressure. For a given pressure the population of VP-volumes lies overwhelmingly below this line. Its slope defines a pseudo bulk modulus, B_c=-VdP/dV, of 134 GPa. By construction, the average derivative of pressure with respect to volume (multiplied by the negative of the volume) of all local pressures is the actual bulk modulus, B. For comparison the volume versus pressure curve is shown for a perfect crystal of alpha iron at zero temperature calculated to the same level of approximation as the 9826-atom damage-sample.

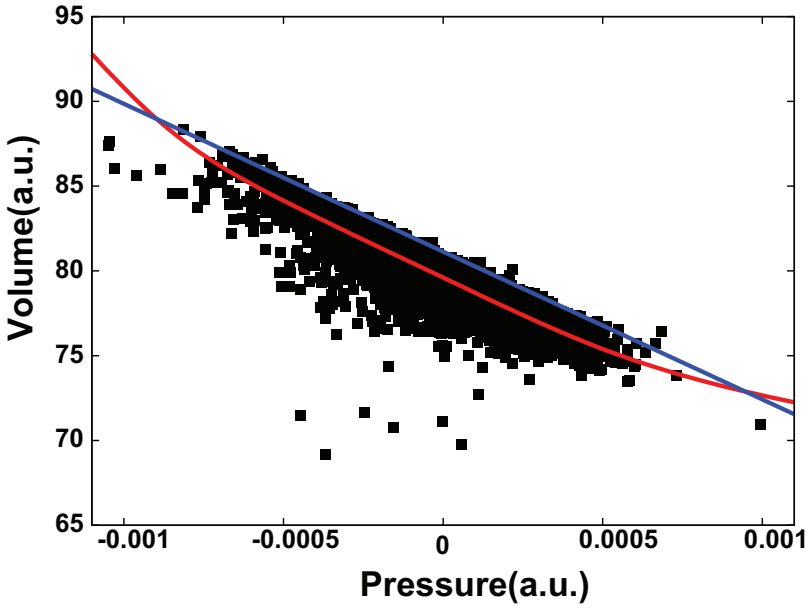

Figure 8.4: Distribution of VP-Volumes as a function of local pressure. The straight-blue line indicates an upper or critical limit on volume as a function of pressure in the damaged-system. The curved-red line is the volume versus pressure curve for perfect crystal.

The perfect crystal line passes through the center of the distribution of points, showing that the average distribution of volumes as a function of pressure in the damage-sample is reproduced approximately by volume versus pressure curve of the perfect crystalline-sample for most of the pressure range. The two lines cross at low and high volumes. The high volumes on the critical line in the damage-sample have a smaller compressibility than the perfect crystal while those at low volume have a greater compressibility. It will be interesting, in further studies, to determine whether or not, under increased hydrostatic pressure, the sample as a whole responds mainly through a reduction of volume of sites at the critical volume.

Magnetic moments also decrease with pressure. This is a correlation that is affected through the volume; the bandwidth increases as the distance to neighbors is reduced, resulting in a smaller exchange splitting. Figure 8.5 shows the local moments as a function of pressure; for comparison the atomic moment in perfect bulk Fe calculated in exactly the same way is also shown. The bulk moment provides an upper bound to the moment at each pressure. The same relationship is found in plotting the moment versus volume as shown in Figure 8.6. The size of the local moment can be explained in part by the change in volume but other aspects of the local atomic environment are clearly important. We have not attempted to analyze the local moment in terms of local geometry other than the local volume. A clear next step is to correlate the moment with the local value of the overlapped electron-density evaluated with an Embedded Atom Method as was proposed by Dudarev (141).

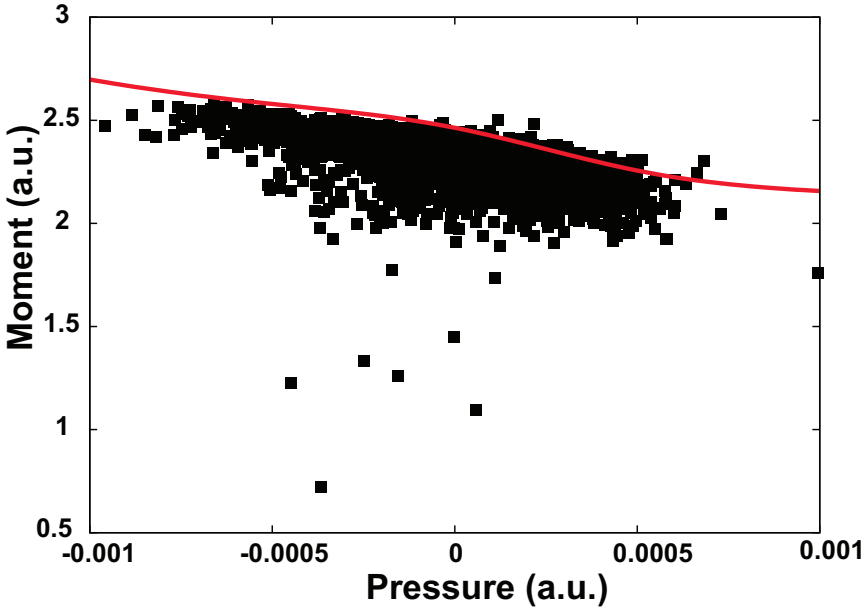

Figure 8.5: 4 Distribution of local moments as a function of local pressure. The red line indicates the moment versus pressure curve for perfect crystalline alpha Fe.

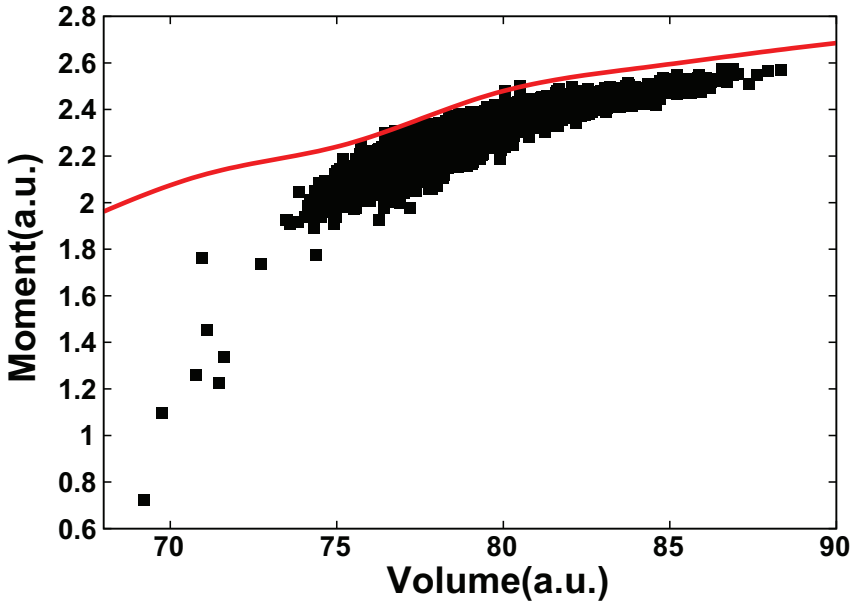

Figure 8.6: Local moments as a function of VP-volume; red line is the moment per atom in perfect crystal. The data seems to show the Stoner criticality.

8.5 Conclusion

We have briefly described first principles local stress and computed the local pressure for a sizable (9826 atom) model of a single time step in the evolution of a radiation cascade. We find the local pressure to be correlated with other local quantities in a way that is reasonable and aids in our understanding of connection between different local environments and local properties. We propose that the sensitivity of the local stress to the local atomic environment will lead to its expanded use in understanding materials behavior at the atom level. In this paper we have made comparisons only to the local pressure in perfect bulk iron. Planned further comparisons include, for example, to other time steps within the cascade and to the same size system but with thermal displacements only. Further comparisons with samples at other temperatures, ambient pressure, and with impurities will clarify the meaning of the local stresses and add to its utility as a descriptive tool.

Chapter 9

Summary

Describing the structure and dynamics in the disordered materials is a challenging problem in physics. In this dissertation we make progress towards meeting this challenge by using the dynamic pair density function and atomic level stresses to characterize these materials at the atomic level.

The use of the dynamic pair-density functions to analyze liquid iron at high-temperature showed that in high-temperature liquids the dynamics is controlled by the first nearest neighbors. This localization of the dynamics to the nearest neighbor validates the equipartition theorem for the atomic level stresses observed in models of liquid iron based on pair-wise potentials.

The use of the pair density functions in an inhomogeneous, non-equilibrium system of radiation damaged Fe showed commonality of behavior between the radiation-damaged sample and the super-cooled liquid. Analysis in terms of the PDF and MSD of the heart of the cascade is shown to be useful for locally describing the radiation damage.

We introduced the quantum-mechanical method to calculate the atomic level stresses. This method relies upon a specific decomposition of the total energy into contributions from each atomic site. We discuss the detailed distinction between evaluating changes in the site energy with respect to deformation and the accepted

alternative method of evaluating changes in the site-integrated-virial-stress-density. We argue in favor of numerical differentiation of the site energy for determination of the atomic level stress. We relate the atomic level stress to the bonding among the cage of surrounding atoms. Depending on the neighbor bonding, the pressure on atoms can differ from the intuitive notion that lager atoms will be under compressive pressure. We give results for such a situation in CuZr. The local pressures of liquid and glass structures are compared to values for Cu-Zr and other elements on bcc lattices.

Glass formation is a complex phenomenon. It depends on properties such as the interfacial energy between liquid and glass, which are difficult to evaluate. We discussed the reasons why glass formation is not possible in the Au-Al system despite the fact that it shows a deep eutectic on the Au-rich side of the phase diagram and the estimated T_g/T_l ratio is high. We discuss this behavior in terms of charge transfer, atomic level stress, effective atomic radius, local cluster formation, electronic frustration and interfacial energy. The arguments are partially supported by the computed results of charge transfer and atomic level stresses, which are evaluated using first principle calculations.

First principle local stresses are computed for sizable (9826 atom) model of a single time step in the evolution of a radiation cascade. The local pressures are found to be correlated with other local quantities such as magnetic moments and volumes. This shows that the atomic level pressure is sensitive to the local environment and will help us to expand our knowledge of material behavior at the atomic level. Thus the atomic level stress can have great utility as a descriptive tool.

Future work will extend the exploration of the CuZr composition range, extend calculations to include ternary and quaternary alloy additions, and make connections between local stress/strain and measured macroscopic residual stress and local dynamics. Comparison of the dynamic PDF, atomic level stress, and fluctuations in atomic level stress will establish a direct connection to measurements.

In the future we will expand our simulations of CuZr with respect temperature and simulation time, so that we can explore liquid behavior as the glass transition is approached and compare to the properties of the instantaneously-quenched-glass.

We have developed a set of first principle procedures and codes that are generally applicable to disordered materials and relate forces, stresses, and dynamics to each other at the atomic level.

Bibliography

Bibliography

[1] D. Alfe, G. D. Price, and M. J. Gillan, Physical Review B **64** (2001). 1

[2] C. J. Byrne and M. Eldrup, Science **321**, 502 (2008). 2

[3] G. S. Armatas and M. G. Kanatzidis, Nature **441**, 1122 (2006). 2

[4] S. Weiner, I. Sagi, and L. Addadi, Science **309**, 1027 (2005). 2

[5] A. Hedler, S. L. Klaumunzer, and W. Wesch, Nature Materials **3**, 804 (2004). 2

[6] P. Anderson, Science **267**, 1615 (1995). 3

[7] J. Langer, Physics Today **60**, 8 (2007). 3

[8] M. Telford, Materials Today **7**, 36 (2004). 3

[9] T. Egami and S. J. L. Billinge, *Underneath the Bragg peaks : structural analysis of complex materials* (Pergamon, Kiddington, Oxford, UK, 2003). 3, 4, 12, 48, 63

[10] R. J. McQueeney, Physical Review B **57**, 10560 (1998). 4, 48

[11] W. Dmowski, S. B. Vakhrushev, I. K. Jeong, M. P. Hehlen, F. Trouw, and T. Egami, Physical Review Letters **100**, (2008). 4, 49, 59

[12] T. Egami, K. Maeda, and V. Vitek, Philosophical Magazine A **41**, 883 (1980). 5, 50, 51, 77, 87, 117

[13] T. Egami, Progress in Materials Science **56**, 637 (2011). 5

[14] P. Hohenberg and W. Kohn, Physical Review B **136**, B864 (1964). 5, 35, 76, 118

[15] W. Kohn and L. J. Sham, Physical Review **140**, 1133 (1965). 5, 37, 76, 118

[16] O. H. Nielsen and R. M. Martin, Physical Review B **32**, 3792 (1985). 6, 51, 77

[17] Y. Wang, G. M. Stocks, W. A. Shelton, D. M. C. Nicholson, Z. Szotek, and W. M. Temmerman, Physical Review Letters **75**, 2867 (1995). 6, 45, 78, 119

[18] D. M. C. Nicholson, G. M. Stocks, Y. Wang, W. A. Shelton, Z. Szotek, and W. M. Temmerman, Physical Review B **50**, 14686 (1994). 6, 45, 78, 119

[19] X. G. Zhang and D. M. C. Nicholson, Physical Review B **60**, 4551 (1999). 6, 120

[20] W. Klement, R. H. Willens, and P. Duwez, Nature **187**, 869 (1960). 8, 100

[21] J. L. Yarnell, M. J. Katz, R. G. WEnzel, and S. H. Koenig, Phys. Rev. A. **7**, 2130 (1973). xiii, 13

[22] W. Kob, Journal of Physics-Condensed Matter **11**, R85 (1999). xiii, 15

[23] W. Kob, Slow relaxations and nonequilibrium dynamics in condensed matter, Proceedings of the Les Houches Summer School of Theoretical Physics, Session **77**, 1 (2002). xiii, 15

[24] J. M. Haile, *Molecular Dynamic Simulation Elementary Methods* (John Wiley and SONS, INC, 1992). 16, 21, 22, 63

[25] D. R. Reichman and P. Charbonneau, Journal of Statistical Mechanics-Theory and Experiment , (2005). xiii, 17

[26] W. Kob and H. C. Andersen, Physical Review E **52**, 4134 (1995). xiii, 18

[27] J. Horbach, W. Kob, and K. Binder, Philosophical Magazine B **77**, 297 (1998). xiii, 19, 20

[28] W. Kob and H. C. Andersen, Physical Review E **51**, 4626 (1995). xiii, 19, 20, 22, 23, 24

[29] C. A. Angell, Nuovo Cimento D **16**, 993 (1994). xiv, 25

[30] C. A. Angell, Science **267**, 1924 (1995). 26

[31] C. A. Angell, Journal of Physics and Chemistry of Solids **49**, 863 (1988). 26

[32] K. Ito, C. T. Moynihan, and C. A. Angell, Nature **398**, 492 (1999). 26

[33] J. P. Garrahan and D. Chandler, Proceedings of the National Academy of Sciences of the United States of America **100**, 9710 (2003). 26

[34] C. A. Angell, Journal of Non-Crystalline Solids **73**, 1 (1985). 26

[35] M. L. Ferrer, H. Sakai, D. Kivelson, and C. Alba-Simionesco, Journal of Physical Chemistry B **103**, 4191 (1999). 27

[36] G. Ruocco, F. Sciortino, F. Zamponi, C. De Michele, and T. Scopigno, Journal of Chemical Physics **120**, 10666 (2004). 27

[37] S. Sastry, P. G. Debenedetti, and F. H. Stillinger, Nature **393**, 554 (1998). 27

[38] W. Kauzmann, Chemical Reviews **43**, 219 (1948). 27

[39] A. P. Sokolov, A. Kisliuk, D. Quitmann, and E. Duval, Physical Review B **48**, 7692 (1993). 29

[40] A. P. Sokolov, Physica B **220**, 251 (1996). 29

[41] N. V. Surovtsev and A. P. Sokolov, Physical Review B **66**, (2002). 29

[42] S. W. Lovesey, *Theory of neutron scattering from condensed matter* (Clarendon Press, Oxford, 1984). 30

[43] V. K. Malinovsky, V. N. Novikov, P. P. Parshin, A. P. Sokolov, and M. G. Zemlyanov, Europhysics Letters **11**, 43 (1990). xiv, 30

[44] C. C. Yu and J. J. Freeman, Physical Review B **36**, 7620 (1987). xiv, 31

[45] R. Stoller, G. Odette, and B. Wirth, Journal of Nuclear Materials **251**, 49 (1997). 32

[46] M. J. Norgett, M. T. Robinson, and I. M. Torrens, Nuclear Engineering and Design **33**, 50 (1975). 32

[47] G. H. Kinchin and R. S. Pease, Reports on Progress in Physics **18**, 1 (1955). 32

[48] F. Garner, D. Gelles, and F. Wiffen, *Optimizing materials for nuclear applications* (The Metallurgical Society, Inc., Warrendale, PA, 1985). 33

[49] M. Levy, Proceedings of the National Academy of Sciences of the United States of America **76**, 6062 (1979). 37, 76

[50] A. D. Becke, Physical Review A **38**, 3098 (1988), Becke, ad. 39

[51] J. P. Perdew and Y. Wang, Physical Review B **45**, 13244 (1992). 39

[52] J. P. Perdew, K. Burke, and M. Ernzerhof, Physical Review Letters **77**, 3865 (1996). 39

[53] J. W. Strutt and B. Rayleigh, Philosophical magazine **34**, 4816 (1892). 40

[54] J. Korringa, Physica **13**, 392 (1947). 40

[55] W. Kohn and N. Rostoker, Physical Review **94**, 1111 (1954). 40

[56] J. S. Faulkner, Progress in Materials Science **27**, 1 (1982). 40

[57] P. Weinberger, *Electron scattering theory for ordered and disordered matter* (Clarendon Press Oxford, 1990). 40

[58] A. Gonis, *Green functions for ordered and disordered systems* (North-Holland Amsterdam, 1992). 40

[59] H. Winter and G. M. Stocks, Physical Review B **27**, 882 (1983). 40

[60] J. S. Faulkner and G. M. Stocks, Physical Review B **21**, 3222 (1980). 41

[61] D. Fabian and L. Watson, *Band structure spectroscopy of metals and alloys: proceedings* (Academic, New York, 1973). 41

[62] D. D. Johnson, F. J. Pinski, and G. M. Stocks, Physical Review B **30**, 5508 (1984). 44

[63] T. Egami and Y. Waseda, Journal of Non-Crystalline Solids **64**, 113 (1984). 51, 103, 113

[64] O. H. Nielsen and R. M. Martin, Physical Review Letters **50**, 697 (1983). 51, 77, 117

[65] B. J. Alder and T. E. Wainwright, Journal of Chemical Physics **27**, 1208 (1957). 53

[66] A. Rahman, Physical Review a-General Physics **136**, A405 (1964). 53

[67] M. P. Allen and D. J. Tildesley, *Computer simulation of liquids* (Clarendon Press ; Oxford University Press, Oxford, England, 1989). 54, 59

[68] D. Frenkel and B. Smit, *Understanding molecular simulation: from algorithms to applications* (Academic, London, 2002). 54

[69] C. Gear, *Initial value Problems in Ordinary Differential Equation* (Prentice-Hall, Englewood Cliffs, NJ, 1971). 54, 59

[70] H. J. C. Berendsen, J. P. M. Postma, W. F. Vangunsteren, A. Dinola, and J. R. Haak, Journal of Chemical Physics **81**, 3684 (1984). 55

[71] R. Kubo, Reports on Progress in Physics **29**, 255 (1966). 55

[72] S. Nose, Molecular Physics **52**, 255 (1984). 55, 60

[73] W. G. Hoover, Physical Review A **31**, 1695 (1985). 55

[74] M. S. Daw and M. I. Baskes, Physical Review Letters **50**, 1285 (1983). 56

[75] M. S. Daw and M. I. Baskes, Physical Review B **29**, 6443 (1984). 56

[76] M. W. Finnis and J. E. Sinclair, Philosophical Magazine A **50**, 45 (1984). 56, 67, 120

[77] A. F. Voter, *Intermetallic Compounds: Principles and Practice* (Wiley, New York, 1994). 56

[78] R. E. Stoller, Jom-Journal Of The Minerals Metals Materials Society **48**, 23 (1996). 56

[79] W. J. Phythian, R. E. Stoller, A. J. E. Foreman, A. F. Calder, and D. J. Bacon, Journal of Nuclear Materials **223**, 245 (1995). 56

[80] A. F. Calder and D. J. Bacon, Journal of Nuclear Materials **207**, 25 (1993). xvi, 56, 67, 116, 120

[81] R. E. Stoller, Journal of Nuclear Materials **233**, 999 (1996). 56

[82] D. J. Bacon, A. F. Calder, J. M. Harder, and S. J. Wooding, Journal of Nuclear Materials **205**, 52 (1993). 56

[83] M. W. Finnis, Philosophical Magazine A **53**, 161 (1986). 56, 67, 120

[84] M. W. Finnis, AERE R-13182, **UK AEA Harwell Laboratory** (1988). 56, 67

[85] J. M. Harder and D. J. Bacon, Philosophical Magazine A **58**, 165 (1988). 56

[86] Y. Wang, D. M. C. Nicholson, G. M. Stocks, A. Rusanu, M. Eisenbach, and R. E. Stoller, Journal of Applied Physics **109** (2011). 57, 67

[87] Y. Wang, D. Nicholson, G. Stocks, A. Rusanu, M. Eisenbach, and R. E. Stoller, MRS Online Proceedings Library **1363** (2011). 57, 67

[88] R. A. Johnson, Physical Review a-General Physics **134**, 1329 (1964). 59

[89] T. Tomida and T. Egami, Physical Review B **52**, 3290 (1995). 59

[90] V. A. Levashov, T. Egami, R. S. Aga, and J. R. Morris, Physical Review B **78** (2008). 59, 65, 77, 117

[91] L. Van Hove, Physical Review **95**, 249 (1954). 63

[92] M. Born, K. Huang, and M. Lax, American Journal of Physics **23**, 474 (1955). 65

[93] T. Keyes, The Journal of Physical Chemistry A **101**, 2921 (1997). 65

[94] S. P. Chen, T. Egami, and V. Vitek, Physical Review B **37**, 2440 (1988). 65

[95] S. J. Zinkle, Physics of Plasmas **12** (2005). 67

[96] R. E. Stoller and A. F. Calder, Journal of Nuclear Materials **283**, 746 (2000). 67, 120

[97] R. I. Henderson, Physics Letters A **49**, 197 (1974). 67

[98] Y. Wang, G. M. Stocks, and J. S. Faulkner, Physical Review B **49**, 5028 (1994). 73

[99] E. Gross and R. Dreizler, *Density functional theory* (Springer, New York, 1995). 76

[100] W. Kohn and P. Vashishta, Plenum Press, New York , 79 (1983). 76

[101] R. Parr and W. Yang, *Density-functional theory of atoms and molecules* (Oxford University Press, USA, 1994). 76

[102] D. D. Johnson, D. M. Nicholson, F. J. Pinski, B. L. Gyorffy, and G. M. Stocks, Physical Review Letters **56**, 2088 (1986). 77

[103] T. Egami, S. J. Poon, Z. Zhang, and V. Keppens, Physical Review B **76** (2007). 77, 117

[104] V. Vitek and T. Egami, Physica Status Solidi B-Basic Research **144**, 145 (1987). 77

[105] A. Filippetti and V. Fiorentini, Physical Review B **61**, 8433 (2000). 77, 117

[106] R. Bader, Atoms in Molecules. A Quantum Theory, Claredon (1990). 78

[107] M. Yu, D. Trinkle, and R. Martin, Physical Review B **83**, 115113 (2011). 78

[108] M. Yu and D. Trinkle, Journal of Chemical Physics **134**, 64111 (2011). 78

[109] H. Hellmann, *Einfhrung in die quantenchemie: Texte imprim* (F. Deuticke, 1937). 82

[110] R. P. Feynmann, Phys. Rev **56**, 340 (1939). 82

[111] J. Harris, Physical Review B **31**, 1770 (1985). 86

[112] U. V. Barth and L. Hedin, Journal of Physics Part C Solid State Physics **5**, 1629 (1972). 89

[113] C. Jiang, C. Wolverton, J. Sofo, L. Chen, and Z. Liu, Physical Review B **69**, 214202 (2004). 93

[114] G. Kresse and J. Furthmuller, Physical Review B **54**, 11169 (1996). 93

[115] G. Kresse and J. Furthmuller, Computational Materials Science **6**, 15 (1996). 93

[116] A. Inoue, T. Zhang, and T. Masumoto, Materials Transactions Jim **31**, 425 (1990). 100

[117] T. Zhang, A. Inoue, and T. Masumoto, Materials Transactions Jim **32**, 1005 (1991). 100

[118] A. Inoue, T. Nakamura, N. Nishiyama, and T. Masumoto, Materials Transactions Jim **33**, 937 (1992). 100

[119] A. Peker and W. L. Johnson, Applied Physics Letters **63**, 2342 (1993). 100

[120] A. Inoue, Materials Transactions Jim **36**, 866 (1995). 100

[121] A. L. Greer, Science **267**, 1947 (1995). 100

[122] A. Inoue, Acta Materialia **48**, 279 (2000). 100

[123] W. L. Johnson, Mrs Bulletin **24**, 42 (1999). 100

[124] H. Okamoto and T. Massalski, Journal of Phase Equilibria **4**, 190 (1983). xv, 100

[125] F. Spaepen and D. Turnbull, *Rapidly quenched metals* (MIT Press, Cambridge, MA, 1976). 101

[126] T. Egami, M. Ojha, D. Nicholson, D. Louzguine-Luzgin, N. Chen, and A. Inoue, Philosophical Magazine **92**, 655 (2012). xv, 101, 102

[127] W. F. Gale and T. C. Totemeier, *Smithells metals reference book*, 8th ed. (Elsevier Butterworth-Heinemann, Oxford, 2004). xv, 101

[128] A. Takeuchi and A. Inoue, Materials Transactions **46**, 2817 (2005). 103

[129] H. Buchler and K. J. Range, Journal of the Less-Common Metals **160**, 143 (1990). 103

[130] H. Buchler and K. J. Range, Journal of the Less-Common Metals **161**, 347 (1990). 105

[131] M. Puselj and K. Schubert, Journal of the Less-Common Metals **35**, 259 (1974). 105

[132] R. F. Hoyt and A. C. Mota, Journal of the Less-Common Metals **62**, 183 (1978). 108, 109

[133] D. Turnbull, Journal of Chemical Physics **20**, 411 (1952). 112

[134] F. C. Frank, Proceedings of the Royal Society of London Series a-Mathematical and Physical Sciences **215**, 43 (1952). 112

[135] D. B. Miracle, D. V. Louzguine-Luzgin, L. V. Louzguina-Luzgina, and A. Inoue, International Materials Reviews **55**, 218 (2010). 113

[136] D. B. Miracle, Acta Materialia **54**, 4317 (2006). 113

[137] R. E. Stoller, *Primary radiation damage Formation*Comprehensive Nuclear materials (Elsevier Ltd., Amsterdam, 2012). 116

[138] M. S. Daw and M. I. Baskes, Physical Review B **29**, 6443 (1984). 117

[139] J. F. Lutsko, Journal of Applied Physics **65**, 2991 (1989). 117

[140] I. Alber, J. L. Bassani, M. Khantha, V. Vitek, and G. J. Wang, Philosophical Transactions of the Royal Society of London Series A **339**, 555 (1992). 117

[141] S. Dudarev and P. Derlet, Journal of Physics: Condensed Matter **17**, 7097 (2005). 123

Vita

I was born in Mahadevsthan Village Development Committee (VDC), Doti district of Nepal. I received my Bachelor of Science (B. Sc.) with major in Physics and Master of Science (M. Sc.) degree with major in Physics from Tribhuvan University (TU), Kathmandu, Nepal. After completing my M. Sc. degree in Physics in 1994 I joined Tribhuvan University, Kathmandu Nepal as a Lecturer in Physics and worked there from December 1994 to August 2000. I got my Masters degree in Physics from University of Kentucky, Lexington, Kentucky in 2003. I came to University of Tennessee in August of 2005 for my doctoral study. I did my research work at The University of Tennessee and at Oak Ridge National Laboratory with Prof. Takeshi Egami. Dr. D. M. Nicholson, a Senior Scientist at Oak Ridge national Laboratory, also mentored me for my dissertation research. I received my Doctor of Philosophy degree in Physics in August 2012.